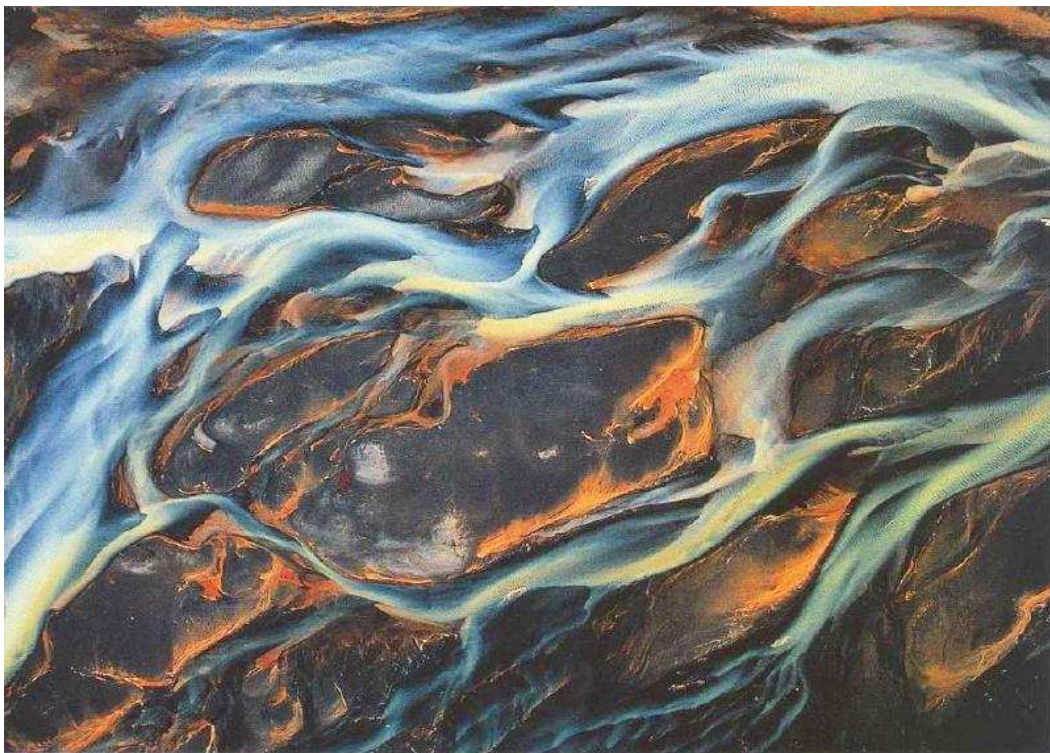


Dottorato di Ricerca in Ingegneria Idraulica

Unit processes in braided rivers

Rodolfo Repetto



Supervisor: Marco Tubino

Rodolfo Repetto

University of L'Aquila

Dipartimento di Ingegneria delle Strutture, delle Acque e del Terreno

Monteluco di Roio, 67040, L'Aquila, Italy

tel: +39 0862 434545

fax: +39 0862 434548

e-mail: rodolfo.repetto@univaq.it

Contents

1	Introduction	1
2	Experimental study in a flume with variable width	11
2.1	Introduction	11
2.2	Experimental set up	14
2.3	Experimental runs	17
2.3.1	Experiments performed	17
2.3.2	Experimental procedure	17
2.4	Experimental results	19
2.4.1	Series “a”: suppression of free bars	19
2.4.2	Series “b”: forced response	22
3	Flow field and bed topography in channels with variable width	27
3.1	Introduction	27
3.2	2D depth-averaged model	29
3.2.1	Formulation of the problem	29
3.2.2	Linear solution	32
3.2.3	Results	35
3.3	3D model	41
3.3.1	Formulation of the problem	41
3.3.2	Linearization	44
3.3.3	Solution	45
3.3.4	Results	49
3.4	Comparison with experimental results	54
3.5	Correction due to the streamlines curvature effect on transverse bed shear stress	59
3.6	Planimetric evolution	62
4	Suppression of free bars in channels with variable width	69
4.1	Introduction	69

4.2	Formulation of the problem	70
4.3	Solution	70
4.3.1	Outline of the solution procedure	70
4.3.2	First order free problem - $\mathcal{O}(A)$	72
4.3.3	First order forced problem - $\mathcal{O}(\delta)$	74
4.3.4	Scheme of the solution at the higher orders	75
4.3.5	$\mathcal{O}(\delta^2)$ problem	77
4.3.6	$\mathcal{O}(A\delta)$ problem	78
4.3.7	Solvability condition	79
4.4	Results	80
5	Stability of bifurcations in channels with movable bed	85
5.1	Introduction	85
5.2	Previous contributions: Wang et al. (1995) model	87
5.3	Formulation of the problem	90
5.3.1	Problem for a single channel	90
5.3.2	Problem for a channels network	93
5.4	Numerical scheme	96
5.4.1	Solution for a single channel	98
5.4.2	Solution for a channel network	99
5.5	Results	102
5.5.1	Single channel	102
5.5.2	Channel network	104
5.5.3	Comparison with the results of Wang et al. (1995) . . .	110
A	Experimental results	113
A.1	Series “a”	113
A.2	Series “b”	119
B	Stability of bifurcations	131
	Bibliography	135
	Acknowledgements	138
	Ringraziamenti	140

List of Figures

1.1	Sunwapta river, Alberta, Canada (flow from left to right). . .	2
1.2	Borbera river, Italy (courtesy of Guido Zolezzi).	3
1.3	Braiding mechanisms. (a) central bar braiding mechanism, (b) alternating point bar chute cutoff, (c) dissection of multiple row bars (from Ashmore (1991)).	5
1.4	Circulation in a simple channel junction (from Ashmore (1982)).	6
1.5	Avulsion and incision of a new channel (from Ashmore (1982)).	7
1.6	Incision of a large bar (from Ashmore (1982)).	8
2.1	Width variations in Sunwapta river, Alberta, Canada (flow toward the camera).	12
2.2	Spectral analysis of width variations, Meduna river, Italy (A harmonics amplitude, λ wave number).	13
2.3	Picture of the flume.	15
2.4	Fourier spectra of leading components of bottom elevation (run "a11").	20
2.5	Comparison between the amplitudes of the leading harmonic ($i, 1$) (alternate bar mode) measured in the case of constant width channel and in the case of width variations.	21
2.6	Comparison between the wavenumber of bars measured in the case of constant width channel and in the case of width variations.	22
2.7	Amplitude of the leading purely longitudinal component of bed profile with respect to Shields parameter (experiments b35-b44).	23
3.1	Sketch of the geometry and notation.	30
3.2	Typical equilibrium bed configuration ($\lambda_b = 0.2$, $\beta = 15$, $\vartheta_0 = 0.07$, $d_s = 0.05$).	35
3.3	Velocity and bed elevation longitudinal profiles ($\lambda_b = 0.2$, $\beta = 15$, $\vartheta_0 = 0.07$, $d_s = 0.05$).	36

3.4	Transverse bed profile in different sections ($\lambda_b = 0.2, \beta = 15, \vartheta_0 = 0.07, d_s = 0.05$).	36
3.5	Resonance point for central bars in the plane λ, β ($\theta_0 = 0.07, d_s = 0.05$).	37
3.6	Equilibrium bed configuration close to resonant conditions ($\lambda_b = 0.237, \beta = 15.9, \vartheta_0 = 0.07, d_s = 0.05$).	39
3.7	Transverse bed profile in different sections ($\lambda_b = 0.237, \beta = 15.9, \vartheta_0 = 0.07, d_s = 0.05$).	39
3.8	Difference between bed elevation at the centerline and the the banks versus width variations wave number λ_b for different values of width parameter β . $\beta = 15.851$ corresponds to the resonant value ($\theta_0 = 0.07, d_s = 0.05$).	40
3.9	Sketch of the geometry and notation.	42
3.10	Equilibrium bed configurations for different values of the wavenumber of width variations. (a) $\lambda_b = 0.1$, (b) $\lambda_b = 0.2$, (c) $\lambda_b = 0.3$, (d) $\lambda_b = 0.5$ ($\vartheta_0 = 0.1, d_s = 0.05, \beta = 10$).	50
3.11	Fourier analysis of bottom profile: amplitude of the first three harmonics obtained with the 3D and the 2D models, respectively. (a), (e) $\lambda_b = 0.1$; (b), (f) $\lambda_b = 0.2$; (c), (g) $\lambda_b = 0.3$; (d), (h) $\lambda_b = 0.5$ ($\vartheta_0 = 0.1, d_s = 0.05, \beta = 10$).	51
3.12	Fourier analysis of longitudinal velocity: amplitude of the first three harmonics obtained with the 3D and the 2D models, respectively. (a), (e) $\lambda_b = 0.1$; (b), (f) $\lambda_b = 0.2$; (c), (g) $\lambda_b = 0.3$; (d), (h) $\lambda_b = 0.5$ ($\vartheta_0 = 0.1, d_s = 0.05, \beta = 10$).	52
3.13	(a) Mechanism of generation of secondary flow in the plane (y,z), (b), (c) secondary flow and bed deformation at the narrowest section.	52
3.14	Secondary flow at the narrowest section ($\beta = 10, \lambda_b = 0.2, \vartheta_0 = 0.1, d_s = 0.05$).	53
3.15	Comparison between the first two transverse harmonics of the Fourier representation of the bed predicted by the theory and the experiments.	55
3.16	Amplitude of the first two transverse harmonics of the Fourier representation of bed topography ($\lambda_b = 0.5, \delta = 0.125$).	56
3.17	Amplitude of the first two transverse harmonics of the Fourier representation of bed topography ($\lambda_b = 0.3, \delta = 0.125$).	57
3.18	Amplitude of the first two transverse harmonics of the Fourier representation of bed topography ($\lambda_b = 0.3, \delta = 0.25$).	58
3.19	Real and imaginary part of k versus λ_b ($\beta = 15, \vartheta_0 = 0.1, d_s = 0.01$).	60

3.20	Amplitude ((a), (c), (e)) and phase ((b), (d), (f)) of harmonic 1 of bed profile versus λ_b , for different values of β . (a), (b) $\beta = 10$; (c), (d) $\beta = 15$; (e), (f) $\beta = 20$ ($\vartheta_0 = 0.1$, $d_s = 0.05$, $\beta = 10$).	62
3.21	Amplitude ((a), (c), (e)) and phase ((b), (d), (f)) of harmonic 1 of longitudinal velocity component versus λ_b , for different values of β . (a), (b) $\beta = 10$; (c), (d) $\beta = 15$; (e), (f) $\beta = 20$ ($\vartheta_0 = 0.1$, $d_s = 0.05$, $\beta = 10$).	63
3.22	Amplitude ((a), (c), (e)) and phase ((b), (d), (f)) of harmonic 1 of transverse velocity component versus λ_b , for different values of β . (a), (b) $\beta = 10$; (c), (d) $\beta = 15$; (e), (f) $\beta = 20$ ($\vartheta_0 = 0.1$, $d_s = 0.05$, $\beta = 10$).	64
3.23	Transverse bottom profile for different values of the longitudinal coordinate. (a), (b) $\lambda_b = 0.1$; (c), (d) $\lambda_b = 0.2$; (e), (f) $\lambda_b = 0.3$; (g), (h) $\lambda_b = 0.5$ ($\vartheta_0 = 0.1$, $d_s = 0.05$, $\beta = 10$).	65
3.24	The phase α_u of longitudinal depth-average velocity at the centerline (dotted lines) and at the banks (continuous lines) is plotted versus the wavenumber of width variations (thinner lines: 2D model; ticker lines: 3D model) ($\beta = 20$, $\vartheta_0 = 0.1$, $d_s = 0.05$)	66
3.25	The difference between the bank values of the depth averaged longitudinal velocity at the narrowest and widest section is plotted versus the wavenumber of width variations($\beta = 20, \vartheta_0 = 0.1$, $d_s = 0.05$).	66
3.26	Neutral stability curves in the plane (λ_b, ϑ_0) ($\beta_0 = 15$, $d_s = 0.05$).	67
4.1	Neutral stability curve for bars formation.	73
4.2	The correction Ω_1 to the growth rate of free bars is plotted versus λ_b (a) and λ (b) for different values of Shields parameter ϑ_0 ((a) $\lambda = 0.5$, (b) $\lambda_b = 0.3$, $\beta = 20$, $d_s = 0.01$).	80
4.3	The threshold value of δ above which bars are suppressed is plotted versus β for different values of ϑ_0 ($d_s = 0.05$, $\lambda_b = 0.3$).	81
4.4	The growth rate Ω of free bars is plotted versus λ for different values of λ_b , (a) $\beta = 18$, (b) $\beta = 34$ (cwc: constant width channel. $\vartheta_0 = 0.2$, $d_s = 0.01$, $\delta = 0.125$).	81
4.5	The growth rate Ω of free bars is plotted versus λ for different values of λ_b , (a) $\vartheta_0 = 0.1$, (b) $\vartheta_0 = 0.2$ (cwc: constant width channel. $\beta = 20$, $d_s = 0.01$, $\delta = 0.125$).	82
4.6	The correction ω_1 to total angular frequency ω of free bars is plotted versus λ for different values of λ_b ($\vartheta_0 = 0.2$, $d_s = 0.01$, $\beta = 18$, $\delta = 0.125$).	82

4.7	The total angular frequency ω of free bars is plotted versus λ for different values of λ_b ($\vartheta_0 = 0.2$, $d_s = 0.01$, $\beta = 18$, $\delta = 0.125$).	83
5.1	Bifurcation in a braided river, Sunwapta (Alberta, Canada).	86
5.2	Geometry of the network.	88
5.3	Notation.	91
5.4	Sketch of the nodal point condition.	93
5.5	Numerical cell.	97
5.6	Bed profiles at different times; the sediment discharge has been increased by 10%. The initial channel slope has been filtered out from bed profile.	103
5.7	Bed and water level profiles at different times; the water level has been increased by 100%.	104
5.8	Bottom profile development under stable conditions. The initial channel slope has been filtered out from bed profile.	105
5.9	Bottom profile development under unstable conditions. The initial channel slope has been filtered out from bed profile.	106
5.10	The critical Shields number θ is plotted versus the width ratio β for different Froude numbers (channels width $b=50\text{m}$, channels slope $S=0.008$).	107
5.11	The critical Shields number θ is plotted versus the Froude number F (channels width $b=50\text{m}$, channels slope $S=0.008$).	107
5.12	The critical Shields number θ is plotted versus the coefficient α (channels width $b=50\text{m}$, channels slope $S=0.008$).	108
5.13	The critical Shields number θ is plotted versus the coefficient t_b (channels width $b=50\text{m}$, channels slope $S=0.008$).	108
5.14	Bottom and free surface profile development forced by raising water level at the downstream end of channel b .	109
5.15	The critical value of the exponent of the nodal point relation k is plotted versus Shields parameter ϑ for different values of Froude number.	111
5.16	The value of the exponent of the nodal point relation k as a function of time for different Shields parameters ϑ .	111

List of Tables

2.1	Realized bank configurations.	14
2.2	Summary of experimental conditions of series “a”.	19
2.3	Summary of experimental conditions of series “b” (runs b1-b26).	24
2.4	Summary of experimental conditions of series “b” (runs b27- b52).	25
2.5	Summary of experimental conditions of series “b” (runs b53- b67).	26

List of Main Symbols

*	superscript asterisks denote dimensional variables
,	subscript commas denote derivative operators
A	amplitude of free alternate bars
a	amplitude of width variations
b	width
C_f	friction factor
<i>c.c.</i>	complex conjugate
D	water depth
d_s	sediment diameter
E	Erosion coefficient
F	Froude number
g	gravity
G	local bottom gradient normal to bed stress vector
H	free surface elevation
k_s	Gauckler and Strickler coefficient
L_b	width variations wave length
\mathcal{N}	vertical structure of turbulent kinematic viscosity
n	coordinate normal to s
$\mathcal{O}(\dots)$	order of magnitude
Q	water discharge
$\mathbf{q} = (q_x, q_y)$	bed load vector
$\hat{\mathbf{n}}$	unit vector normal to the banks
p	sediment porosity
R_h	hydraulic radius
r	empirical constant for transverse slope effect
r_c	curvature radius of streamlines
S	channel slope
$\mathbf{u} = (u, v, w)$	velocity
$\mathbf{U} = (U, V)$	depth averaged velocity
U_b	excess of depth averaged velocity at the bank with respect to uniform flow velocity
U_n	bank depth-averaged velocity at the narrowest section
U_w	bank depth-averaged velocity at the widest section
s	coordinate along the streamlines
t	time
x	longitudinal coordinate
y	transverse coordinate

y_s	bank profile
z	coordinate normal to x and y
β	width ratio
β_c	critical value of width ratio for bar formation
β_r	resonant width ratio
$\delta = a/2$	amplitude of width variations
Φ	bed load function
η	bed elevation
λ	wave number
λ_b	wave number of width variations
λ_m	meander wave number
λ_r	resonant wave number
Ω	growth rate of bars
ω	migration speed of bars
Σ	section surface
ϑ	Shields parameter
ϑ_c	critical value of Shields parameter for sediment movement
ρ	water density
ρ_s	sediment density
$\boldsymbol{\tau} = (\tau_x, \tau_y)$	bottom stress

Chapter 1

Introduction

In the last two decades the understanding of the basic mechanisms controlling the large scale morphodynamics of river systems has been considerably improved. The latter progress, though accomplished with the aid of a large number of field observations and laboratory investigations, is mainly the result of theoretical analyses based on a mechanical approach, coupled with reasonable assumptions on relative importance of the temporal and spatial scales involved. In this context asymptotic (perturbation) methods have been proved to be particularly successful to describe the variety of patterns which may arise when a suitable model for the hydrodynamic transport of particles is fed into the conservation law for sediment. For instance, the formation of river bars has been conclusively explained in terms of an inherent instability of an erodible bed subject to a turbulent flow in almost straight channels. This leads to the spontaneous development of free bottom perturbations migrating downstream. Furthermore, the fundamental mechanisms which control the planimetric evolution of single channels have been mainly understood in terms of nonlinear competition between (self-excited) free bed responses and the forced topography.

However theoretical predictors mostly refer to the case of single thread channels (meandering rivers), well sorted sediment and steady flow. As for braided rivers, satisfying dynamical models are not yet available: furthermore, typical signs of chaotic behavior seem to emerge from the results of the simplified model of Murray & Paola (1994), which suggest that the behavior of these systems may be unpredictable over large time scales.

The fundamental factors distinguishing braided from meandering rivers are still unclear. However braiding seems to occur provided the flow be sufficiently laterally unconstrained, this implying that the channels can change freely their width. Furthermore, braiding occurs in the presence of bedload transport rather than suspended load. On the other hand meandering rivers



Figure 1.1: Sunwapta river, Alberta, Canada (flow from left to right).

do not develop without the presence of some form of sides stabilization to constrain the flow laterally, such as cohesive material constituting the banks or the presence of vegetation. According to these observations Murray & Paola (1994) define the braiding process as “*the fundamental instability of laterally unconstrained free-surface flow over cohesionless beds*”. Furthermore the authors consider the meandering of rivers as the result of partial suppression of the above instability by factors that can inhibit local redeposition, such as dominant suspended load, or can constrain laterally the channel. In figures 1.1 and 1.2 two examples of braided rivers are shown.

A detailed modeling of a braided network presents several difficulties, the system being characterized by numerous complicating features. The main physical ingredients required to correctly reproduce the generation and development of braided systems are briefly discussed in the following.

- i) *Strong nonlinearities*. Braided systems are characterized by strong nonlinearities; in particular the interactions between free responses of the system (due to an inherent instability of free surface turbulent flow over an erodible bed) and forced responses (induced by physical constraints, such as curvature, width variations, confluences, ...) crucially affect the topographic behavior of the network.
- ii) *Unsteadiness*. Flow field and sediment transport in braided rivers are



Figure 1.2: Borbera river, Italy (courtesy of Guido Zolezzi).

typically unsteady. An equilibrium configuration of the system does not seem to exist, rather a recursive process of formation and obliteration of bed forms and planimetric structures is always observed.

- iii) *Time scales.* Unlike in the case of meandering rivers, where bed development is much faster than planform development due to the effect of cohesion and vegetation on bank stability, here the time scales of bed and bank erosion are comparable. Hence, the full coupling between bed and planform evolution must be retained. Furthermore, bank erosion induces a net effect on sediment transport.
- iv) *Gravitational effects on sediment transport.* Gravitational effects on bedload transport have been found to play a fundamental role in river morphodynamics, since they affect both the instability process which leads to bar development and the equilibrium configuration of bedforms (Fredsoe (1978), Colombini et al. (1987)). In braided systems the presence of strong local depositions and scours, like those induced by channel migration and confluences, implies that such effects have to be taken into account in detail.
- v) *Partially transporting cross sections.* Braided rivers are characterized by relatively small values of Shields stress, which falls close to the crit-

ical value even at high stages. Typically only some branches are simultaneously active. Furthermore, in a single channel sediment transport may occur only in a limited part of the cross section; hence, the possibility of partial transport of sediment within the cross section must be accounted for to model the network.

- vi) *Secondary flows.* Depositional and scour phenomena in alluvial rivers are often associated with the development of secondary flows: a notable example is bed deformation associated with secondary flows induced by centrifugal effect in curved channels. In braided systems secondary flows may be triggered by centrifugal effect induced by curvature of streamlines of depth averaged flow and by inertial effects associated with flow adjustments to spatial variations of channel geometry.
- vii) *Finite length effects.* The relatively small length of each branch, due to the continuous interplay of channels, implies that the condition of infinite longitudinal domain, which is often introduced to investigate bar development in rivers, can be hardly reproduced by single branches of braided systems. Hence, upstream and downstream influences may crucially affect water and sediment motion in each channel.

Due to the above features, braided rivers have been so far investigated within the context of two different, and somehow complementary, points of view: the study of the whole network under suitable simplifying hypotheses or the investigation of single unit processes characterizing the network. Both approaches are supported by experimental and field works which provide a fundamental patrimony of observations and data.

Following the first approach several numerical models have been developed, with the aim of identifying the essential processes required to describe the dynamics of the network. Murray & Paola (1994), for instance, tackle the problem through a cellular model: the spatial domain is split into cells and simple laws for the exchange of water and sediment between adjacent cells are adopted. The given initial condition is a uniformly sloping bed over which a white-noise perturbation is superimposed. The model is able to reproduce a braiding-like configuration and seems suitable to catch the main features of a braiding: channels divisions, confluences, branches migration; however, the unit processes can not be described in detail.

A second approach to braided rivers consider separately single unit processes governing the generation and development the network. Two experimental works of Ashmore (1982, 1991) provide a detailed description of these unit processes, which can be summarized as follows.

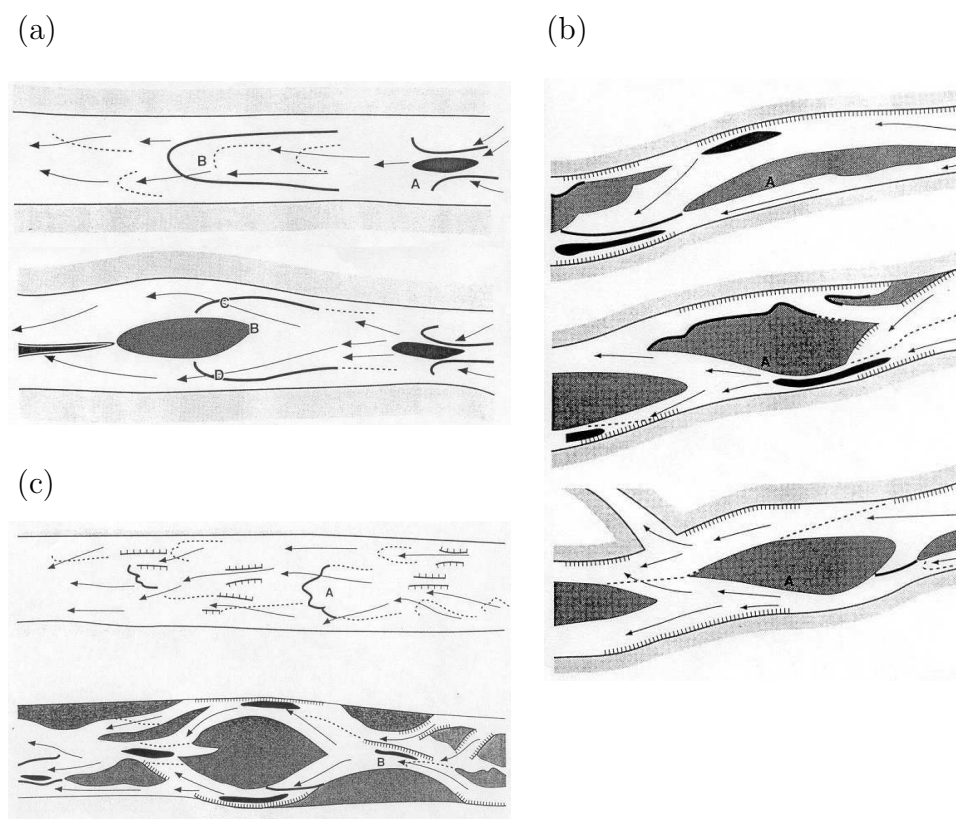


Figure 1.3: Braiding mechanisms. (a) central bar braiding mechanism, (b) alternating point bar chute cutoff, (c) dissection of multiple row bars (from Ashmore (1991)).

Channel bifurcations

Channel bifurcations are the formative process in braided systems; Ashmore (1991) describes the possible mechanisms through which braiding may develop:

- i) *Central bar mechanism and dissection of transverse unit bar.* These two mechanisms are the most commonly documented processes of braiding generation and have been first described by Leopold & Wolman (1957). They essentially imply the development of a submerged central bar initiated from a symmetrical transverse unit bar, whose downstream margin is usually marked by the accumulation of the coarsest fraction of bedload. Figure 1.3a shows the typical development of this process: the presence of the bar forces the flow to diverge and the central nucleus is eventually exposed. Immediately downstream of the bar the divided flows produce scour pools against the opposite banks, thus inducing a

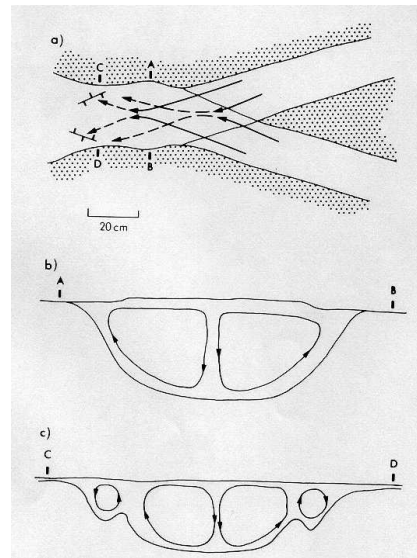


Figure 1.4: Circulation in a simple channel junction (from Ashmore (1982)).

widening of the channel and the generation of a bifurcation. Ashmore (1991) suggests that the distinction between the central bar mechanism and the dissection of transverse unit bar is essentially due to the much higher sediment mobility which characterizes the latter process.

- ii) *Chute cutoff mechanism.* A commonly reported alternative braiding process is the chute cutoff of point bars in low-sinuosity channels. Figure 1.3b shows an example of alternating point bar cutoff. A transverse alternating point bar in a weakly curved channel is transformed into a more complex bed form by lateral accretion of portions of migratory sheets that move along the channel. The rapid point bar accretion and concave bank erosion immediately upstream of the chute causes more flow to be directed over the point bar. The steep gradient near the head of the slough channels captures progressively larger volumes of water. The chute rapidly widens leading to the bifurcation of the flow. Chute cutoff process plays an important role in maintenance of the braided planform.
- iii) *Multiple bars mechanism.* The generation of braiding from multiple row bars was first documented by Fujita & Muramoto (1988). This particular mechanism appears to be a special case that applies only to channels with very high values of the width/depth ratio. The initial bed configuration, consisting of numerous multiple bars, is gradually converted to fewer larger bars which concentrate the flow into scour

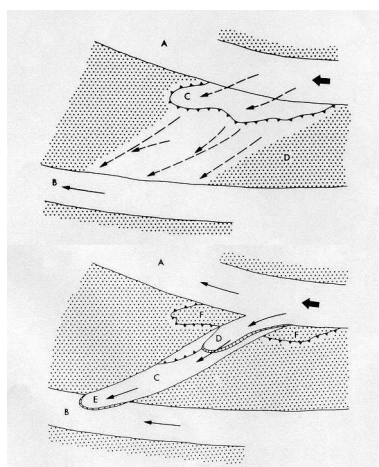


Figure 1.5: Avulsion and incision of a new channel (from Ashmore (1982)).

hollows, leading to dissection and emergence of portions of the bed and finally to braiding (figure 1.3c).

Confluences

Another important unit process is represented by channel confluences; it is probably the most studied braiding process since channel junctions generate deep scour holes (see for instance Ashmore & Parker (1983)). The scour is the result of strong secondary currents generated by the flow convergence (figure 1.4). Scour occurs in the zone of attachment of helical cells and deposition in the separation zone. According to Mosley (1976) the scour depth is controlled by the angle of incidence of the two channels and by the proportion of the total discharge flowing in each branch. The hole tends to parallel the alignment of the dominant channel.

Bar formation

In single branches of braided rivers alternating bars develop, similar to those of the straight channels. Though their formation may be associated to an inherent instability of the flow-sediment system, their development is crucially affected by local flow conditions like curvature and local widening. Channels confluences and alternating bars development are mainly responsible for the generation of scour holes.

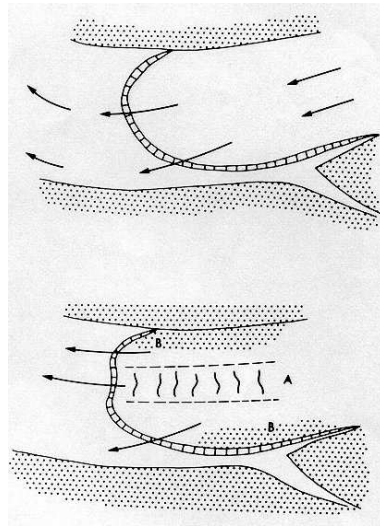


Figure 1.6: Incision of a large bar (from Ashmore (1982)).

Avulsions

Avulsions (figure 1.5) are typical events in a fully developed braiding. They occur under a variety of circumstances and do not necessarily involve reoccupation of an abandoned channel. The presence of bars plays a crucial role on the generation of avulsions both inducing bank erosion and raising the local water level allowing overtopping of the channels sides. When the water finds a definite path across the surface the incision of a new channel may occur.

Incision of bars

In braided networks large bars are often subject to an incision due to the generation of an axial trough which displays accelerated sediment transport (figure 1.6). This phenomenon usually occurs during declining water discharge, being triggered by the concentration of flow along one line.

Channels migration

Single channels in braided networks are subject to planimetric migration similar to that displayed by meandering rivers. However, since bank erosion occurs on a time scale which is of the same order of the scale of the altimetric deformation of the bed, channel migration in braided rivers is much faster than in meandering channels. The lateral migration of branches is typically driven by the scour at the outer bank produced by streamlines curvature. Strong width variations are also often documented.

In the present work the attention is focused on two unit processes characterizing braided systems. The first mechanism which have been investigated is the formation of a channel bifurcation. As discussed above, a mechanism which appears to play a significant role in such process is the tendency for diverging flows to give rise to sediment deposition in the central region of the channel, which in turn implies a tendency of the flow to concentrate on the sides of the central bar. In chapters 2, 3 and 4 of the present work the problem of bed development in channels subject to periodic width variations is tackled both experimentally and theoretically. The results show that width variations are likely to enhance the formation of central depositions and scours, suggesting that the development of transverse variations of the bed are mainly related to the development of secondary flows induced by the variable channel geometry. Under suitable conditions the equilibrium bed topography, forced by a variable bank profile, may lead the channel to be planimetrically unstable: the flow tends to enhance any small initial width variation leading to the generation of a bifurcation. Furthermore, theoretical and experimental results show that width variations inhibit the development of migrating alternating bars and promote the transition of previously formed alternating bars to steady central deposits.

A second unit process which has been considered in chapter 5 is the mechanism whereby one of the bifurcating channels may be progressively abandoned. The stability of a bifurcation has been investigated through a one dimensional numerical model, both in the unperturbed case and in the case forced by boundary conditions.

Chapter 2

Experimental study in a flume with variable width

2.1 Introduction

Width variations constitute a typical characteristic of natural rivers, which may also manifest a certain degree of regularity as exhibited by spectral analyses of the planforms of natural streams (figure 2.1, figure 2.2). Width variations may be originated, in almost straight reaches, by bank erosion induced by bar development and migration; in meandering channels width variations follow closely curvature variations, with a dominant frequency corresponding to half the length of meanders. All the available predicting models of river development are based on the assumption of constant channel width: however, recent experimental results obtained by Bittner (1994) in a laboratory flume with periodically varying width suggest that width variations may induce typical topographic responses and enhance the formation of central bars.

The problem bears both a conceptual and practical relevance. In fact, like the effect of variable curvature in a meandering channel, which constitutes its antisymmetric counterpart, the study of flow field and bottom topography in a channel with periodic width variations represents the model problem for a cohesionless channel subject to a symmetric planimetric forcing. Notice that in the case of meandering channels the forced altimetric response essentially consists of depositional bars displaying a spatial structure similar to that of alternate bars which would spontaneously develop in the channel.

In the present case the forced response exhibits a transverse structure similar to that of central bars. According to the available predicting models, provided the channel be not exceedingly wide, central bars are not expected



Figure 2.1: Width variations in Sunwapta river, Alberta, Canada (flow toward the camera).

to form spontaneously in the absence of some forcing mechanism. Hence, the study of width variations may also turn out to be relevant to understand the process of channel bifurcation, which constitutes one of the unit processes characterizing the dynamic behavior of braided systems. Experimental observations suggest that, whatever be the primary mechanism, the direct formation of a central bar, as suggested by field observations of Leopold & Wolman (1957), or the transition from migrating alternate bars to steady central bars, as documented by flume experiments performed by Ashmore (1982), channel bifurcation is typically the consequence of a central bar deposit.

Width variations may also be important with respect to the interactions they may exhibit with large-scale migrating forms such as bars. It is well known that repetitive sequences of scour holes and depositional diagonal fronts, with vertical scale of the order of the flow depth, develop spontaneously and migrate in straight channels with constant width, provided the width to depth ratio exceed a threshold value which depends on flow and sediment characteristics (Colombini et al. (1987)). Free bars display a variety of possible altimetric patterns depending upon the most unstable transverse mode (alternate, central or multiple rows bars). Theoretical analyses and experimental results suggest that, when the sediment is mainly transported as bed load, the alternate bars configuration is dominant for typical values of the width to depth ratio of the channel. This generally implies that the

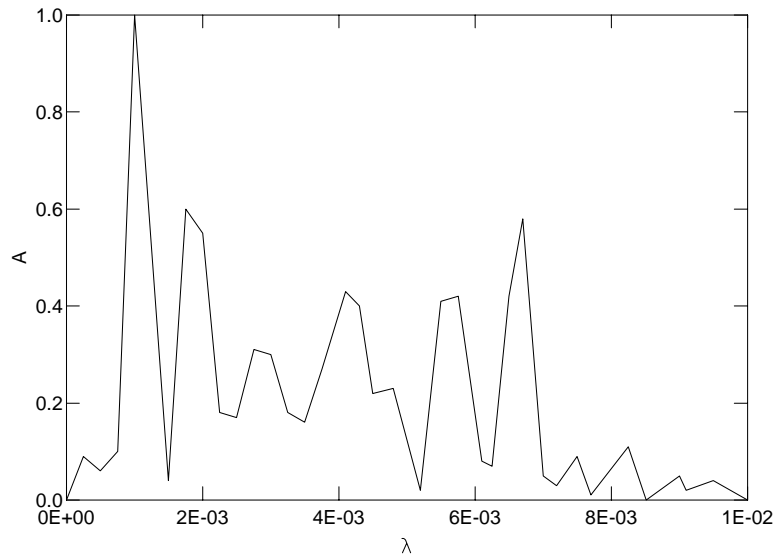


Figure 2.2: Spectral analysis of width variations, Meduna river, Italy (A harmonics amplitude, λ wave number).

associated effects of scour and deposition may be quite large. The latter consideration justifies the attention which has been devoted so far to identify those mechanisms which can inhibit the formation of migrating bars and stabilize bottom topography. Kinoshita & Miwa (1974) first showed that channel sinuosity induces a damping effect on bar formation and migration. They observed both the coexistence of free bars with the forced topography driven by curvature, at low sinuosity, and the suppression of migrating bars for larger values of channel sinuosity. The latter process has been also documented in subsequent laboratory experiments, both in the case of weakly meandering channels (Colombini et al. (1992)) and in the case of large amplitude meanders (Whiting & Dietrich (1993)). The process has been interpreted theoretically by Tubino & Seminara (1990) with reference to a regular sequence of small-amplitude meanders. They found that migrating bars are suppressed provided the maximum channel curvature exceed a threshold value, which essentially depends on the amplitude of bars which would develop in the channel in the absence of the forcing effect of curvature.

In the present chapter the results of experiments performed in a flume with periodic width variations are presented. The attention is focused both on the determination of equilibrium flow field and bed topography in the channel and on the suppressive role of width variations on migrating alternate bars.

2.2 Experimental set up

The experiments were carried out in a flume with a length of 15m and a maximum width of 60cm (figure 2.3) in the Hydraulic Laboratory of the University of Trento. Along both sides of the channel was a 30cm high rail that supported a carriage used for levelling the bed and measuring bottom topography. The rail slope could be regulated at the prescribed value. At the downstream end of the flume a sedimentation tank was placed, with a length of 1.3m. Periodic width variations were constructed inside of the channel, attaching 2.5m long and 0.4m high strips of PVC to wooden profiles, to form vertical flume walls. The banks configuration considered is described by the following relation

$$b^* = b_0^* [1 + a \cos(\lambda_b^* x^*)], \quad (2.1)$$

where b^* and b_0^* are local and average half width, respectively, λ_b^* is the wave number of width variations and finally a is the amplitude of such variations. Three different bank configurations have been tested: their geometrical characteristics are summarized in the following table

λ_b	a
0.5	0.25
0.3	0.25
0.3	0.5

Table 2.1: Realized bank configurations.

where $\lambda_b = \lambda_b^* b_0^*$ is the dimensionless wavenumber of width variations.

The main hydraulic circuit was constituted by

i) a pump with the following characteristics

maximum head $\Delta_{max}=30\text{m}$,

maximum discharge $Q_{max}=59\text{m}^3/\text{h}$;

ii) a PVC delivery pipe DN50;

iii) an electromagnetic discharge meter with a relative precision of $\sim 2\%$;

iv) a 8m^3 downstream tank.

At channel inlet the kinetic energy of the incoming flow was dissipated through a system of metallic meshes. Furthermore, the initial part of the

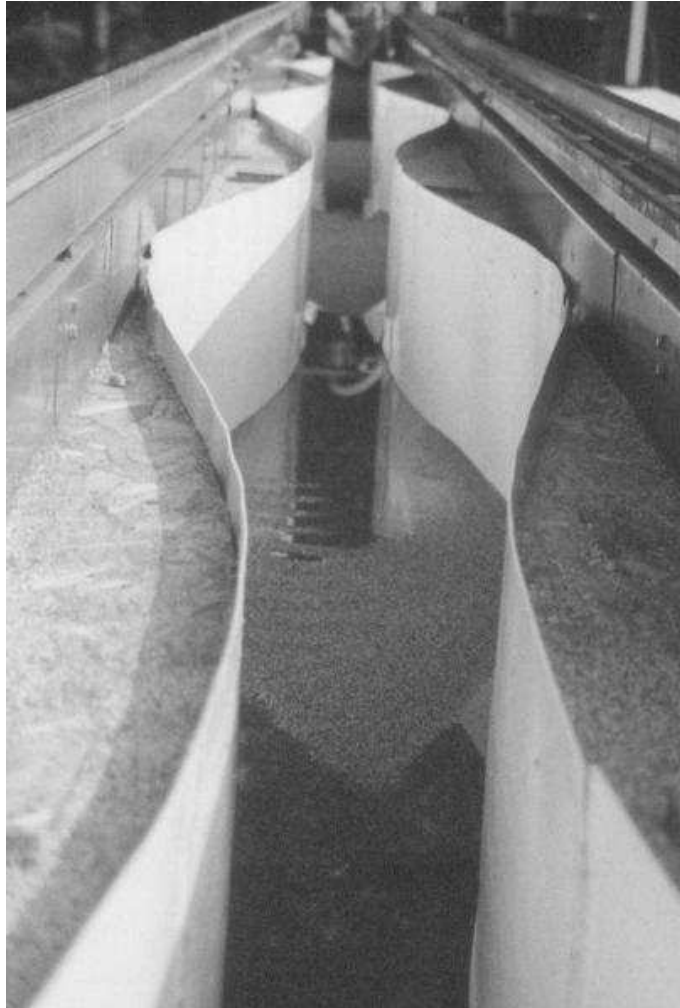


Figure 2.3: Picture of the flume.

flume, for a length of 50cm, was protected with gravel in order to avoid local erosion.

The flume was filled with a well-sorted 1.3mm sediment, recirculated through a cyclone pump from the channel downstream end to a second hydro-cyclone, installed at the head of the flume, where the sediment and the water used to recirculate it were separated. Water level inside of the tank was set using a sluice gate. The cyclone pump was driven by a pump with maximum head $\Delta_{max}=6\text{m}$ and maximum discharge $Q_{max}=200\text{l/min}$.

To evaluate the water level along the channel during each run, eleven piezometers have been placed with a longitudinal spacing of 1.2m.

Bed elevation was surveyed using a laser profiler mounted on a carriage

driven by a motor along longitudinal and transverse directions. The laser is able to survey the bed elevation in the absence of water flow; hence, once a steady condition was achieved, the pumps were switched off and a back-water profile was generated through the downstream tailgate to prevent the dissection of bed topography.

2.3 Experimental runs

2.3.1 Experiments performed

Uniform water and sediment flow in a movable bed channel with a given width, is completely defined once three dimensionless parameters are fixed. The following choice has been adopted herein

$$\beta = \frac{b_0^*}{D_0^*} = \text{width ratio}, \quad (2.2a)$$

$$d_s = \frac{d_s^*}{D_0^*} = \text{grain roughness parameter}, \quad (2.2b)$$

$$\vartheta_0 = \frac{\tau_0^*}{(\rho_s - \rho)gd_s^*} = \text{Shields parameter}, \quad (2.2c)$$

where D_0^* is the uniform water depth, d_s^* is sediment diameter, τ_0^* is bed shear stress, ρ_s and ρ are sediment and water density, respectively and finally g is gravity.

Theoretical approaches to river morphodynamics (see for instance Colombini et al. (1987)) suggest that the width to depth ratio β is the crucial parameter which controls the formation of migrating macro-scale bedforms (alternate or multiple bars); in particular, for given values of ϑ_0 and d_s , it is possible to define a threshold value of β above which such bedforms develop in the channel. One of the main purposes of our experimental study is to understand the role that width variations play on the formation and migration of alternate bars; hence a wide range of values of β have been investigated. However it is not possible, for given channel width, to increase the width/depth ratio of the channel beyond certain values which would imply Shields stresses below the threshold value for sediment movement ϑ_c . The experiments have been performed for different water discharge and slope, which correspond to the following ranges of values of dimensionless parameters

$$5.5 < \beta < 18,$$

$$\vartheta_c < \vartheta_0 < 0.13,$$

$$0.05 < d_s < 0.12.$$

2.3.2 Experimental procedure

In each experiment the following procedure was adopted.

- i) The bed was smoothed flat to the prescribed slope before each experiment using a wide scraper attached to a carriage that ran along the rails.
- ii) Bottom elevation was surveyed with the laser profiler in order to check the exact initial conditions. In each cross section 50 points were measured, with a longitudinal spacing of 10cm.
- iii) A very low discharge was passed over the bed prior to the experiments to prepare a smooth, saturated surface. The required discharge was then achieved.
- iv) During the run the following variables were periodically measured:
 - water discharge,
 - water level along the flume,
 - sediment discharge using a trap placed at the downstream end of the channel.
- v) The shape and position of bedforms in the channel were periodically sketched and the migration speed of bars was estimated.
- vi) Once the bottom had reached a quasi-steady condition the downstream sluice gate was closed and a backwater profile was generated; the flume was then slowly emptied.
- vii) After few minutes, when the bed surface was dry, the bottom elevation was surveyed using the laser profiler, measuring 50 points in each cross section with a longitudinal spacing of 10cm.
- viii) The position and length of each bar in the flume was measured in detail.
- ix) Bottom elevation data have been analyzed through a FFT procedure.

2.4 Experimental results

Two series of experiments have been carried out, which will be described in the following.

2.4.1 Series “a”: suppression of free bars

The first series of experiments, denoted with “a”, was specifically designed in order to ascertain whether or not width variations may have a suppressive role on alternating bars development and migration.

A first set of experiments has been performed in a channel with a constant width of 40cm, for different values of water discharge and slope. In this case the development of regular trains of free migrating bars was observed with dominant wave lengths which fall within the unstable range predicted by the theoretical analysis of Colombini et al. (1987). In a second set of experiments the behavior of free bars in channels with variable width has been investigated, under identical hydraulic conditions and average width of the previous case. The dimensionless wavenumber of width variations λ_b was equal to 0.5 and the maximum width of the channel was equal to 50cm, which corresponds to $a = 0.25$. A complete summary of experimental conditions is reported in table 2.2, where with S is denoted the initial channel slope, with Q the water discharge and with D_0 the uniform flow depth. Furthermore, β_c is the critical value of width/depth ratio above which alternate bars are expected to develop in the channel as predicted by Colombini et al. (1987).

run	S	Q [l/min]	D_0^* [m]	β	β_c	ϑ_0	d_s	λ_b	a
a1	0.007	214.0	0.022	9.22	5.17	0.068	0.062	0.5	0.25
a2	0.007	253.7	0.024	8.36	5.78	0.075	0.056	0.5	0.25
a3	0.010	163.9	0.017	11.91	5.28	0.075	0.080	0.5	0.25
a4	0.010	163.9	0.017	11.91	5.28	0.075	0.080	0.5	0.25
a5	0.010	163.9	0.017	11.91	5.28	0.075	0.080	0.5	0.25
a6	0.010	253.4	0.022	9.27	6.45	0.097	0.063	0.5	0.25
a7	0.015	113.9	0.012	16.42	5.10	0.082	0.111	0.5	0.25
a8	0.015	162.7	0.015	13.42	5.94	0.100	0.091	0.5	0.25
a9	0.015	193.6	0.016	12.15	6.29	0.111	0.082	0.5	0.25
a10	0.015	193.6	0.016	12.15	6.29	0.111	0.082	0.5	0.25
a11	0.015	222.6	0.031	11.22	6.54	0.120	0.076	0.5	0.25

Table 2.2: Summary of experimental conditions of series “a”.

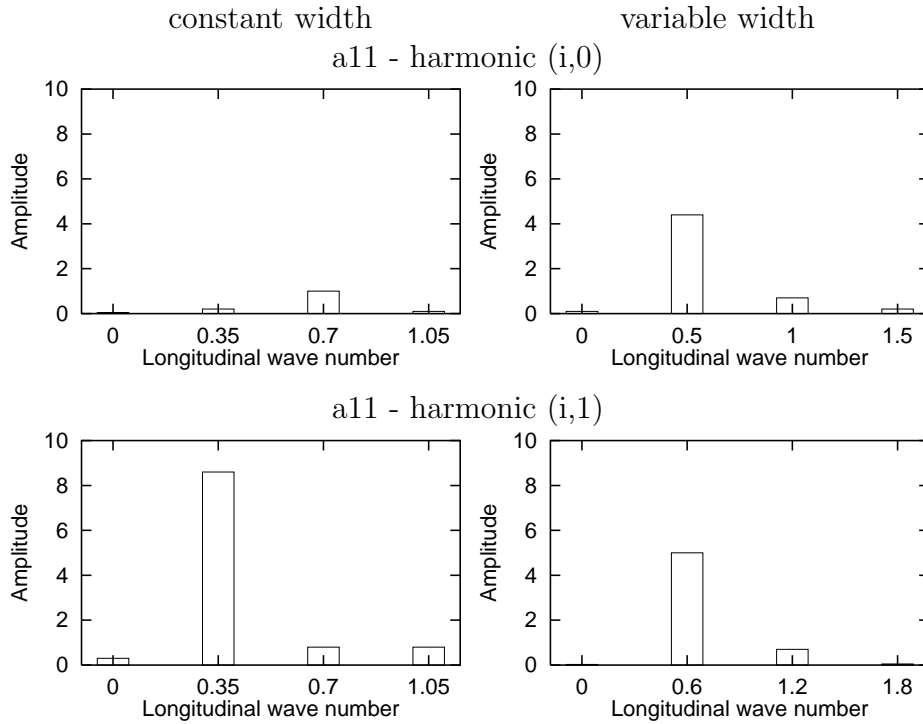


Figure 2.4: Fourier spectra of leading components of bottom elevation (run “a11”).

The beginning of each experiment was usually characterized by the formation of a central bar at the wide sections of the flume. Such bar, once reached a sufficient amplitude, started to migrate downstream with a speed ranging between 5cm/min and 15cm/min, depending on the hydraulic conditions of the experiment. The migration speed was observed to decrease significantly as the front of the bar approached the narrowest section of the flume. Usually the central bar was not able to migrate through the constraint; hence a temporary configuration was established, characterized by sediment transport mainly occurring at channel sides within the narrowest sections and at the centerline within the widest sections. After few minutes, typically, the central bar pattern turned into a configuration characterized by the development of short alternating bars, with a migration speed varying from few cm/min to a maximum of 20cm/min. The development of alternate bars was always irregular and highly unsteady. Regular trains of bars migrating along the full length of the channel have never been detected; rather a pulsating recursive process of formation and obliteration of bars characterized by variable length and height has often been observed.

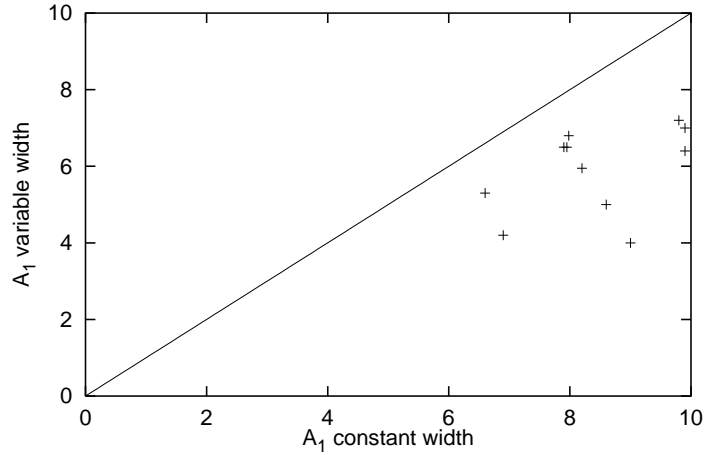


Figure 2.5: Comparison between the amplitudes of the leading harmonic ($i, 1$) (alternate bar mode) measured in the case of constant width channel and in the case of width variations.

An equilibrium bed configuration was never reached; the experiment was stopped and the bottom topography was surveyed with the laser profiler when alternate bars were recognizable in the flume. The following Fourier representation has been adopted to describe bottom topography

$$f(x, y) = \sum_{m=0}^{\infty} \sum_{n=0}^{\infty} A_{mn} \exp(i\lambda x) \exp(iky) + c.c., \quad (2.3)$$

where $\lambda = m\lambda_0$, $k = n\frac{\pi}{2}$ and $\lambda_0 = \frac{2\pi b_0^*}{L_{box}^*}$, being L_{box}^* the box length. Furthermore dimensionless coordinates have been defined as follows

$$x = \frac{x^*}{b_0^*}, \quad y = \frac{y^*}{b^*(x^*)}, \quad (2.4a,b)$$

so that y falls in the range $(-1,1)$. The harmonics with $n = 0$ ($i, 0$) correspond to purely longitudinal deformations of the bed while alternate bars are represented by the harmonics with $n = 1$ ($i, 1$). In figure 2.4 the results of the Fourier analysis of the bed after run “a11” are reported. In the case of constant width channel (plots on the left side) weak purely longitudinal deformations are detected, while migrating alternate bars form with a longitudinal wave number λ equal to 0.35. In the case of periodically variable width the bed displays a strong longitudinal deformation, characterized by deposition at the wide sections and scour at the constraints. This component is directly forced by channel geometry, therefore it exhibits the same wave number of

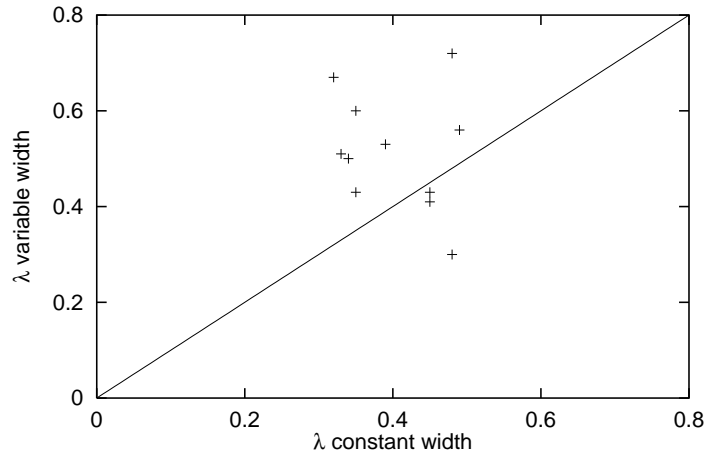


Figure 2.6: Comparison between the wavenumber of bars measured in the case of constant width channel and in the case of width variations.

width variations and its longitudinal profile is almost in phase with respect to banks configuration. Furthermore, it appears, from harmonics $(i, 1)$, that the alternate bars mode is damped with respect to the constant width case and the wave length of bars decreases significantly. In appendix A the complete set of results of the Fourier analyses of bed topography is reported.

In figure 2.5 a comparison is given between alternate bar amplitudes obtained in each experiment, in the case of constant and variable-width channel. It appears that width variations always induce a damping effect on alternate bars amplitude; furthermore, figure 2.6 shows that in the variable width flume, alternate bars display a length which is typically smaller than that found in the case of straight banks: bedforms longer than the wave length of width variations were seldom observed.

2.4.2 Series “b”: forced response

The second series of experiments, denoted with “b” has been mainly devoted to the determination of the forced bed configuration. In this respect, in order to keep only those components of bed deformation which are directly forced by width variations the following Fourier representation of bed elevation has been adopted

$$f(x, y) = \sum_{m=0}^{\infty} \sum_{n=0}^{\infty} A_{mn} \exp(i\lambda x) \exp(iky) + c.c., \quad (2.5)$$

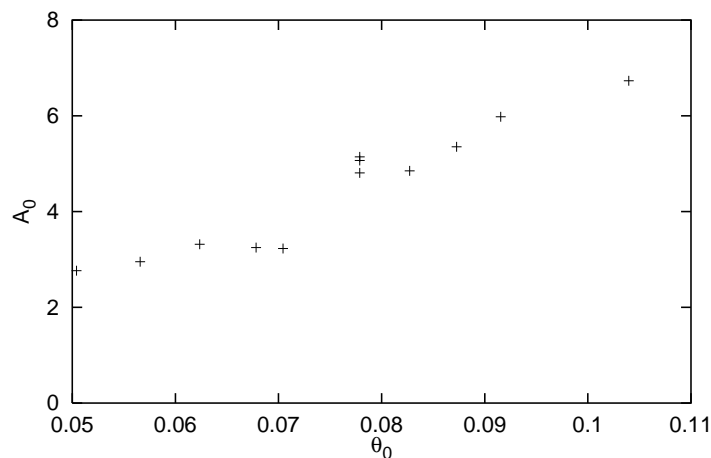


Figure 2.7: Amplitude of the leading purely longitudinal component of bed profile with respect to Shields parameter (experiments b35-b44).

where $\lambda = m\lambda_0$ and $k = n\pi$. In this case the first transverse mode (i,1) corresponds to the central bar configuration.

For variable geometric configurations (different wavelength and amplitude of width variations) the bed displays a strong longitudinal deformation, almost in phase with respect to banks profile, whose amplitude increases with Shields parameter as shown in figure 2.7. On the longitudinal component transverse variations are superimposed and lead to a central bar configuration. Results suggest that periodic width variations may trigger the transition from migrating alternate bars to a steady symmetrical bed configuration (steady central bars) with dominant longitudinal wavenumber equal to that of bank profile. In tables 2.3, 2.4 and 2.5 a complete summary of hydraulic conditions of series “b” experimental runs is reported. In appendix A the full set of experimental results is compared with theoretical findings discussed in the next chapter.

Experiments b60-b67 were characterized by an amplitude a of width variations equal to 0.5: in this case migrating alternate bars were seldom observed in the channel. This result confirms the suppressive role played by width variations on large scale migrating forms.

run	S	Q [l/min]	D_0^* [m]	β	ϑ_0	d_s	λ_b	a
b1	0.007	123.6	0.015	13.46	0.046	0.091	0.5	0.25
b2	0.007	313.6	0.026	7.70	0.081	0.052	0.5	0.25
b3	0.007	313.6	0.026	7.70	0.081	0.052	0.5	0.25
b4	0.007	333.1	0.027	7.43	0.084	0.050	0.5	0.25
b5	0.007	352.7	0.028	7.18	0.087	0.049	0.5	0.25
b6	0.007	372.5	0.029	6.94	0.090	0.047	0.5	0.25
b7	0.007	233.5	0.022	9.19	0.068	0.062	0.5	0.25
b8	0.007	233.5	0.022	9.19	0.068	0.062	0.5	0.25
b9	0.007	253.4	0.023	8.75	0.071	0.059	0.5	0.25
b10	0.007	183.9	0.019	10.61	0.059	0.072	0.5	0.25
b11	0.007	193.9	0.019	10.27	0.061	0.070	0.5	0.25
b12	0.007	313.6	0.026	7.70	0.081	0.052	0.5	0.25
b13	0.01	123.7	0.013	14.97	0.059	0.102	0.5	0.25
b14	0.01	93.8	0.011	17.68	0.050	0.120	0.5	0.25
b15	0.01	214.1	0.019	10.77	0.083	0.073	0.5	0.25
b16	0.01	234.1	0.020	10.21	0.087	0.069	0.5	0.25
b17	0.01	153.8	0.015	13.14	0.068	0.089	0.5	0.25
b18	0.01	214.1	0.019	10.77	0.083	0.073	0.5	0.25
b19	0.01	93.8	0.011	17.68	0.050	0.120	0.5	0.25
b20	0.015	113.9	0.011	17.77	0.075	0.121	0.5	0.25
b21	0.015	113.9	0.011	17.77	0.075	0.121	0.5	0.25
b22	0.015	162.7	0.014	14.35	0.093	0.098	0.5	0.25
b23	0.015	163.8	0.014	14.29	0.094	0.097	0.3	0.25
b24	0.015	213.1	0.016	12.20	0.110	0.083	0.3	0.25
b25	0.015	193.6	0.015	12.93	0.103	0.088	0.3	0.25
b26	0.015	113.9	0.011	17.77	0.075	0.121	0.3	0.25

Table 2.3: Summary of experimental conditions of series “b” (runs b1-b26).

run	S	Q [l/min]	D_0^* [m]	β	ϑ_0	d_s	λ_b	a
b27	0.015	253.1	0.018	11.01	0.121	0.075	0.3	0.25
b28	0.015	133.4	0.012	16.16	0.083	0.110	0.3	0.25
b29	0.015	253.1	0.018	11.01	0.121	0.075	0.3	0.25
b30	0.015	222.8	0.017	11.88	0.112	0.081	0.3	0.25
b31	0.015	163.8	0.014	14.29	0.094	0.097	0.3	0.25
b32	0.015	222.8	0.017	11.88	0.112	0.081	0.3	0.25
b33	0.015	253.1	0.018	11.01	0.121	0.075	0.3	0.25
b34	0.015	113.9	0.011	17.77	0.075	0.121	0.3	0.25
b35	0.01	113.7	0.013	15.75	0.057	0.107	0.3	0.25
b36	0.01	193.6	0.017	11.45	0.078	0.078	0.3	0.25
b37	0.01	163.8	0.016	12.65	0.070	0.086	0.3	0.25
b38	0.01	214.1	0.019	10.77	0.083	0.073	0.3	0.25
b39	0.01	253.5	0.020	9.74	0.091	0.066	0.3	0.25
b40	0.01	133.7	0.014	14.29	0.062	0.097	0.3	0.25
b41	0.01	313.4	0.023	8.57	0.104	0.058	0.3	0.25
b42	0.01	153.8	0.015	13.14	0.068	0.089	0.3	0.25
b43	0.01	234.1	0.020	10.21	0.087	0.069	0.3	0.25
b44	0.01	93.8	0.011	17.68	0.050	0.120	0.3	0.25
b45	0.007	163.8	0.018	11.37	0.055	0.077	0.3	0.25
b46	0.007	214.0	0.021	9.68	0.064	0.066	0.3	0.25
b47	0.007	313.6	0.026	7.70	0.081	0.052	0.3	0.25
b48	0.007	372.5	0.029	6.94	0.090	0.047	0.3	0.25
b49	0.007	193.9	0.019	10.27	0.061	0.070	0.3	0.25
b50	0.007	293.1	0.025	8.02	0.078	0.054	0.3	0.25
b51	0.007	333.9	0.027	7.42	0.084	0.050	0.3	0.25
b52	0.007	323.8	0.026	7.55	0.083	0.051	0.3	0.25

Table 2.4: Summary of experimental conditions of series “b” (runs b27-b52).

run	S	Q [l/min]	D_0^* [m]	β	ϑ_0	d_s	λ_b	a
b53	0.007	303.2	0.025	7.86	0.079	0.053	0.3	0.25
b54	0.007	308.2	0.026	7.78	0.080	0.053	0.3	0.25
b55	0.004	293.7	0.029	6.77	0.053	0.046	0.3	0.25
b56	0.004	314.1	0.031	6.50	0.055	0.044	0.3	0.25
b57	0.004	334.4	0.032	6.26	0.057	0.043	0.3	0.25
b58	0.004	373.2	0.034	5.86	0.061	0.040	0.3	0.25
b59	0.004	412.7	0.036	5.52	0.065	0.037	0.3	0.25
b60	0.004	263.9	0.028	7.22	0.049	0.049	0.3	0.5
b61	0.004	314.1	0.031	6.50	0.055	0.044	0.3	0.5
b62	0.004	214.5	0.024	8.17	0.044	0.056	0.3	0.5
b63	0.007	214.0	0.021	9.68	0.064	0.066	0.3	0.5
b64	0.007	163.8	0.018	11.37	0.055	0.077	0.3	0.5
b65	0.007	163.8	0.018	11.37	0.055	0.077	0.3	0.5
b66	0.007	253.4	0.023	8.75	0.071	0.059	0.3	0.5
b67	0.007	372.5	0.029	6.94	0.090	0.047	0.3	0.5

Table 2.5: Summary of experimental conditions of series “b” (runs b53-b67).

Chapter 3

Flow field and bed topography in channels with variable width

3.1 Introduction

In this chapter some theoretical results are presented regarding the equilibrium flow field and bed topography in channels subject to periodic width variations.

In section 3.2 an analytical two-dimensional model is proposed based on a linearized solution of the problem. The model is able to produce an average bed configuration displaying a good agreement with experimental observations, which predict deposition at the widest section and scour at the channel constrain. However, the model is not suitable to describe the transverse deformation of the bed which comes out from experimental results.

To overcome this difficulty a 3D quasi-analytical model has been developed which is presented in section 3.3. The latter model reproduces as the 2D one the average bottom deformation but it predicts stronger transverse variations of bed profile and of flow velocities. These considerations suggest that three-dimensional effects associated with the generation of secondary flows, are crucial to generate the equilibrium configuration in channels with variable width.

In section 3.4 theoretical findings are compared with experimental results presented in the previous chapter.

In order to understand the generation of secondary flows the two-dimensional model has been corrected taking into account the effect of streamlines curvature on transverse bed shear stress as shown in section 3.5. Results agree fairly satisfactorily with those of the three-dimensional model; however, streamlines curvature doesn't seem to be the only responsible for transverse flow

and bed variations.

In section 3.6 bank stability is investigated in the context of the three-dimensional model, through a simplified approach, which goes back to that originally introduced for meandering channels by Ikeda et al. (1981). The bank erosion model relates the rate of bank retreat to the excess bed stress at the bank induced by flow perturbations which arise as a consequence of width variations; furthermore the channel is assumed to be stable in the absence of the forcing effect due to the variable width. Experimental observations of Ashmore (1982) seem to provide some support to the above hypothesis in that single channels of braided networks reproduced in the laboratory were often found to attain quasi-equilibrium width conditions as defined by Parker (1978). We then neglect several complicating features like the effect of cohesion and vegetation. Furthermore, in order to determine the initial tendency of the flow to enhance planform development, we assume bank erosion to be slow with respect to bottom evolution, which implies that on the time scale of flow and bed development the planimetric configuration is assumed to be steady. The latter hypothesis may turn out not to be adequate when applied to single channels of a braided river with coarse sediment. In this respect present results are to be seen as the appropriate starting point for future investigations where the full coupling between bed and bank development will have to be retained.

Some preliminary results of this work are reported in Repetto & Tubino (1999)a.

3.2 2D depth-averaged model

3.2.1 Formulation of the problem

We consider the flow in a straight cohesionless channel, with average width $2b_0^*$ over which small-amplitude sinusoidal variations are superimposed (see figure 3.1). Hence, the side walls of the channel are described by the following equation

$$y^* = \pm b^* = \pm b_0^* [1 + \delta (e^{i\lambda_b^* x^*} + c.c.)], \quad \delta \ll 1, \quad (3.1a,b)$$

where

$$\lambda_b^* = \frac{2\pi}{L_b^*} \quad (3.2)$$

is the wave number of width variations; furthermore x^* and y^* are longitudinal and transverse coordinate (the asterisks denote dimensional variables that will be let dimensionless in the following). Notice that $\delta = a/2$, being a the amplitude of width variations as defined by equation (2.1).

2D de Saint Venant equations are written in form

$$U_{,t^*}^* + U^* U_{,x^*}^* + V^* U_{,y^*}^* + gH_{,x^*}^* + \frac{\tau_x^*}{\rho D^*} = 0, \quad (3.3a)$$

$$V_{,t^*}^* + U^* V_{,x^*}^* + V^* V_{,y^*}^* + gH_{,y^*}^* + \frac{\tau_y^*}{\rho D^*} = 0, \quad (3.3b)$$

$$D_{,t^*}^* + (U^* D^*)_{,x^*} + (V^* D^*)_{,y^*} = 0, \quad (3.3c)$$

where U^* and V^* are longitudinal and transverse velocity components, t^* is time, H^* water level, D^* water depth, τ_x^* and τ_y^* longitudinal and transverse bottom shear stresses and g gravity.

The flow equations are coupled with the sediment continuity equation, which reads

$$(1 - p)(H^* - D^*)_{,t^*} + q_{x,x^*}^* + q_{y,y^*}^* = 0, \quad (3.4)$$

where q_x^* and q_y^* are sediment flow rate components and p is sediment porosity.

The boundary conditions impose the physical requirement that channel walls be impermeable both to flow and to sediment transport; they read

$$\mathbf{U}^* \cdot \hat{\mathbf{n}}^* = 0, \quad (y^* = \pm b^*), \quad (3.5a)$$

$$\mathbf{q}^* \cdot \hat{\mathbf{n}}^* = 0, \quad (y^* = \pm b^*), \quad (3.5b)$$

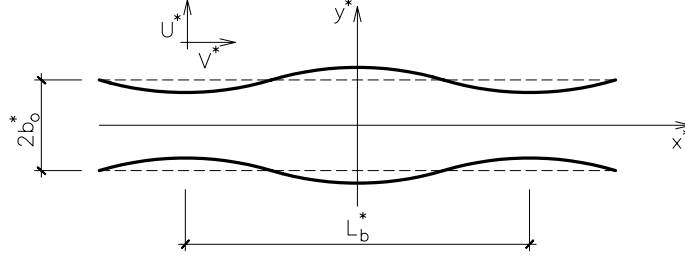


Figure 3.1: Sketch of the geometry and notation.

where $\mathbf{U}^* = (U^*, V^*)$, $\mathbf{q}^* = (q_x^*, q_y^*)$ and $\hat{\mathbf{n}}^*$ is the unit vector normal to the banks. Furthermore, we have to impose the constance of water discharge and average bed elevation along the channel, which read

$$\int_{-b^*}^{b^*} U^* D^* dy^* = Q^*, \quad (3.6a)$$

$$\int_0^{\frac{2\pi}{\lambda_b^*}} \int_{-b^*}^{b^*} (H^* - D^*) dy^* dx^* = \text{const.}, \quad (3.6b)$$

where Q^* is water discharge.

We stretch our physical domain into a rectangle normalizing the transverse coordinate y^* with the local width in the form

$$y = \frac{y^*}{b^*(x^*)}, \quad (3.7)$$

so that y falls in the range $(-1, 1)$.

Let now define dimensionless variables as follows

$$x^* = b_0^* x, \quad (U^*, V^*) = U_0^* (U, V), \quad H^* = D_0^* F_0^2 H,$$

$$D^* = D_0^* D, \quad (\tau_x^*, \tau_y^*) = \rho U_0^{*2} (\tau_x, \tau_y), \quad b^* = b_0^* b,$$

$$(q_x^*, q_y^*) = d_s^* \sqrt{\frac{\rho_s - \rho}{\rho}} g d_s^* (q_x, q_y), \quad t^* = \frac{b_0^*}{U_0^*} t, \quad (3.8a-h)$$

where U_0^* and D_0^* are average speed and depth of a reference uniform flow in the channel with constant width $2b_0^*$, for given water discharge and slope, F_0 is Froude number of the latter flow and ρ is water density. Furthermore ρ_s and d_s^* are sediment density and diameter, respectively.

We look for the steady forced configuration induced by width variations, hence we can neglect the time derivatives in equations (3.3a-c) and (3.4).

In terms of the stretched coordinates (x, y) equations (3.3a-c) and (3.4) are then written in the following dimensionless form

$$bUU_{,x} + VU_{,y} + bH_{,x} + b\frac{\beta\tau_x}{D} - yb_{,x}UU_{,y} - yb_{,x}H_{,y} = 0, \quad (3.9a)$$

$$bUV_{,x} + VV_{,y} + H_{,y} + b\frac{\beta\tau_y}{D} - yb_{,x}UV_{,y} = 0, \quad (3.9b)$$

$$b(UD)_{,x} + (VD)_{,y} - yb_{,x}(UD)_{,y} = 0, \quad (3.9c)$$

$$q_{x,x} + q_{y,y} - yb_{,x}q_{x,y} = 0, \quad (3.9d)$$

where

$$\beta = \frac{b_0^*}{D_0^*} \quad (3.10)$$

is the average width ratio of the channel.

The boundary conditions (3.5a,b) read, in dimensionless form,

$$-Ub_{,x} \pm V = 0, \quad (y = \pm 1), \quad (3.11a)$$

$$-q_x b_{,x} \pm q_y = 0, \quad (y = \pm 1), \quad (3.11b)$$

$$\int_{-1}^1 UD [1 + \delta (e^{i\lambda_b x} + c.c.)] dy = 2, \quad (3.11c)$$

$$\int_0^{\frac{2\pi}{\lambda_b}} \int_{-1}^1 (F_0^2 H - D) [1 + \delta (e^{i\lambda_b x} + c.c.)] dy dx = \text{const.} \quad (3.11d)$$

In order to complete the mathematical formulation of the problem we need to introduce some closures. We then write shear stress components in terms of a friction coefficient C_f in the form

$$(\tau_x, \tau_y) = (U, V) (U^2 + V^2)^{1/2} C_f,$$

$$C_f^{-1/2} = 6 + 2.5 \ln \left(\frac{D}{2.5d_s} \right), \quad d_s = \frac{d_s^*}{D_0^*}. \quad (3.12a-c)$$

We are interested in studying braided rivers, hence we assume the sediment to be mainly transported as bed load. Furthermore, following a well-established procedure (Ikeda (1982); Talmon (1995)) we model the influence

of transverse bed slope on the direction of particles motion in the form

$$(q_x, q_y) = (\cos \alpha, \sin \alpha) \Phi. \quad (3.13)$$

Φ is bed load function, evaluated through Meyer-Peter & Müller (1948) formula which reads

$$\Phi = 8(\vartheta - \vartheta_c)^{3/2}, \quad (3.14)$$

where ϑ is local Shields parameter defined as follows

$$\vartheta = \frac{|\boldsymbol{\tau}^*|}{(\rho_s - \rho)gd_s^*} \quad (3.15)$$

and ϑ_c is the threshold value of Shields parameter below which sediments do not move, assumed equal to 0.047. Finally, following Ikeda (1982), the angle α is expressed through a linear relationship which reads

$$\sin \alpha = V (U^2 + V^2)^{-1/2} - \frac{r}{\beta \vartheta^{1/2}} (F_0^2 H - D)_{,y}, \quad (3.16)$$

where r is an empirical constant ranging between 0.3 and 0.6.

3.2.2 Linear solution

The hypothesis of small-amplitude of width variations, mathematically expressed by (3.1b), allows us to linearize the equations through the following expansion

$$(U, V, H, D) = (1, 0, \bar{H}, 1) + \delta [e^{i\lambda_b x} (U_1, V_1, H_1, D_1) + c.c.] + \mathcal{O}(\delta^2), \quad (3.17)$$

where *c.c.* is the complex conjugate.

At order $\mathcal{O}(\delta^0)$ we find the solution of the basic flow in the $2b_0^*$ wide channel for given slope and water discharge, in the form

$$\frac{d\bar{H}}{dx} = -\beta C_{f0} = -\beta \left[6 + 2.5 \ln \left(\frac{1}{2.5d_s} \right) \right]^{-2} \quad (3.18)$$

and

$$q_{x0} = \Phi_0 = 8(\vartheta_0 - \vartheta_c)^{3/2}. \quad (3.19)$$

At order $\mathcal{O}(\delta)$ the linearized form of equations (3.9a-d) is

$$a_1 U_1 + a_2 H_1 + a_3 D_1 = 0, \quad (3.20a)$$

$$a_4 V_1 + a_5 H_{1,y} = 0, \quad (3.20b)$$

$$a_6 U_1 + V_{1,y} + a_6 D_1 = 0, \quad (3.20c)$$

$$a_7 U_1 + a_8 V_{1,y} + a_9 (D_1 - H_1)_{,yy} + a_{10} D_1 = 0, \quad (3.20d)$$

where the coefficients are defined as follows

$$\begin{aligned} a_1 &= i\lambda_b + 2\beta C_{f0}, & a_2 &= i\lambda_b F_0^{-2}, & a_3 &= \beta C_{f0} (C_D - 1), \\ a_4 &= i\lambda_b + \beta C_{f0}, & a_5 &= F_0^{-2}, & a_6 &= i\lambda_b, \\ a_7 &= 2i\lambda_b \Phi_T, & a_8 &= 1, & a_9 &= \frac{r}{\beta \vartheta_0^{1/2}} = R, \\ a_{10} &= i\lambda_b C_D \Phi_T \end{aligned} \quad (3.21)$$

and

$$C_D = \frac{1}{C_{f0}} \left(\frac{dC_f}{dD} \right)_0, \quad \Phi_T = \frac{\vartheta_0}{\Phi_0} \left(\frac{d\Phi}{d\vartheta} \right)_0. \quad (3.22a,b)$$

The linearized form of the boundary conditions is readily obtained from (3.11a-d) and reads

$$V_1 = \pm i\lambda_b, \quad (y = \pm 1), \quad (3.23a)$$

$$(F_0^2 H_1 - D_1)_{,y} = 0, \quad (y = \pm 1), \quad (3.23b)$$

$$\int_{-1}^1 (U_1 + D_1) dy = -2, \quad (3.23c)$$

$$\int_0^{\frac{2\pi}{\lambda_b}} \int_{-1}^1 (F_0^2 H_1 - D_1 + F_0^2 \bar{H} - 1) e^{i\lambda_b x} dy dx = 0. \quad (3.23d)$$

System (3.20a-d), with the boundary conditions (3.23a,b), can be transformed into an ordinary differential equation of the fourth order. In terms of the variable V_1 we obtain

$$\frac{d^4 V_1}{dy^4} + \Gamma_1 \frac{d^2 V_1}{dy^2} + \Gamma_2 V_1 = 0, \quad (3.24a)$$

$$V_1 = \pm i\lambda_b, \quad y = \pm 1, \quad (3.24b)$$

$$\frac{d^2 V_1}{dy^2} = \pm i \lambda_b \Gamma_3, \quad y = \pm 1, \quad (3.24c)$$

where

$$\Gamma_1 = \frac{1}{a_1 a_{11}} [a_6(a_3 - a_1)(1 + F_0^2 a_4 a_{11}) - a_3 a_9 + a_1 a_{12} + a_2 a_4 a_6 a_{11}], \quad (3.25a)$$

$$\Gamma_2 = \frac{a_2 a_4 a_6}{a_1 a_{11}} (a_{12} - a_9), \quad (3.25b)$$

$$\Gamma_3 = -\frac{a_4 a_6}{a_1} [F_0^2 (a_3 - a_1) + a_2]. \quad (3.25c)$$

Similar problems can be obtained for the other variables (U_1 , H_1 , D_1).

The linear solution is found analytically in the form

$$V_1 = \gamma_1 \sinh(\lambda_1 y) + \gamma_2 \sinh(\lambda_2 y), \quad (3.26a)$$

$$U_1 = \phi_1 \cosh(\lambda_1 y) + \phi_2 \cosh(\lambda_2 y), \quad (3.26b)$$

$$H_1 = \theta_1 \cosh(\lambda_1 y) + \theta_2 \cosh(\lambda_2 y), \quad (3.26c)$$

$$D_1 = \delta_1 \cosh(\lambda_1 y) + \delta_2 \cosh(\lambda_2 y). \quad (3.26d)$$

In equations (3.26a-d) we have defined

$$\lambda_1 = \sqrt{\frac{1}{2} \left(-\Gamma_1 + \sqrt{\Gamma_1^2 - 4\Gamma_2} \right)}, \quad (3.27a)$$

$$\lambda_2 = \sqrt{\frac{1}{2} \left(-\Gamma_1 - \sqrt{\Gamma_1^2 - 4\Gamma_2} \right)} \quad (3.27b)$$

and the coefficients have the following expressions

$$\gamma_1 = \frac{i \lambda_b (\lambda_2^2 - \Gamma_3)}{(\lambda_2^2 - \lambda_1^2) \sinh(\lambda_1)}, \quad \gamma_2 = \frac{i \lambda_b (\lambda_1^2 - \Gamma_3)}{(\lambda_1^2 - \lambda_2^2) \sinh(\lambda_2)},$$

$$\phi_1 = \frac{1}{a_3 - a_1} \left[a_2 \theta_1 - \frac{a_3}{a_6} \lambda_1 \gamma_1 \right], \quad \phi_2 = \frac{1}{a_3 - a_1} \left[a_2 \theta_2 - \frac{a_3}{a_6} \lambda_2 \gamma_2 \right],$$

$$\theta_1 = -a_4 \frac{\gamma_1}{\lambda_1}, \quad \theta_2 = -a_4 \frac{\gamma_2}{\lambda_2},$$

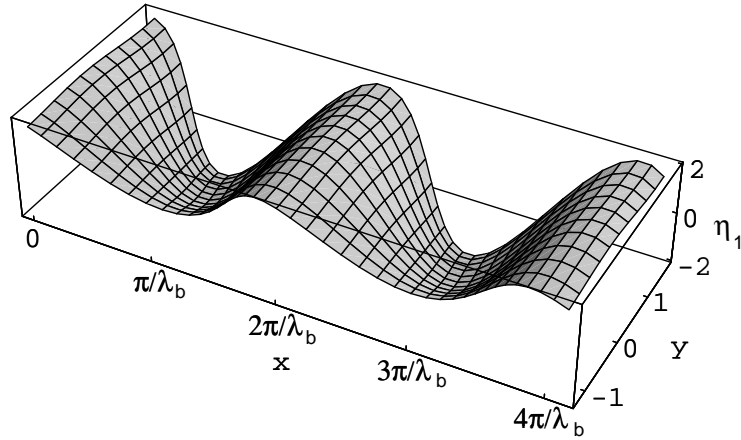


Figure 3.2: Typical equilibrium bed configuration ($\lambda_b = 0.2$, $\beta = 15$, $\vartheta_0 = 0.07$, $d_s = 0.05$).

$$\delta_1 = \frac{1}{a_3 - a_1} \left[\frac{a_1}{a_6} \lambda_1 \gamma_1 - a_2 \theta_1 \right], \quad \delta_2 = \frac{1}{a_3 - a_1} \left[\frac{a_1}{a_6} \lambda_2 \gamma_2 - a_2 \theta_2 \right]. \quad (3.28)$$

In a linear context the conditions (3.23c,d) are automatically satisfied by the solution.

3.2.3 Results

In figure 3.2 a typical equilibrium bed configuration predicted by the theory is plotted (η_1 is the perturbation of bottom elevation). It appears that a strong longitudinal deformation is found, which gives rise to deposition at the wide section and scour at the channel constraint. Figure 3.3 shows that bed profile is nearly in phase with respect to the banks, in agreement with experimental observations of Bittner (1994) and with the results presented in the previous chapter. In this respect present findings do not differ significantly from results which could be obtained through a simpler 1D model; in fact, under steady conditions, deposition within the wide sections is a consequence of the overall mass balance for the water and the sediment. A longitudinal perturbation of cross sectionally averaged velocity is associated with the bed topography, which attains its maximum positive value almost exactly at the narrowest section (figure 3.3).

It is worth to notice that the model doesn't seem to be able to predict the transverse bed deformation which comes out from experimental observations. In fact predicted transverse variations are very weak with respect to the longitudinal variations of bed profile as it is shown in figure 3.4 where

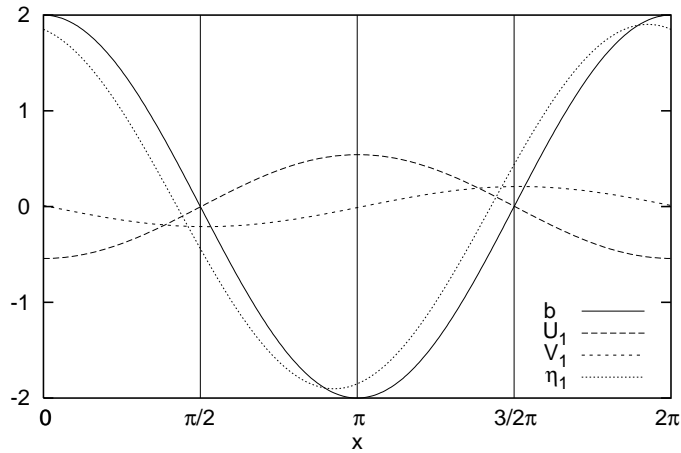


Figure 3.3: Velocity and bed elevation longitudinal profiles ($\lambda_b = 0.2$, $\beta = 15$, $\vartheta_0 = 0.07$, $d_s = 0.05$).

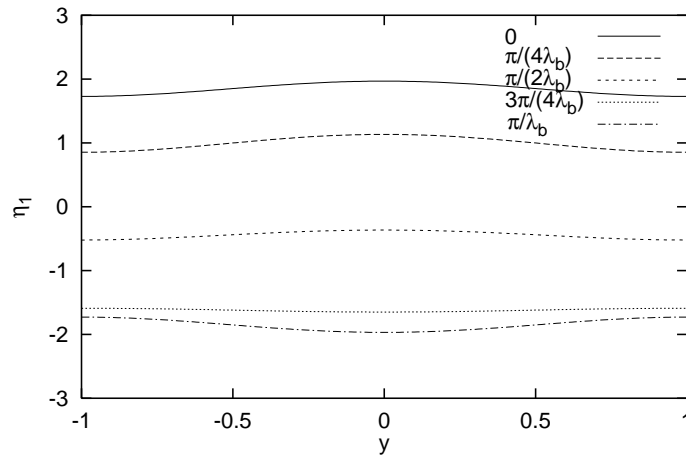


Figure 3.4: Transverse bed profile in different sections ($\lambda_b = 0.2$, $\beta = 15$, $\vartheta_0 = 0.07$, $d_s = 0.05$).

equilibrium bed profiles are plotted for different sections, from the widest (0) to the narrowest one (π/λ_b). To avoid this difficulty a correction to transverse shear stress due to streamlines curvature has been taken in to account as described in section 3.5.

In the context of a linear analysis the solution is no more valid close to resonant conditions. Resonance occurs when the forcing effect of variable planform is such to excite a free response of the channel with the same planimetric structure of the forced pattern. In the case of meandering

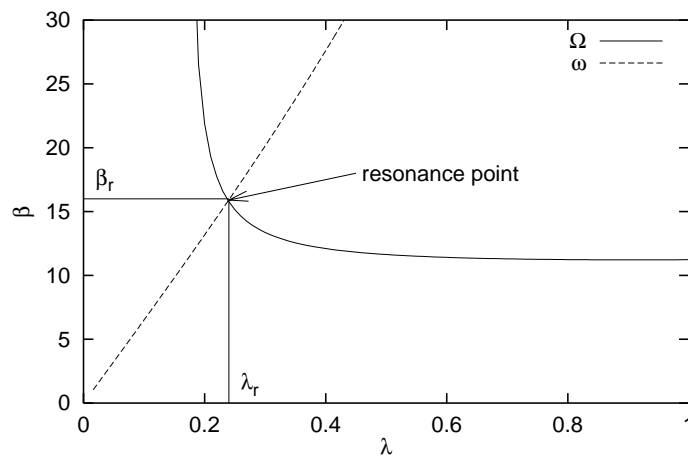


Figure 3.5: Resonance point for central bars in the plane λ, β ($\theta_0 = 0.07$, $d_s = 0.05$).

channels Blondeaux & Seminara (1985) showed that alternate bars could be resonantly excited by channel curvature. In the presence of repetitive width variations the situation is conceptually similar; however, in the latter case the forcing effect is symmetrical and it can only excite symmetrical free forms such as central bars (or higher order even modes).

According to the linear stability theory for free central bars formation, the dispersion relationship allows one to compute the growth rate Ω and the migration speed ω of bars as function of the governing parameters

$$(\Omega, \omega) = f(\vartheta_0, d_s, \beta, \lambda), \quad (3.29)$$

where ϑ_0 , d_s , β , and λ are Shields parameter, grain roughness, width ratio of the basic flow and bars wave number, respectively. Plotting in the plane (β, λ) the curves corresponding to $\Omega = 0$ and $\omega = 0$, as suggested by Colombini et al. (1987), resonance conditions are defined by their intersection (figure 3.5). In other words the free response of the channel is resonantly excited when the wave number of width variations λ_b is equal to λ_r and β is equal to β_r , for given Shields stress and grain roughness.

In figure 3.6 the bottom configuration predicted by the theory close to resonant conditions is shown. It appears that the transverse deformation of bed profile is strongly enhanced and its amplitude tends to infinite when the resonant condition is exactly met. From figure 3.7, in which transverse bed profile is plotted for different cross sections, it is furthermore possible to argue that resonance increases the amplitude of the transverse deformation but does not affect the average longitudinal pattern.

It is interesting to notice that, unlike in the case of meandering channels investigated by Blondeaux & Seminara (1985), here the range of parameters in which resonance affects the results seems to be quite narrow. This is shown in figure 3.8 where the difference between bed elevation at the centerline and at the banks is plotted versus the wave number of width variations.

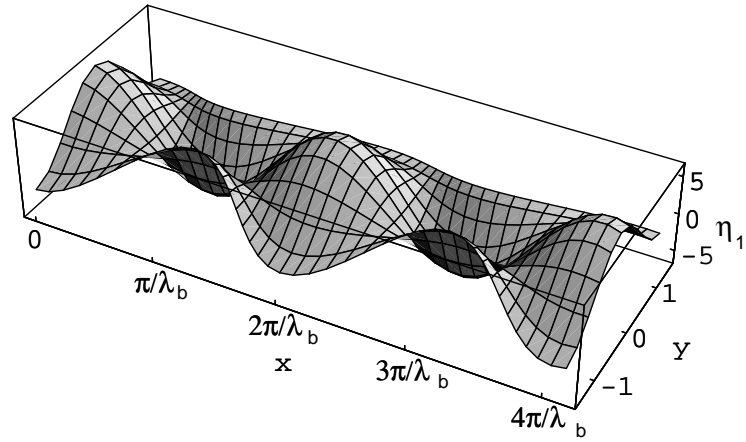


Figure 3.6: Equilibrium bed configuration close to resonant conditions ($\lambda_b = 0.237$, $\beta = 15.9$, $\vartheta_0 = 0.07$, $d_s = 0.05$).

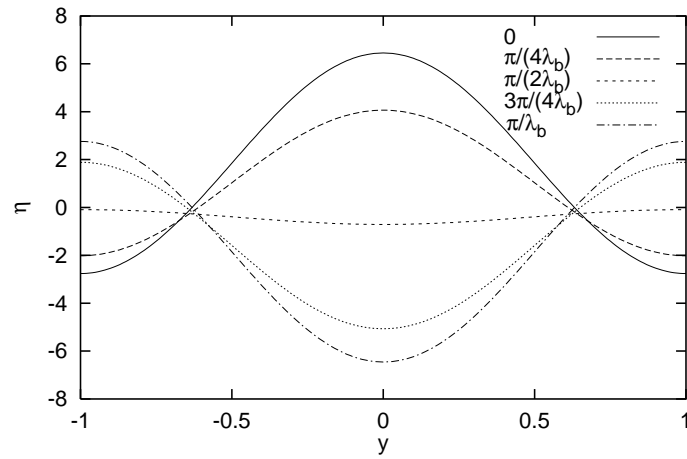


Figure 3.7: Transverse bed profile in different sections ($\lambda_b = 0.237$, $\beta = 15.9$, $\vartheta_0 = 0.07$, $d_s = 0.05$).

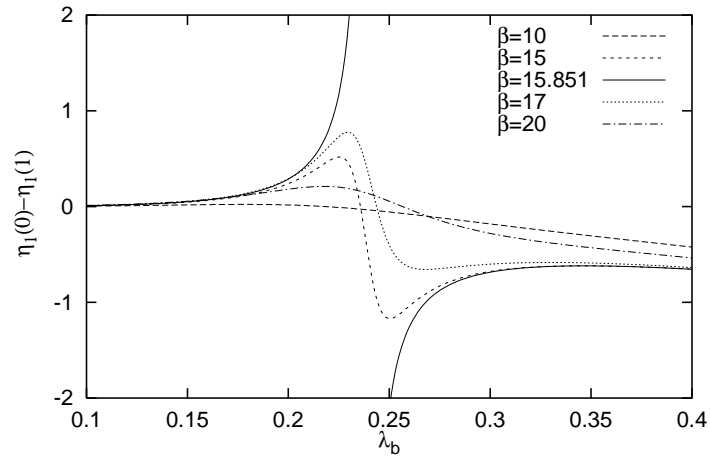


Figure 3.8: Difference between bed elevation at the centerline and the the banks versus width variations wave number λ_b for different values of width parameter β . $\beta = 15.851$ corresponds to the resonant value ($\theta_0 = 0.07$, $d_s = 0.05$).

3.3 3D model

3.3.1 Formulation of the problem

In this section we intend to determine the flow and bed structure of a cohesionless straight channel subject to periodic width variations through a three-dimensional model. Referring to figure 3.9, let x^* , y^* , z^* be the longitudinal, transverse and normal to the average bed coordinates, respectively (super-script asterisks refer to dimensional variables that will be let dimensionless in the following). Furthermore, let u^* , v^* , w^* be the velocity components. The equation describing channel banks is given by (3.1a).

As showed in section 3.2 we work in stretched domain in which the transverse coordinate is normalized with the local width, following equation (3.7).

Dimensionless variables are defined as follows

$$x^* = b_0^* x, \quad (u^*, v^*, w^*) = U_0^* \left(u, v, \frac{w}{\beta} \right), \quad \lambda_b^* = \frac{\lambda_b}{b_0^*},$$

$$(H^*, D^*, z^*) = D_0^* (H, D, z), \quad \nu_t^* = \sqrt{g D_0^* S} D_0^* \nu_t, \quad (3.30a-e)$$

where ν_t is kinematic viscosity and S channel slope. According to the shallow water approximation, dimensionless Reynolds equations in steady conditions are written in the form

$$\begin{aligned} uu_{,x} + (uN_1 + vN_0)u_{,y} + wu_{,z} + F_0^{-2}H_{,x} + \\ -\beta\sqrt{C_{f0}}(\nu_t u_{,z})_{,z} + F_0^{-2}N_1H_{,y} = 0, \end{aligned} \quad (3.31a)$$

$$\begin{aligned} uv_{,x} + (uN_1 + vN_0)v_{,y} + wv_{,z} + \\ -\beta\sqrt{C_{f0}}(\nu_t v_{,z})_{,z} + F_0^{-2}N_0H_{,y} = 0, \end{aligned} \quad (3.31b)$$

$$u_{,x} + N_1u_{,y} + N_0v_{,y} + w_{,z} = 0, \quad (3.31c)$$

where

$$C_{f0} = \frac{gD_0^*S}{U_0^{*2}}, \quad \beta = \frac{b_0^*}{D_0^*}, \quad F_0 = \frac{U_0^*}{\sqrt{gD_0^*}} \quad (3.32a-c)$$

are friction factor, width ratio and Froude number of the basic flow, respectively. Furthermore, $N_0(x)$ and $N_1(x, y)$ are defined in the form

$$N_0(x) = [1 + \delta (e^{i\lambda_b x} + c.c.)]^{-1}, \quad (3.33a)$$

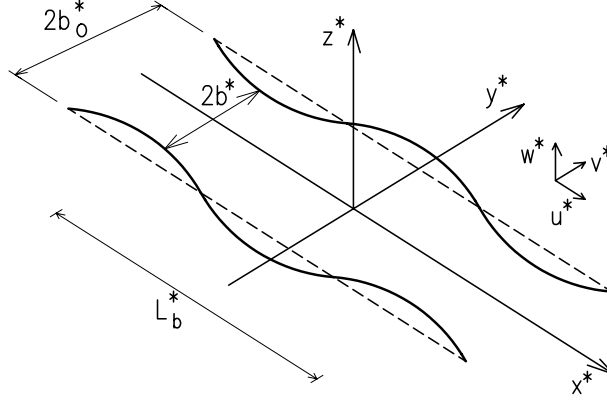


Figure 3.9: Sketch of the geometry and notation.

$$N_1(x, y) = -y (i\lambda_b \delta e^{i\lambda_b x} + c.c.) N_0. \quad (3.33b)$$

The boundary conditions for equations (3.31a-c) read

$$u = v = w = 0, \quad (z = \eta + z_0 D), \quad (3.34a)$$

$$\beta w - (vN_0 + uN_1) H_{,y} - uH_{,x} = 0, \quad (z = H), \quad (3.34b)$$

$$u_{,z} = v_{,z} = 0, \quad (z = H), \quad (3.34c)$$

$$\int_D \mathbf{u} \cdot \hat{\mathbf{n}}_b \, dz = 0, \quad (y = \pm 1), \quad (3.34d)$$

with $\eta = (H - D)$ local bed elevation, \mathbf{u} velocity vector and $\hat{\mathbf{n}}_b$ unit vector normal to the banks. They express the no-slip condition at the bed (with z_0 reference level at which the condition is imposed in uniform flow), the kinematic and dynamic conditions at free surface (in the simplified form which follows from the shallow water approximation) and the kinematic condition at the banks. We assume the bed to be constituted by a uniform sediment of diameter d_s^* and density ρ_s , which is sufficiently coarse to be mainly transported as bed load. The flow equations are then coupled with the sediment continuity equation

$$q_{x,x} + N_1 q_{x,y} + N_0 q_{y,y} = 0, \quad (3.35)$$

where the bedload vector $\mathbf{q} = (q_x, q_y)$ has been made dimensionless using the Einstein (1950) scale

$$\mathbf{q}^* = \mathbf{q} \left(\frac{\rho_s - \rho}{\rho} g d_s^{*3} \right)^{1/2}, \quad (3.36)$$

with the associated boundary conditions which express the requirement of no sediment flux through the banks

$$\mathbf{q} \cdot \hat{\mathbf{n}}_b = 0, \quad (y = \pm 1). \quad (3.37)$$

Notice that the effect of width variations is mainly felt through the dependence on the shape of the banks embodied in the definition of the unit vector appearing in boundary conditions (3.34d) and (3.37).

A slowly varying approach is adopted to introduce the closure relationships which are required to complete the formulation of the problem. Hence, we assume that the closures, given in terms of local values of flow variables, maintain the same structure of the uniform case. We set

$$\nu_t = \sqrt{\frac{C_f}{C_{f0}}} |\mathbf{u}| D \mathcal{N}(\zeta), \quad (3.38)$$

where the vertical structure of turbulent kinematic viscosity is given in terms of the stretched vertical variable ζ according to the relationship proposed by Dean (1974)

$$\mathcal{N}(\zeta) = \frac{k\zeta}{1 + \zeta + 4.68\zeta^2}, \quad \zeta = \frac{z - \eta}{D}, \quad (3.39a,b)$$

with k V. Karman constant. Furthermore friction factor is evaluated through equations (3.12).

Bed load intensity is evaluated through Meyer-Peter & Müller (1948) formula in terms of the local value of Shields parameter

$$\vartheta = \frac{|\boldsymbol{\tau}^*|}{(\rho_s - \rho)gd_s^*}, \quad (3.40)$$

where $\boldsymbol{\tau}^*$ is bottom shear stress. The local bed slope modifies both the intensity and the direction of bedload. The first effect is introduced as a correction of the critical Shields parameter ϑ_c . The second effect is quantified on the basis of experimental observations (Ikeda (1982); Talmon (1995)) which suggest the following estimate for the angle $\hat{\alpha}$ describing the deviation of particle trajectories with respect to the local bed stress vector

$$\tan(\hat{\alpha}) = -\frac{r}{\beta\sqrt{\vartheta}}G, \quad (3.41)$$

where r is an empirical coefficient ranging between 0.3 and 0.6 and G is the local bottom gradient normal to the bed stress vector.

3.3.2 Linearization

We take advantage of the assumption of small amplitude of width variations ($\delta \ll 1$) and expand the solution in the form

$$(u, v, w, H, D) = (u_0, 0, 0, \bar{H}, 1) + \delta [(u', v', w', h, d)e^{i\lambda_b x} + c.c.] + \mathcal{O}(\delta^2), \quad (3.42)$$

where $u_0(\zeta)$ is the velocity profile of the basic uniform flow. Substituting the expansion (3.42) into equations (3.31a-c) and (3.34a-d) and keeping only linear terms, the following differential problem for the variables u' , v' , w' , h and d is obtained

$$(\mathcal{N}v'_{,\zeta})_{,\zeta} - \frac{i\lambda_b u_0 v'}{\beta \sqrt{C_{f0}}} - \frac{h_{,y}}{\beta F_0^2 \sqrt{C_{f0}}} = 0, \quad (3.43a)$$

$$\begin{aligned} (\mathcal{N}u'_{,\zeta})_{,\zeta} - \frac{i\lambda_b u_0 u'}{\beta \sqrt{C_{f0}}} - \sqrt{C_{f0}} \left(\frac{C_D}{2} d + \int_{z_0}^1 u' d\zeta \right) - \frac{u_{0,\zeta} w'}{\beta \sqrt{C_{f0}}} \\ + \frac{i\lambda_b u_0 u_{0,\zeta}}{\beta \sqrt{C_{f0}}} [h - d(1 - \zeta)] - \frac{i\lambda_b h}{\beta F_0^2 \sqrt{C_{f0}}} + \sqrt{C_{f0}} d = 0, \end{aligned} \quad (3.43b)$$

$$w'_{,\zeta} + i\lambda_b u' - i\lambda_b u_{0,\zeta} [h - d(1 - \zeta)] + v'_{,y} = 0, \quad (3.43c)$$

with the boundary conditions

$$w' - i\lambda_b h u_0 = 0 \quad (\zeta = 1), \quad (3.44a)$$

$$v'_{,\zeta} = u'_{,\zeta} = 0 \quad (\zeta = 1), \quad (3.44b)$$

$$u' = v' = w' = 0 \quad (\zeta = z_0), \quad (3.44c)$$

$$\int_{z_0}^1 v' d\zeta = \pm i\lambda_b \quad (y = \pm 1), \quad (3.44d)$$

where

$$C_D = \frac{1}{C_{f0}} \left(\frac{dC_f}{dD} \right)_0. \quad (3.45)$$

The linearized form of bedload components reads

$$q_{sx} = \Phi(\vartheta_G), \quad \vartheta_G = \vartheta - \frac{r_1}{\beta} (\eta_{,x} + N_1 \eta_{,y}),$$

$$q_{sy} = \Phi(\vartheta_0) \left[\left(\frac{\tau_y}{|\boldsymbol{\tau}|} \right)_{z_0} - \frac{r}{\beta\sqrt{\vartheta_0}} N_0 \eta_{,y} \right], \quad (3.46a-c)$$

where Φ is bed load function, $r_1 = \vartheta_c/\mu$, with μ dynamic friction coefficient, and ϑ_0 is Shields parameter of the uniform basic flow. Substituting from (3.46a-c) into sediment continuity equation we obtain

$$i\lambda_b \Phi_T \left[\frac{C_D}{2} d + \int_{z_0}^1 u' d\zeta + \frac{(\mathcal{N}u'_{,\zeta})_{z_0}}{\sqrt{C_{f0}}} \right] + \left(\frac{v'_{,\zeta y}}{u_{0,\zeta}} \right)_{z_0} - \frac{r}{\beta\sqrt{\vartheta_0}} (h-d)_{,yy} = 0, \quad (3.47)$$

with the boundary conditions

$$\left(\frac{v'_{,\zeta}}{u_{0,\zeta}} \right) - \frac{r}{\beta\sqrt{\vartheta_0}} (h-d)_{,y} = \pm i\lambda_b, \quad (y = \pm 1) \quad (3.48)$$

and

$$\Phi_T = \frac{\vartheta_0}{\Phi(\vartheta_0)} \left(\frac{d\Phi}{d\vartheta_G} \right)_{\vartheta_G=\vartheta_0}. \quad (3.49)$$

3.3.3 Solution

Lets define the two new variables

$$\mathcal{F} = \int_{z_0}^{\zeta} u' d\zeta, \quad \mathcal{G} = \int_{z_0}^{\zeta} v' d\zeta \quad (3.50a,b)$$

as the integrals in ζ of longitudinal and transverse velocity components, respectively.

Integrating in ζ continuity equation (3.43c) it is possible to find an explicit expression for the vertical velocity component w' as follows

$$w' = -\mathcal{G}_{,y} - i\lambda_b \mathcal{F} + i\lambda_b d \left[(u_0(\zeta - 1) - \int_{z_0}^{\zeta} u_0 d\zeta) \right] + i\lambda_b h u_0. \quad (3.51)$$

Substituting such expression into equation (3.43b) and applying a derivative in ζ in order to eliminate the term $\int_{z_0}^1 u' d\zeta$, we find a differential problem for the variables \mathcal{F} , \mathcal{G} , in the form

$$\mathcal{G}_{,\zeta\zeta\zeta} = -\frac{\mathcal{N}_{,\zeta}}{\mathcal{N}} \mathcal{G}_{,\zeta\zeta} + \frac{i\lambda_b u_0}{\beta\sqrt{C_{f0}}\mathcal{N}} \mathcal{G}_{,\zeta} + \frac{h_{,y}}{\beta F_0^2 \sqrt{C_{f0}}\mathcal{N}}, \quad (3.52a)$$

$$\mathcal{F}_{,\zeta\zeta\zeta\zeta} = -\frac{2\mathcal{N}_{,\zeta}}{\mathcal{N}} \mathcal{F}_{,\zeta\zeta\zeta} + \frac{1}{\mathcal{N}} \left(\frac{i\lambda_b u_0}{\beta\sqrt{C_{f0}}} - \mathcal{N}_{,\zeta\zeta} \right) \mathcal{F}_{,\zeta\zeta} - \frac{i\lambda_b u_{0,\zeta\zeta}}{\beta\sqrt{C_{f0}}\mathcal{N}} \mathcal{F} +$$

$$\begin{aligned}
& -\frac{u_{0,\zeta\zeta}}{\beta\sqrt{C_{f0}}\mathcal{N}}\mathcal{G}_{,y} - \frac{u_{0,\zeta}}{\beta\sqrt{C_{f0}}\mathcal{N}}\mathcal{G}_{,\zeta y} + \\
& -\frac{i\lambda_b d}{\beta\sqrt{C_{f0}}\mathcal{N}} \left(u_{0,\zeta\zeta} \int_{z_0}^{\zeta} u_0 \, d\zeta + u_0 u_{0,\zeta} \right), \tag{3.52b}
\end{aligned}$$

with the boundary conditions

$$\mathcal{G}_{,\zeta\zeta} = 0, \quad (\zeta = 1), \tag{3.53a}$$

$$\mathcal{G}_{,\zeta} = 0, \quad (\zeta = z_0), \tag{3.53b}$$

$$\mathcal{G} = 0, \quad (\zeta = z_0), \tag{3.53c}$$

$$\begin{aligned}
\mathcal{F}_{,\zeta\zeta\zeta} = & -\frac{\mathcal{N}_{,\zeta}}{\mathcal{N}}\mathcal{F}_{,\zeta\zeta} + \frac{\sqrt{C_{f0}}}{\mathcal{N}} \left(\frac{C_D}{2}d + \mathcal{F}(1) \right) + \\
& + \frac{i\lambda_b h}{\beta F_0^2 \sqrt{C_{f0}}\mathcal{N}} - \frac{\sqrt{C_{f0}}}{\mathcal{N}}d, \quad (\zeta = z_0), \tag{3.53d}
\end{aligned}$$

$$\mathcal{F}_{,\zeta\zeta} = 0, \quad (\zeta = 1), \tag{3.53e}$$

$$\mathcal{F}_{,\zeta} = 0, \quad (\zeta = z_0), \tag{3.53f}$$

$$\mathcal{F} = 0, \quad (\zeta = z_0), \tag{3.53g}$$

$$\mathcal{G} = 0, \quad (\zeta = 1, y = \pm 1). \tag{3.53h}$$

The boundary conditions (3.53h) suggest the following structure for the solution

$$\mathcal{G} = \mathcal{G}_0(\zeta)y + \sum_{m=1}^{\infty} \mathcal{G}_m(\zeta) \sin(m\pi y), \tag{3.54a}$$

$$\begin{aligned}
(\mathcal{F}, h, d) = & [\overline{\mathcal{F}}(\zeta), \overline{h}, \overline{d}] y^2 + \\
& + \sum_{m=0}^{\infty} [\mathcal{F}_m(\zeta), h_m, d_m] \cos(m\pi y). \tag{3.54b}
\end{aligned}$$

Substituting from (3.54a,b) into (3.52a,b), leads to a sequence of ordinary differential problems in the variable ζ , which are solved numerically using a "shooting" procedure along with a IV order Runge-Kutta scheme.

The solution proceeds as follows. At first we determine the vertical structure of \mathcal{G}_0 in the form

$$\mathcal{G}_0(\zeta) = \hat{\mathcal{G}}_0(\zeta)\bar{h}, \quad (3.55)$$

solving the following problem

$$\mathcal{G}_{0,\zeta\zeta\zeta} = -\frac{\mathcal{N}_{,\zeta}}{\mathcal{N}}\mathcal{G}_{0,\zeta\zeta} + \frac{i\lambda_b u_0}{\beta\sqrt{C_{f0}}\mathcal{N}}\mathcal{G}_{0,\zeta} + \frac{2\bar{h}}{\beta F_0^2\sqrt{C_{f0}}\mathcal{N}}, \quad (3.56a)$$

$$\mathcal{G}_{0,\zeta\zeta} = 0, \quad (\zeta = 1), \quad (3.56b)$$

$$\mathcal{G}_{0,\zeta} = 0, \quad (\zeta = z_0), \quad (3.56c)$$

$$\mathcal{G}_0 = 0, \quad (\zeta = z_0). \quad (3.56d)$$

From boundary conditions (3.44d) and (3.48) we evaluate \bar{h} and \bar{d} as follows

$$\bar{h} = \frac{i\lambda}{\hat{\mathcal{G}}(1)}, \quad \bar{d} = \bar{h} + \frac{\beta\sqrt{\vartheta_0}}{2r} \left(i\lambda_b - \frac{\hat{\mathcal{G}}_{0,\zeta\zeta}}{u_{0,\zeta}} \Big|_{z_0} \right). \quad (3.57a,b)$$

We determine $\bar{\mathcal{F}}$ solving the problem

$$\begin{aligned} \bar{\mathcal{F}}_{,\zeta\zeta\zeta\zeta} = & -\frac{2\mathcal{N}_{,\zeta}}{\mathcal{N}}\bar{\mathcal{F}}_{,\zeta\zeta\zeta} + \frac{1}{\mathcal{N}} \left(\frac{i\lambda_b u_0}{\beta\sqrt{C_{f0}}} - \mathcal{N}_{,\zeta\zeta} \right) \bar{\mathcal{F}}_{,\zeta\zeta} - \frac{i\lambda_b u_{0,\zeta\zeta}}{\beta\sqrt{C_{f0}}\mathcal{N}}\bar{\mathcal{F}} + \\ & - \frac{i\lambda_b \bar{d}}{\beta\sqrt{C_{f0}}\mathcal{N}} \left(u_{0,\zeta\zeta} \int_{z_0}^{\zeta} u_0 \, d\zeta + u_0 u_{0,\zeta} \right), \end{aligned} \quad (3.58a)$$

$$\begin{aligned} \bar{\mathcal{F}}_{,\zeta\zeta\zeta} = & -\frac{\mathcal{N}_{,\zeta}}{\mathcal{N}}\bar{\mathcal{F}}_{,\zeta\zeta} + \frac{\sqrt{C_{f0}}}{\mathcal{N}} \left(\frac{C_D}{2}\bar{d} + \bar{\mathcal{F}}(1) \right) + \\ & + \frac{i\lambda_b \bar{h}}{\beta F_0^2\sqrt{C_{f0}}\mathcal{N}} - \frac{\sqrt{C_{f0}}}{\mathcal{N}}\bar{d}, \end{aligned} \quad (\zeta = z_0), \quad (3.58b)$$

$$\bar{\mathcal{F}}_{,\zeta\zeta} = 0, \quad (\zeta = 1), \quad (3.58c)$$

$$\overline{\mathcal{F}}_{,\zeta} = 0, \quad (\zeta = z_0), \quad (3.58d)$$

$$\overline{\mathcal{F}} = 0, \quad (\zeta = z_0). \quad (3.58e)$$

We then solve the problem for \mathcal{F}_0 , d_0 and h_0 which reads

$$\begin{aligned} \mathcal{F}_{0,\zeta\zeta\zeta\zeta} = & -\frac{2\mathcal{N}_{,\zeta}}{\mathcal{N}}\mathcal{F}_{0,\zeta\zeta\zeta} + \frac{1}{\mathcal{N}} \left(\frac{i\lambda_b u_0}{\beta\sqrt{C_{f0}}} - \mathcal{N}_{,\zeta\zeta} \right) \mathcal{F}_{0,\zeta\zeta} - \frac{i\lambda_b u_{0,\zeta\zeta}}{\beta\sqrt{C_{f0}}\mathcal{N}}\mathcal{F}_0 + \\ & - \frac{u_{0,\zeta\zeta}}{\beta\sqrt{C_{f0}}\mathcal{N}}\mathcal{G}_0 - \frac{u_{0,\zeta}}{\beta\sqrt{C_{f0}}\mathcal{N}}\mathcal{G}_{0,\zeta} + \\ & - \frac{i\lambda_b d_0}{\beta\sqrt{C_{f0}}\mathcal{N}} \left(u_{0,\zeta\zeta} \int_{z_0}^{\zeta} u_0 \, d\zeta + u_0 u_{0,\zeta} \right), \end{aligned} \quad (3.59a)$$

$$\begin{aligned} \mathcal{F}_{0,\zeta\zeta\zeta} = & -\frac{\mathcal{N}_{,\zeta}}{\mathcal{N}}\mathcal{F}_{0,\zeta\zeta} + \frac{\sqrt{C_{f0}}}{\mathcal{N}} \left(\frac{C_D}{2}d_0 + \mathcal{F}_0(1) \right) + \\ & + \frac{i\lambda_b h_0}{\beta F_0^2 \sqrt{C_{f0}}\mathcal{N}} - \frac{\sqrt{C_{f0}}}{\mathcal{N}}d_0, \end{aligned} \quad (\zeta = z_0), \quad (3.59b)$$

$$\mathcal{F}_{0,\zeta\zeta} = 0, \quad (\zeta = 1), \quad (3.59c)$$

$$\mathcal{F}_{0,\zeta} = 0, \quad (\zeta = z_0), \quad (3.59d)$$

$$\mathcal{F}_0 = 0, \quad (\zeta = z_0). \quad (3.59e)$$

The unknowns h_0 , d_0 can be determined through kinematic condition (3.44a), where w' has been substituted through (3.51), and Exner equation (3.47).

The generic \mathcal{G}_m is then computed in terms of h_m and d_m through the following system

$$\mathcal{G}_{m,\zeta\zeta\zeta\zeta} = -\frac{\mathcal{N}_{,\zeta}}{\mathcal{N}}\mathcal{G}_{m,\zeta\zeta\zeta} + \frac{i\lambda_b u_0}{\beta\sqrt{C_{f0}}\mathcal{N}}\mathcal{G}_{m,\zeta} - \frac{m\pi h_m}{\beta F_0^2 \sqrt{C_{f0}}\mathcal{N}} = 0, \quad (3.60a)$$

$$\mathcal{G}_{m,\zeta\zeta} = 0, \quad (\zeta = 1), \quad (3.60b)$$

$$\mathcal{G}_{m,\zeta} = 0, \quad (\zeta = z_0), \quad (3.60c)$$

$$\mathcal{G}_m = 0, \quad (\zeta = z_0). \quad (3.60d)$$

Furthermore, \mathcal{F}_m can be found in terms of h_m and d_m solving the following problem

$$\begin{aligned} \mathcal{F}_{m,\zeta\zeta\zeta} = & -\frac{2\mathcal{N}_{,\zeta}}{\mathcal{N}}\mathcal{F}_{m,\zeta\zeta} + \frac{1}{\mathcal{N}} \left(\frac{i\lambda_b u_0}{\beta\sqrt{C_{f0}}} - \mathcal{N}_{,\zeta\zeta} \right) \mathcal{F}_{m,\zeta\zeta} - \frac{i\lambda_b u_{0,\zeta\zeta}}{\beta\sqrt{C_{f0}}\mathcal{N}}\mathcal{F}_m + \\ & - \frac{m\pi u_{0,\zeta\zeta}}{\beta\sqrt{C_{f0}}\mathcal{N}}\mathcal{G}_m - \frac{m\pi u_{0,\zeta}}{\beta\sqrt{C_{f0}}\mathcal{N}}\mathcal{G}_{m,\zeta} + \\ & - \frac{i\lambda_b d_m}{\beta\sqrt{C_{f0}}\mathcal{N}} \left(u_{0,\zeta\zeta} \int_{z_0}^{\zeta} u_0 \, d\zeta + u_0 u_{0,\zeta} \right), \end{aligned} \quad (3.61a)$$

$$\begin{aligned} \mathcal{F}_{m,\zeta\zeta} = & -\frac{\mathcal{N}_{,\zeta}}{\mathcal{N}}\mathcal{F}_{m,\zeta} + \frac{\sqrt{C_{f0}}}{\mathcal{N}} \left(\frac{C_D}{2} d_m + \mathcal{F}_m(1) \right) + \\ & + \frac{i\lambda_b h_m}{\beta F_0^2 \sqrt{C_{f0}}\mathcal{N}} - \frac{\sqrt{C_{f0}}}{\mathcal{N}} d_m, \end{aligned} \quad (\zeta = z_0), \quad (3.61b)$$

$$\mathcal{F}_{m,\zeta\zeta} = 0, \quad (\zeta = 1), \quad (3.61c)$$

$$\mathcal{F}_{m,\zeta} = 0, \quad (\zeta = z_0), \quad (3.61d)$$

$$\mathcal{F}_m = 0, \quad (\zeta = z_0), \quad (3.61e)$$

Finally h_m and d_m are computed using again the kinematic condition (3.44a), where w' has been substituted through (3.51), and Exner equation (3.47).

3.3.4 Results

In figure 3.10a-d typical bottom configurations induced by width variations are plotted, for increasing values of λ_b . The results of the Fourier analysis of bottom elevation η , reported in figure 3.11a-d, suggest that the bed profile is mainly characterized by two leading harmonics. The first component represents a purely longitudinal oscillation of the bed, constant in the transverse direction, which gives rise to deposition at the wide section and scour at the channel constraint: bed topography is nearly in phase with respect to bank profile in agreement with the experimental observations of Bittner (1994) and

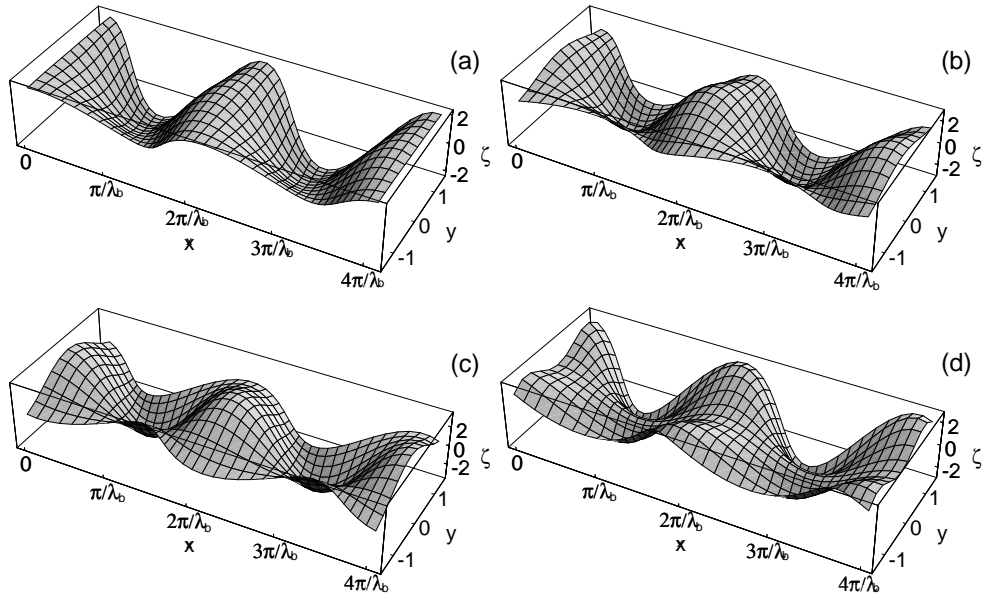


Figure 3.10: Equilibrium bed configurations for different values of the wavenumber of width variations. (a) $\lambda_b = 0.1$, (b) $\lambda_b = 0.2$, (c) $\lambda_b = 0.3$, (d) $\lambda_b = 0.5$ ($\vartheta_0 = 0.1$, $d_s = 0.05$, $\beta = 10$).

with the results presented in the previous chapter. The purely longitudinal component predicted by the 3D model does not differ significantly from that computed with the 2D one (figure 3.11e-h).

The second leading component of bottom topography implies a transverse deformation of the bed in the form of a central bar. Its relative importance with respect to the previous one increases with the wave number λ_b of width variations: for typical values of the control parameters β , ϑ_0 and d_s it reaches a maximum for $\lambda_b \sim 0.3$ (figure 3.11a-d). The relative position of the maximum of the transverse component with respect to the widest section changes significantly with the wavenumber of width variations: as λ_b increases the peak of the transverse component moves from an upstream to a downstream location with respect to the peak of the longitudinal component. When $\lambda_b \sim 0.5$ the phase shift becomes so large that the two leading components of bottom topography are nearly out of phase as appears from figure 3.10d.

It is worth pointing out that the transverse deformation of the bed, which also implies a transverse variation of longitudinal velocity (figure 3.12a-d), is mainly related to three dimensional effects. In fact, the comparison between 3D and 2D results, which are reported in figures 3.11 and 3.12, displays a strong difference in harmonic-1 amplitude both for bed elevation and for longitudinal velocity component. Hence, the generation of a central bar in

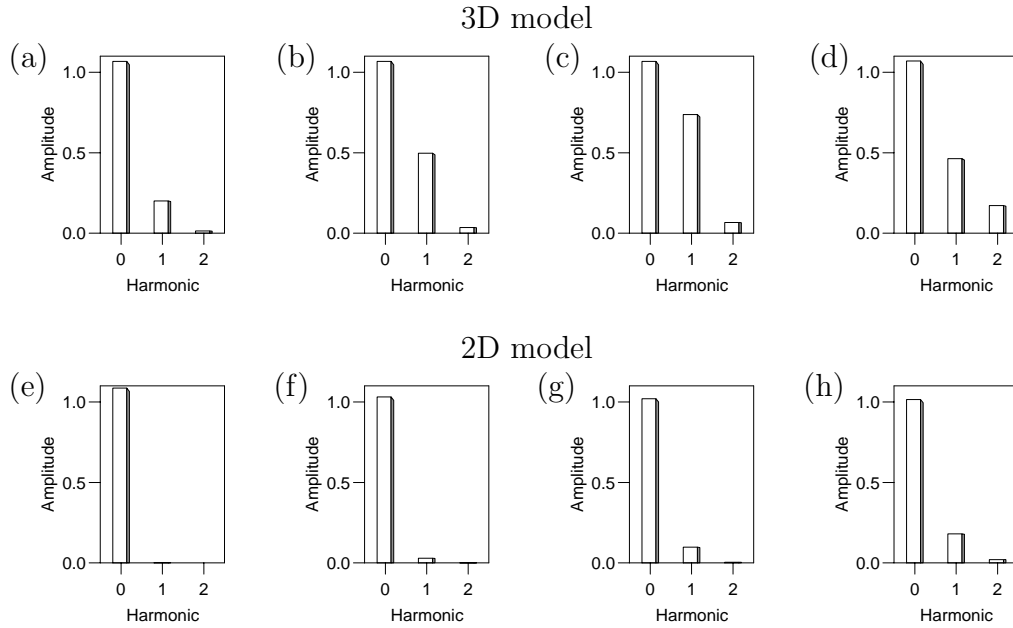


Figure 3.11: Fourier analysis of bottom profile: amplitude of the first three harmonics obtained with the 3D and the 2D models, respectively. (a), (e) $\lambda_b = 0.1$; (b), (f) $\lambda_b = 0.2$; (c), (g) $\lambda_b = 0.3$; (d), (h) $\lambda_b = 0.5$ ($\vartheta_0 = 0.1$, $d_s = 0.05$, $\beta = 10$).

the widest part of the channel, and the related effect of flow divergence, is inherently associated with secondary flows. Such secondary flows can be driven by convective terms and by streamlines curvature. The latter effect is investigated in the following section in which the 2D model has been suitably corrected.

Let now consider the role of convective terms on secondary flow generation. A circulation on the plane (y, z) is triggered by the convective term appearing in equation (3.43a), which vanishes at the bed and reaches its maximum at the free surface. This implies a phase shift in the response of transverse velocity to the variable planform as illustrated in figure 3.13a: just downstream the narrowest section the transverse velocity at the bottom is already directed outward while streamlines are still converging at the free surface. The resulting circulation, which is sketched in figure 3.13b, induces a transverse deformation of the bed (figure 3.13c) which in turn affects the transverse distribution of longitudinal velocity. A similar mechanism operates in the widest section, thus promoting the formation of a central bar.

In figure 3.14 the velocity field on the plane (y, z) at the narrowest section is plotted, showing a secondary circulation. The local depth-averaged value has been filtered out from transverse velocity component.

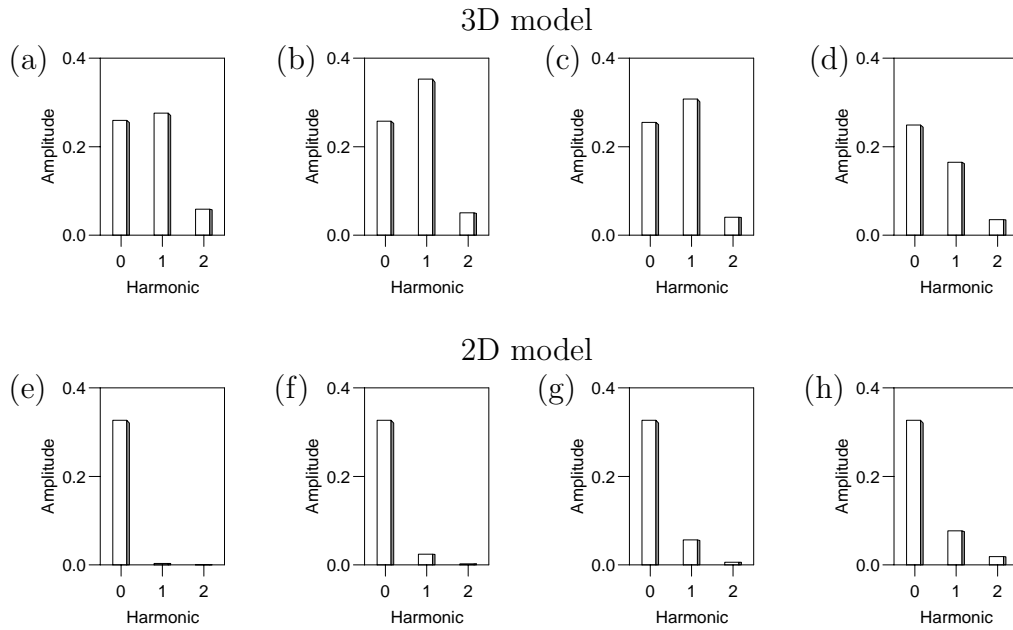


Figure 3.12: Fourier analysis of longitudinal velocity: amplitude of the first three harmonics obtained with the 3D and the 2D models, respectively. (a), (e) $\lambda_b = 0.1$; (b), (f) $\lambda_b = 0.2$; (c), (g) $\lambda_b = 0.3$; (d), (h) $\lambda_b = 0.5$ ($\vartheta_0 = 0.1$, $d_s = 0.05$, $\beta = 10$).

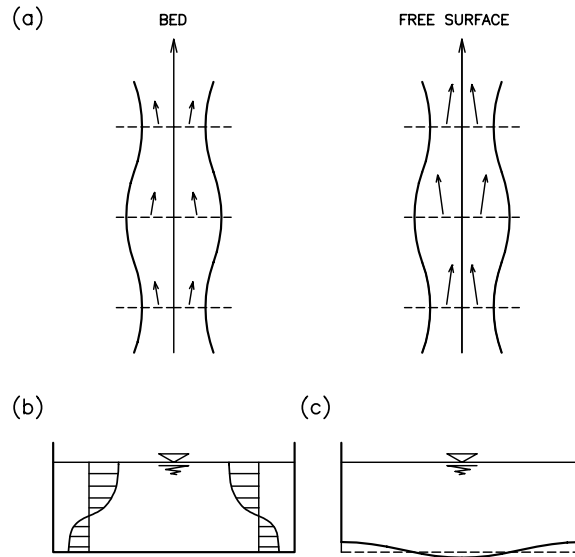


Figure 3.13: (a) Mechanism of generation of secondary flow in the plane (y,z) , (b), (c) secondary flow and bed deformation at the narrowest section.

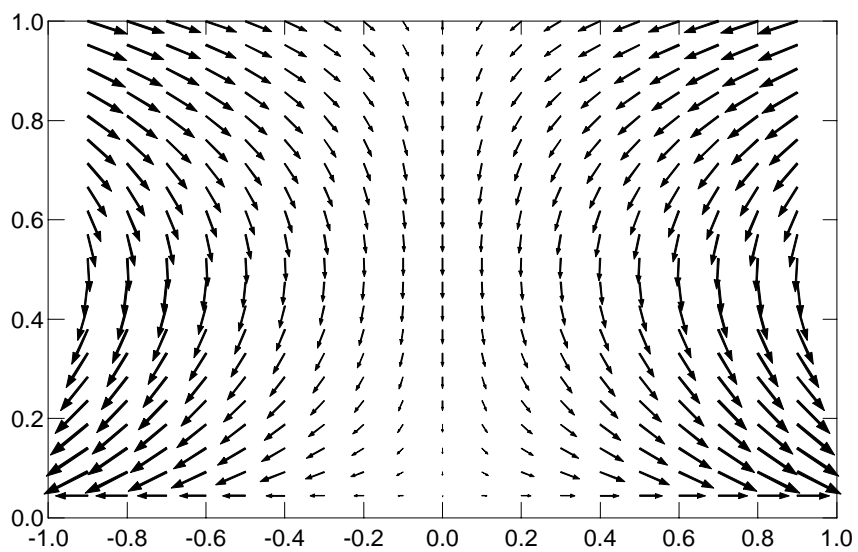


Figure 3.14: Secondary flow at the narrowest section ($\beta = 10$, $\lambda_b = 0.2$, $\vartheta_0 = 0.1$, $d_s = 0.05$).

3.4 Comparison with experimental results

In this section theoretical results are compared with experimental findings presented in chapter 2 (series “b”). In figure 3.15, the theoretical and experimental amplitudes of the first two transverse harmonics of the Fourier representation of bed topography are compared (harmonic 0 represents purely longitudinal deformations and harmonic 1 the central bar mode, with the same longitudinal wavenumber which coincides with λ_b). Each plot corresponds to a different geometric configuration of the banks.

As for the harmonic 0 the agreement is satisfactory in all cases; for $\delta = 0.25$ the theory slightly underestimates the values of longitudinal bed deformation. Notice, however, that in the latter conditions, being the amplitude of width variations relatively large, a linearized theory may turn out to be not completely adequate to describe the solution: non linear effects may be responsible for the small differences detected.

As for the amplitude of the central bar mode, the results must be considered with more care. Figures 3.16, 3.17 and 3.18 report the amplitude of the first two harmonics of bottom configuration plotted versus Shields parameter; theoretical findings are denoted by continuous lines. Each plot corresponds to a different initial bed slope. The amplitude of the central bar mode predicted by the theory agrees with the experimental results at high values of Shields parameter while the agreement is less satisfactory close to the critical conditions for sediment movement. Notice, however, that in the latter case the flume was often partially transporting sediment and emersion of bars occurred frequently: under these conditions the theory is not likely to be applicable. Furthermore, for suitable values of the controlling parameters, the theory displays a resonant response (figure 3.17) and the predicted bed elevation tends to infinite: in these cases a linear approach is no longer valid and a non linear analysis, like that proposed by Seminara & Tubino (1992) for meandering channels, is required.

In appendix A the results of Fourier analyses of experimental bed topography are reported together with a comparison with theoretical findings for all the runs of series “b”. A_{exp} and A_{th} denote the experimental and theoretical amplitudes of each harmonic of bed profile, respectively. In the plots theoretical results are indicated with continuous lines.

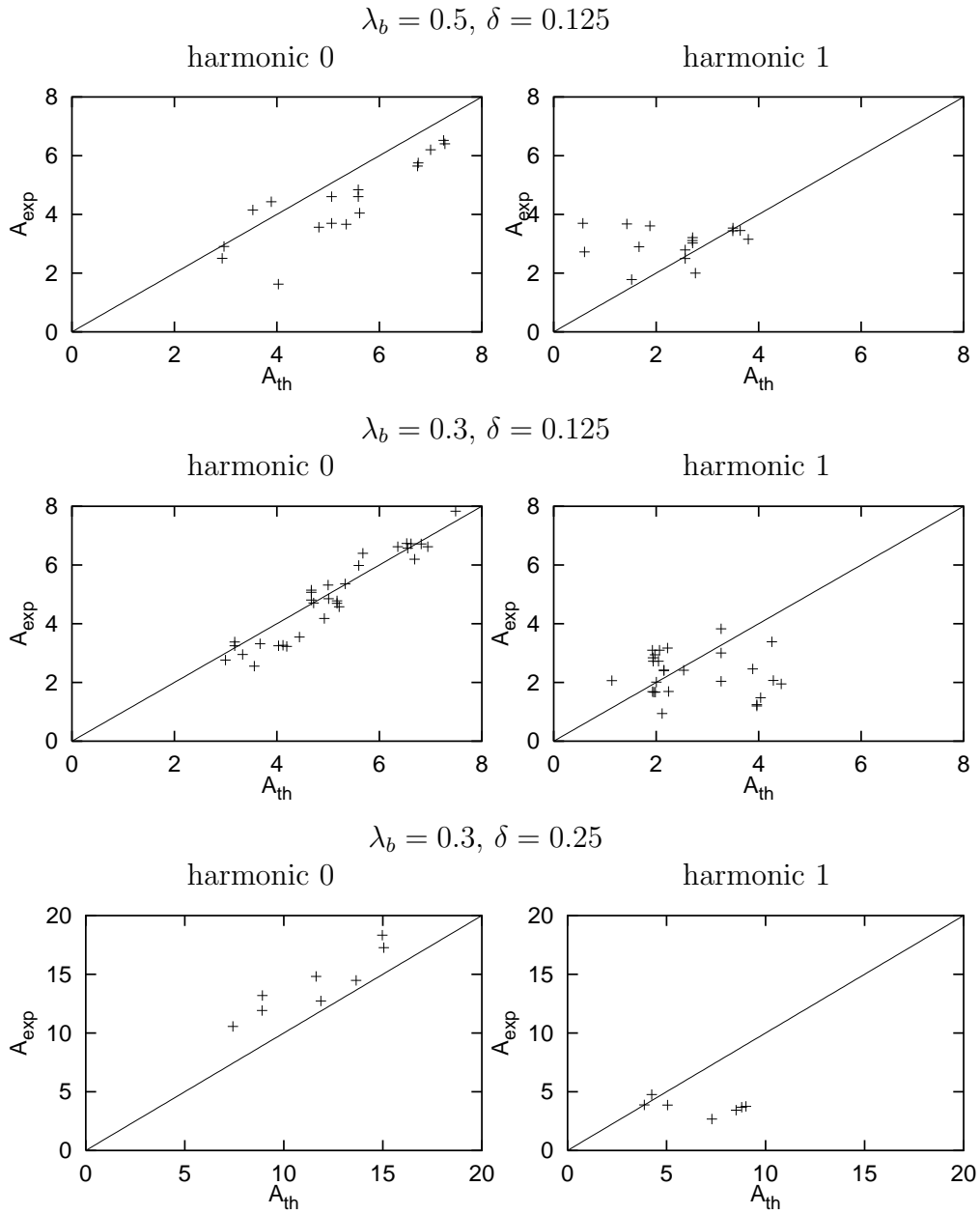


Figure 3.15: Comparison between the first two transverse harmonics of the Fourier representation of the bed predicted by the theory and the experiments.

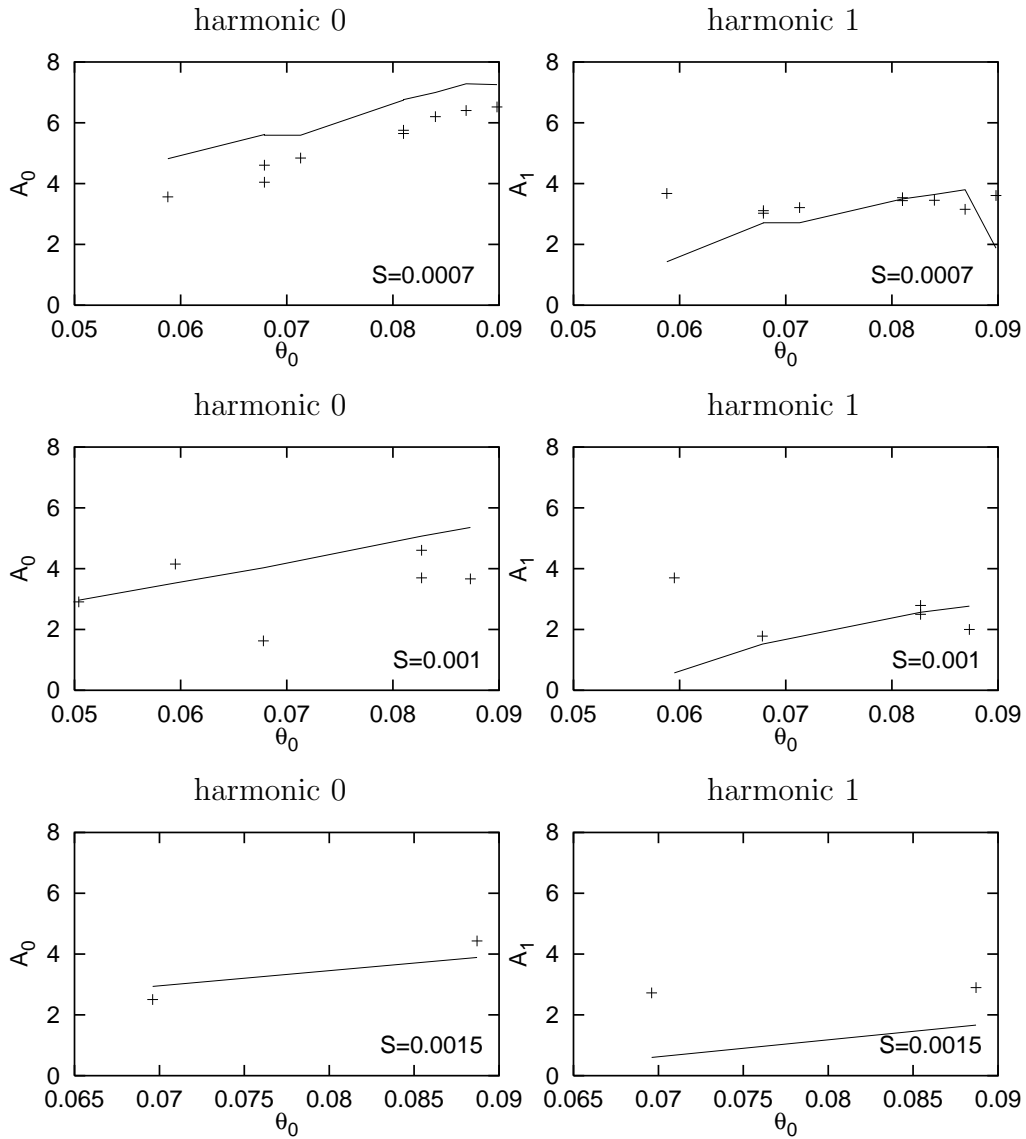


Figure 3.16: Amplitude of the first two transverse harmonics of the Fourier representation of bed topography ($\lambda_b = 0.5$, $\delta = 0.125$).

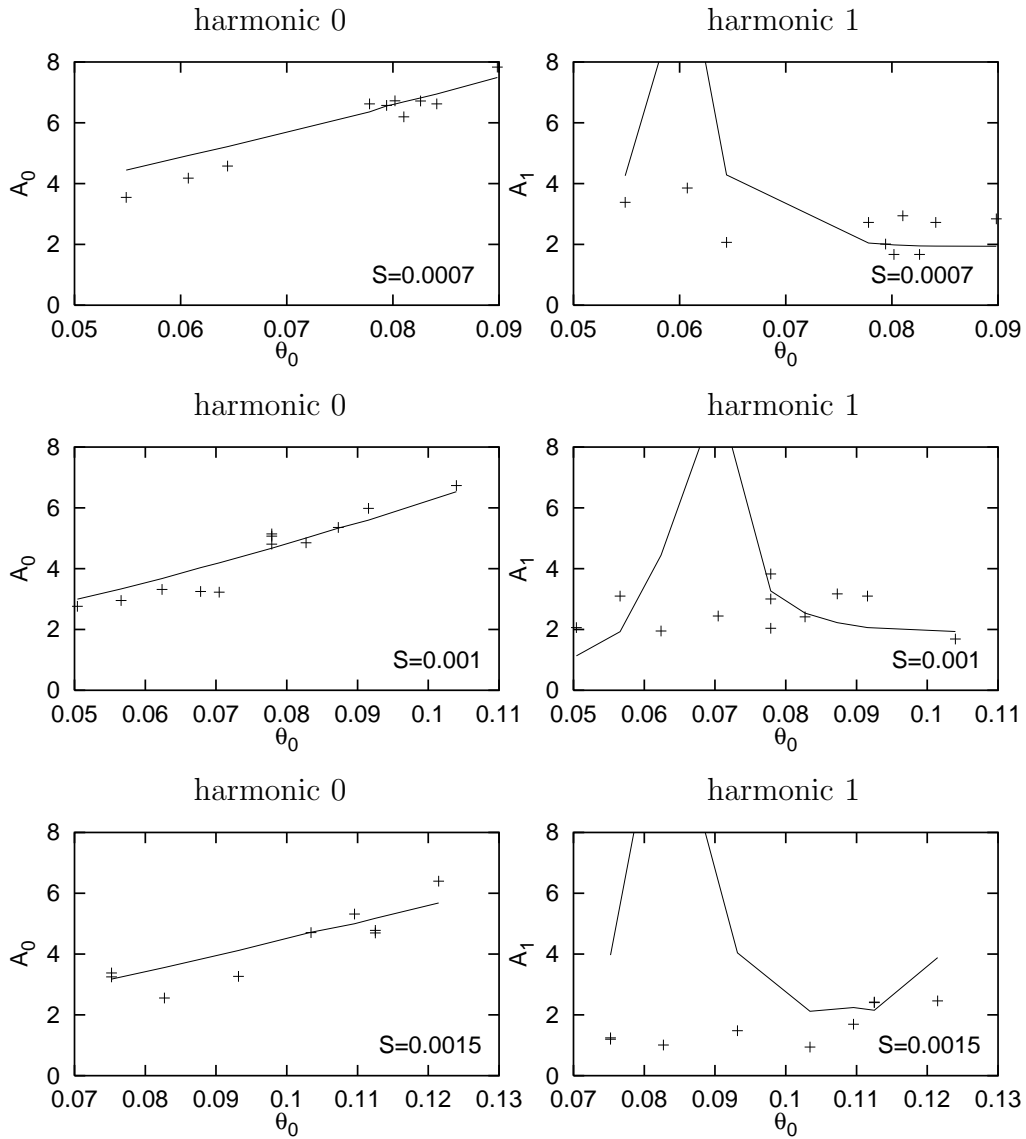


Figure 3.17: Amplitude of the first two transverse harmonics of the Fourier representation of bed topography ($\lambda_b = 0.3$, $\delta = 0.125$).

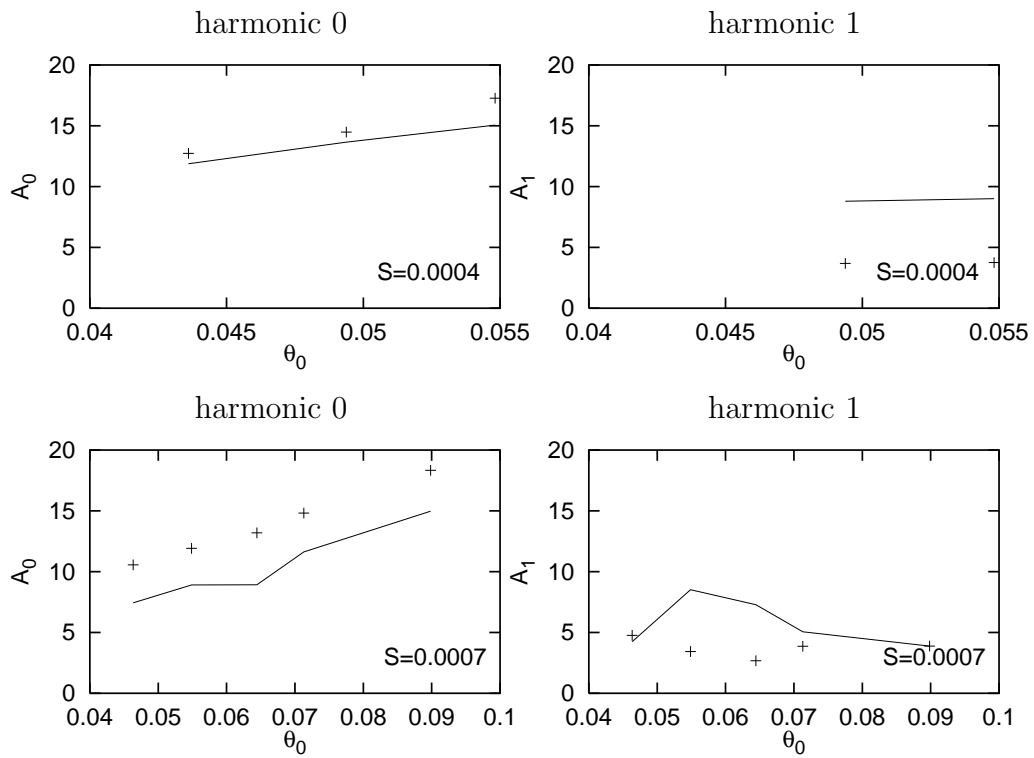


Figure 3.18: Amplitude of the first two transverse harmonics of the Fourier representation of bed topography ($\lambda_b = 0.3$, $\delta = 0.25$).

3.5 Correction due to the streamlines curvature effect on transverse bed shear stress

In this section we correct the 2D model formulated in section 3.2 in order to take into account the effect of streamlines curvature on transverse bottom shear stress.

The curvature radius r_c of streamlines is defined by the following equation

$$\frac{1}{r_c} = \frac{-\left(\frac{V}{U}\right)_{,x}}{\left[1 + \left(\frac{V}{U}\right)^2\right]^{3/2}}. \quad (3.62)$$

Ideas originally developed by Engelund (1974) are followed: the transverse velocity component is decomposed into a helical component with no net flux and a depth-averaged component. The suitability of the above decomposition has been demonstrated by Johannesson & Parker (1989) who showed that, for typical natural channels, the equations governing the above two components of transverse velocity are not directly coupled to each other, at least within a linear context, the helical component being essentially driven by curvature. Following Tubino & Seminara (1990) and referring to a meandering channel with wavenumber λ_m , we denote the vertical distributions of these transverse components by Γ_0 and Γ_1 and the vertical distribution associated with the longitudinal component by Ψ_1 ; hence, the velocity field can be expressed in the form

$$u = \Psi_1(\zeta, \lambda_m)U(s, n), \quad (3.63a)$$

$$v = \nu [\Gamma_0(\zeta, \lambda_m) \exp(i\lambda_m s) + c.c.] U(s, n)D(s, n) + \Gamma_1(\zeta, \lambda_m)V(s, n), \quad (3.63b)$$

where

$$\zeta = \frac{z - \eta}{D} \quad (3.64)$$

is a stretched vertical coordinate, (s, n) represents a curvilinear orthogonal system of coordinates where s denotes the arclength, U and V are depth-averaged longitudinal and transverse velocity components and D is water depth. Furthermore, the local radius of curvature, scaled by half-width b_0^* , is given by

$$\frac{1}{r(s)} = \nu \exp(i\lambda_m s) + c.c. \quad (3.65)$$

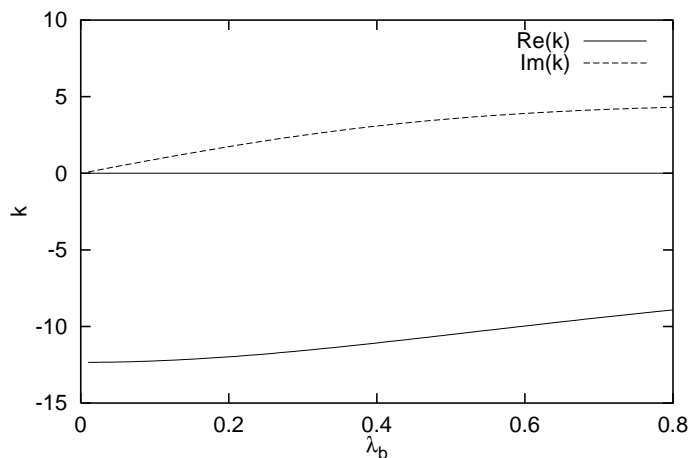


Figure 3.19: Real and imaginary part of k versus λ_b ($\beta = 15$, $\vartheta_0 = 0.1$, $d_s = 0.01$).

and *c.c.* denotes complex conjugate. In order to keep the leading dispersive effects which are associated with the transverse velocity component with zero depth-average, the vertical structure of Γ_0 is fully derived by the three-dimensional solution. Moreover, neglecting longitudinal convection, the latter solution shows that both Γ_1 and Ψ_1 coincide with the logarithmic velocity distribution $u_0(\zeta)$. Thus equations (3.63a,b) can be written in the form

$$u = u_0(\zeta)U, \quad (3.66a)$$

$$v = \nu [\Gamma_0(\zeta, \lambda_m) \exp(i\lambda_m s) + c.c.] UD + u_0(\zeta)V. \quad (3.66b)$$

The above structure strictly applies within the context of a linear theory and in the limit $\lambda_m \rightarrow 0$. However the analysis is not largely affected by the latter assumption since longitudinal convection is neglected only in the estimate of dispersive effects associated with Γ_1 and Ψ_1 distributions but is fully accounted for in the depth-averaged model. It is also kept in the evaluation of Γ_0 as it is appropriate to describe the lag required for secondary flow to adapt to local curvature.

Equations (3.66a,b) imply a similar decomposition for bed stresses in the the form

$$(\tau_s, \tau_n) = \{U, V + \nu UD [k \exp(i\lambda_m s) + c.c.]\} C_f (U^2 + V^2)^{1/2}, \quad (3.67)$$

where a further contribution to transverse bottom stress associated with the helical component of secondary flow has been included through the parameter

k which reads

$$k = \left(\frac{\Gamma_{0,\zeta}}{u_{0,\zeta}} \right)_{\zeta_0}. \quad (3.68)$$

In figure 3.19 the real and imaginary parts of k are plotted versus curvature wave number.

Notice that even though in the present study k has been directly obtained from the 3D model, some formulas exist which allow to compute k without solving the 3D problem (Olesen (1987)).

The results can be extended to the case of channels subject to width variations, taking into account streamlines curvature, given by (3.62).

At the linear level equation (3.67) implies a correction to the transverse component of bottom stress which reads

$$\tau_y = \tau'_y + \tau''_y = C_{f0} V_1 \left(1 - k \frac{i\lambda_b}{\beta} \right). \quad (3.69)$$

In system (3.20a-d) all the coefficients remain unchanged except for a_4 and a_7 which take the following expressions

$$a_4 = i\lambda_b + \beta C_{f0} \left(1 + \frac{i\lambda_b k}{\beta} \right), \quad a_8 = 1 + \frac{i\lambda_b k}{\beta}. \quad (3.70a,b)$$

In figures 3.20, 3.21 and 3.22 the amplitude and phase of harmonic 1 of the Fourier representation of bed topography as predicted by the 3D and the corrected 2D models are plotted. It appears that the results are fairly close: with the inclusion of the effect of streamlines curvature the two-dimensional model is able to describe transverse deformations of bed profile and flow characteristics. Furthermore the dependence of the phase shift and the amplitude of flow and bed variables on wave number of width variations is similar to that predicted by the three-dimensional model. Notice that both models predict a resonant response for almost the same values of the parameters (figures 3.20e, 3.21e and 3.22e). Figure 3.23 shows a comparison between the transverse bed profiles predicted by the models for different values of the longitudinal coordinate x and for different wave numbers of width variations.

It also appears that, even though including streamlines curvature effect increases the agreement between 2D and 3D models, this is not the only three-dimensional effect responsible for transverse variations of flow field and bed topography. In particular the amplitude of harmonic 1 of longitudinal velocity component displays a rather different dependence on λ_b in the two models (figure 3.21a,c,e). The above findings suggest that the longitudinal velocity is also influenced by secondary flow associated with convective terms as described in the previous section.

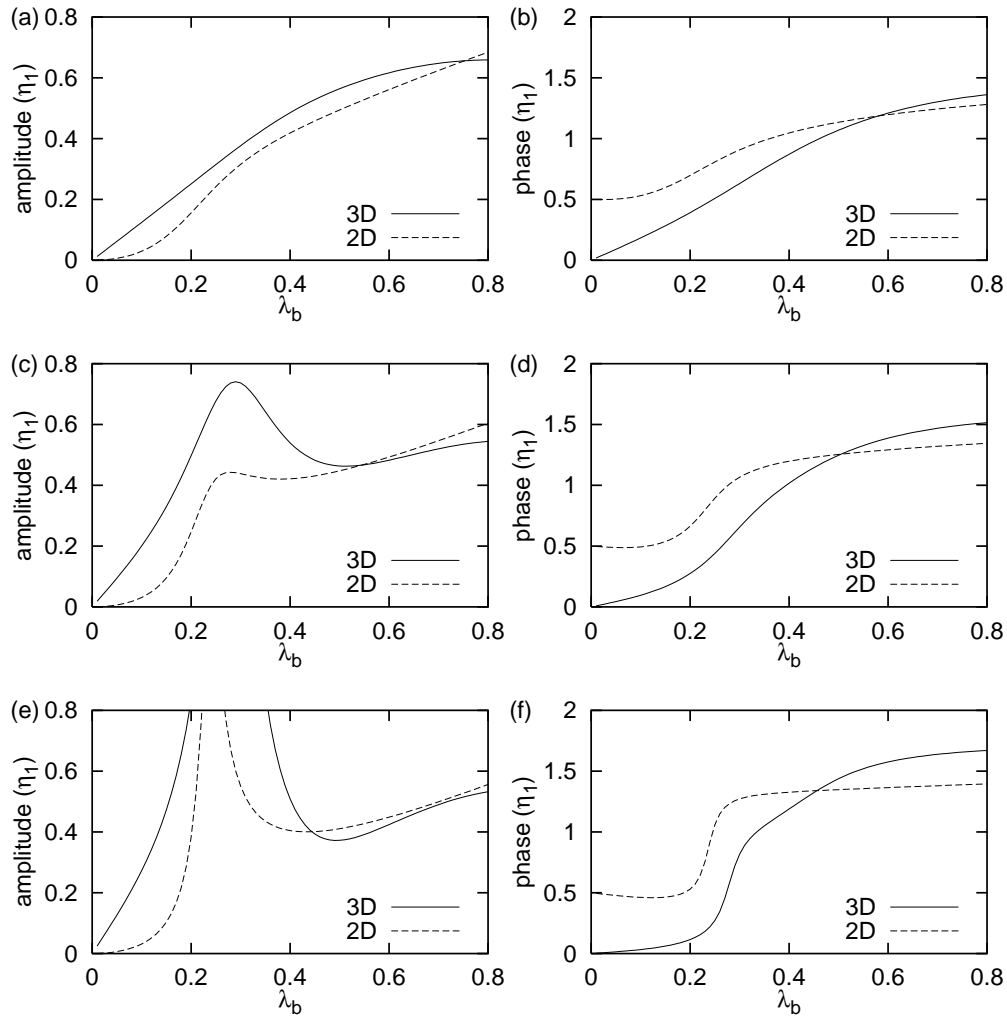


Figure 3.20: Amplitude ((a), (c), (e)) and phase ((b), (d), (f)) of harmonic 1 of bed profile versus λ_b , for different values of β . (a), (b) $\beta = 10$; (c), (d) $\beta = 15$; (e), (f) $\beta = 20$ ($\vartheta_0 = 0.1$, $d_s = 0.05$, $\beta = 10$).

3.6 Planimetric evolution

We now investigate the conditions under which the perturbed flow induced by width variations is able to produce a positive erosion rate in the widest section, which implies that the flow tends to enhance the given initial perturbation of channel width. It will appear that these conditions, which are taken as implying the incipient bifurcation of the flow, are strictly connected with the role of the transverse deformations of flow and bottom topography

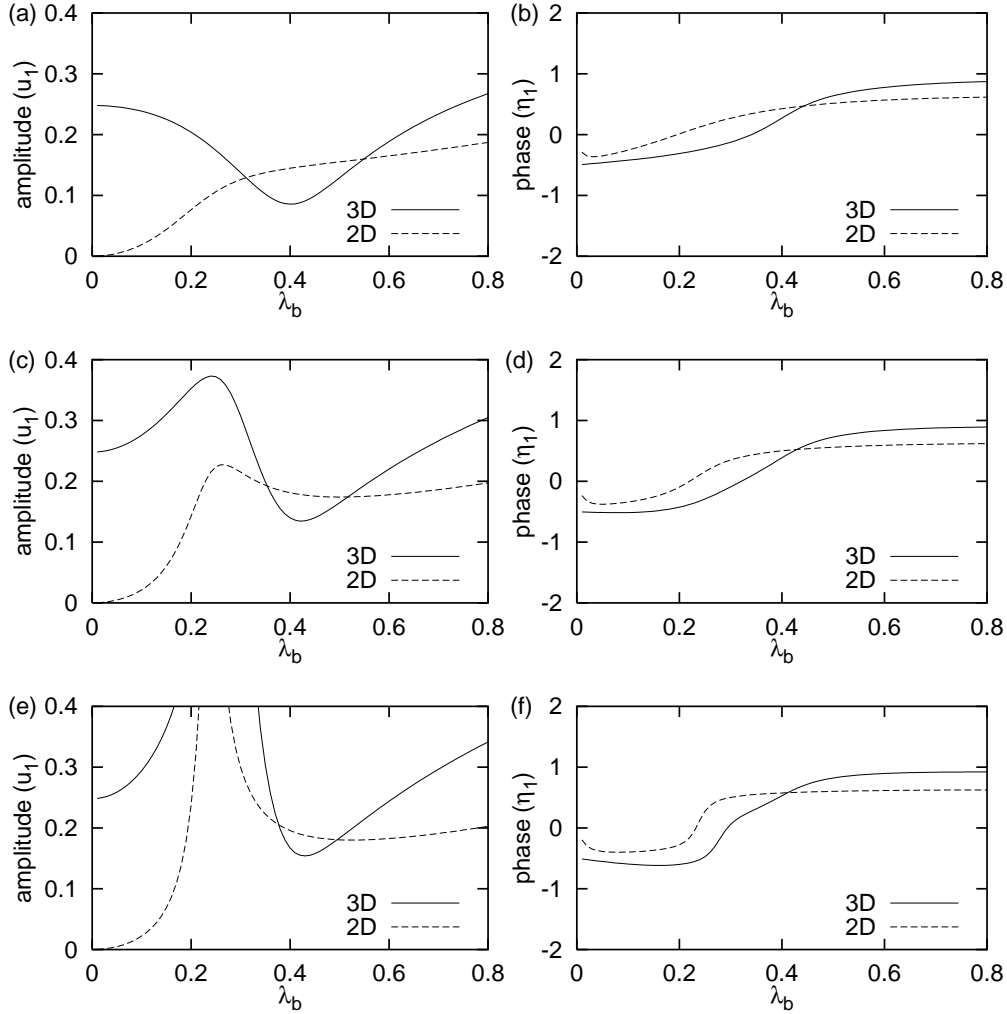


Figure 3.21: Amplitude ((a), (c), (e)) and phase ((b), (d), (f)) of harmonic 1 of longitudinal velocity component versus λ_b , for different values of β . (a), (b) $\beta = 10$; (c), (d) $\beta = 15$; (e), (f) $\beta = 20$ ($\vartheta_0 = 0.1$, $d_s = 0.05$, $\beta = 10$).

associated with 3D effects.

As pointed out in the introduction of the present chapter bank stability is investigated through a simplified model, whereby the net channel widening is neglected and the rate of bank retreat is related to the excess of depth averaged velocity at the banks U_b with respect to the uniform flow velocity, in the form

$$\frac{dy_s}{dt} = EU_b e^{i\lambda_b x} + c.c., \quad (3.71)$$

where y_s is bank profile and E is a suitable erosion coefficient.

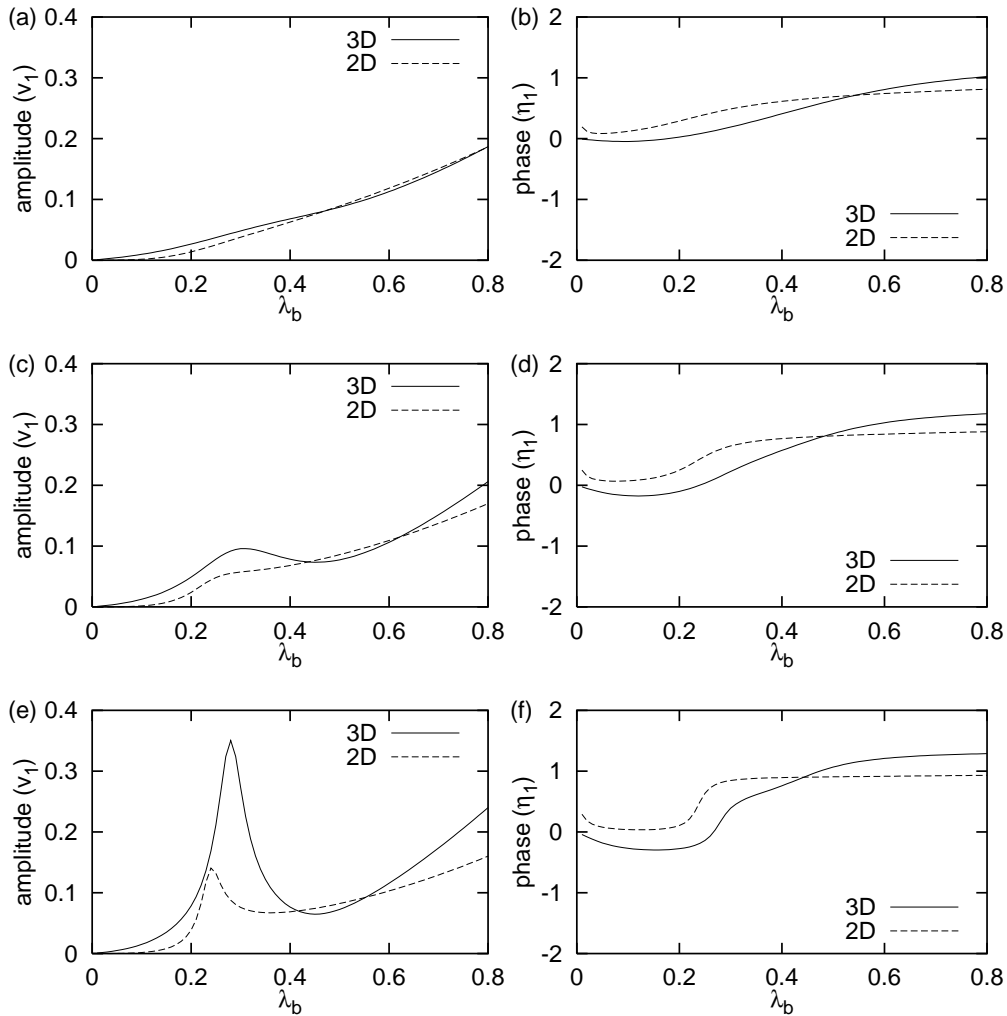


Figure 3.22: Amplitude ((a), (c), (e)) and phase ((b), (d), (f)) of harmonic 1 of transverse velocity component versus λ_b , for different values of β . (a), (b) $\beta = 10$; (c), (d) $\beta = 15$; (e), (f) $\beta = 20$ ($\vartheta_0 = 0.1$, $d_s = 0.05$, $\beta = 10$).

In figure 3.24 the phase α_u of the longitudinal depth-average velocity, that is the location of its maximum longitudinal value with respect to bank profile, is plotted versus the wavenumber of width variations. In the same figure results of the 2D model are also reported. In the latter case longitudinal velocity attains its maximum value at the narrowest section both at the centerline and at the banks ($\alpha_u/\pi \sim 1$): this implies that the channel is planimetrically stable since bank erosion tends to widen the channel where the channel is narrow. The figure shows that the results of present 3D model

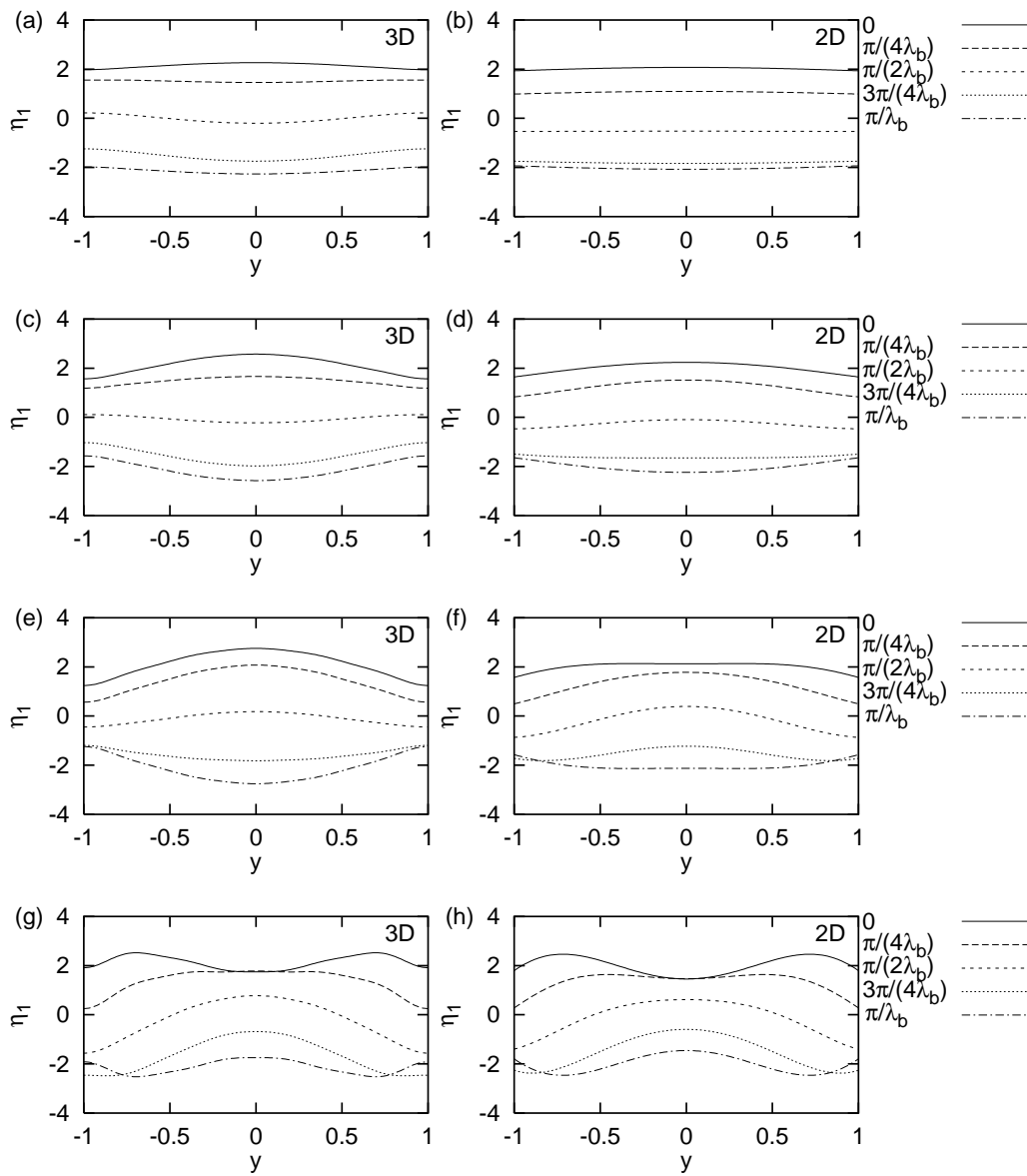


Figure 3.23: Transverse bottom profile for different values of the longitudinal coordinate. (a), (b) $\lambda_b = 0.1$; (c), (d) $\lambda_b = 0.2$; (e), (f) $\lambda_b = 0.3$; (g), (h) $\lambda_b = 0.5$ ($\vartheta_0 = 0.1$, $d_s = 0.05$, $\beta = 10$).

lead to a different scenario: while at the centerline we obtain a similar behavior, the opposite situation occurs at the banks where, for a wide range of values of λ_b , the maximum of longitudinal velocity, that is of erosion rate, is located at the wide sections ($\alpha_u/\pi > 1.5$). Under these conditions the chan-

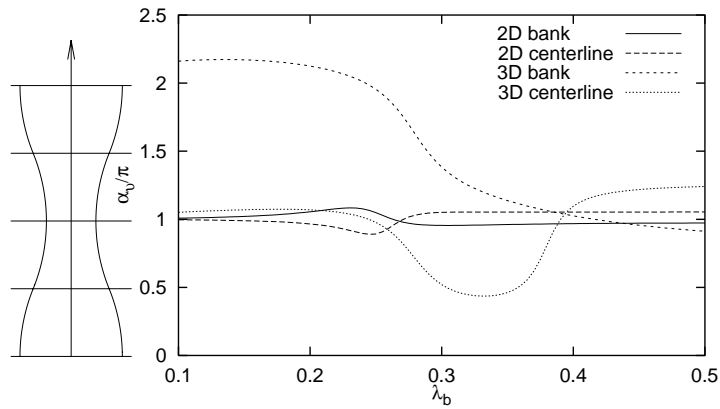


Figure 3.24: The phase α_u of longitudinal depth-average velocity at the centerline (dotted lines) and at the banks (continuous lines) is plotted versus the wavenumber of width variations (thinner lines: 2D model; ticker lines: 3D model) ($\beta = 20$, $\vartheta_0 = 0.1$, $d_s = 0.05$)

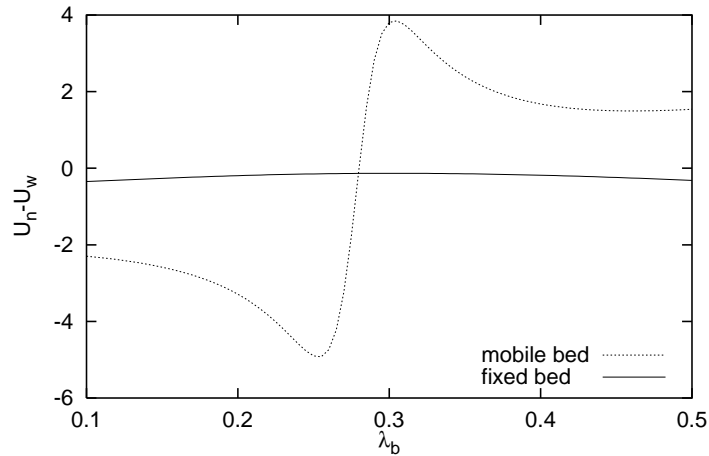


Figure 3.25: The difference between the bank values of the depth averaged longitudinal velocity at the narrowest and widest section is plotted versus the wavenumber of width variations ($\beta = 20$, $\vartheta_0 = 0.1$, $d_s = 0.05$).

nel is planimetrically unstable since flow and bottom perturbations tend to enhance the initial amplitude of width variations.

Figure 3.25 shows the results for the depth averaged velocity at the banks obtained both in case of mobile bed and fixed bed. The results are given in terms of the difference ($U_n - U_w$) between the values in the narrowest and widest section, respectively. It appears that the planimetric instability is

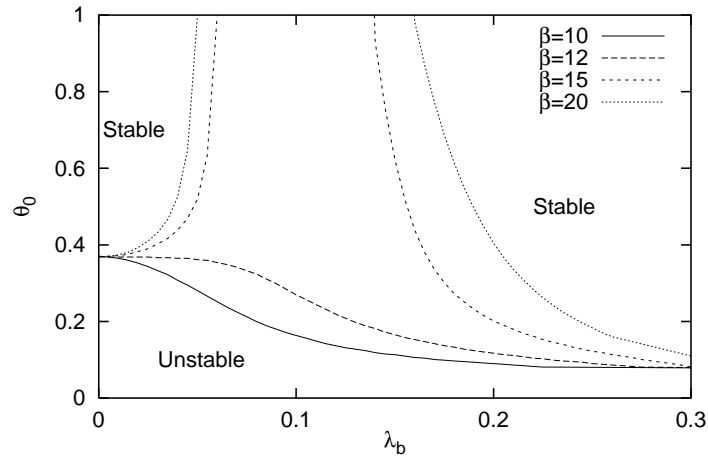


Figure 3.26: Neutral stability curves in the plane (λ_b, ϑ_0) ($\beta_0 = 15$, $d_s = 0.05$).

enhanced by the flow divergence associated with bed deformation, which leads to the formation of a central bar in the wider part of the channel. However, even in the case of fixed bed, $(U_n - U_w)$ is negative, which implies that three dimensional effects are able to counteract the overall decrease of cross sectionally averaged velocity which occurs in the widest section.

Figure 3.25 also suggests that in case of movable bed the solution is strongly dependent on the wavenumber of width variations: at large values of λ_b the central bar is shifted downstream with respect to the widest section so that topographic effects are no longer destabilizing.

Theoretical results are summarized in figure 3.26 where marginal stability curves are reported in the plane (λ_b, ϑ_0) for different values of the width ratio β . Three distinct regions can be identified. At low values of ϑ_0 the channel is always unstable. When ϑ_0 increases a threshold value of λ_b exists above which the channel is stable; at large values of ϑ_0 the channel is unstable for all wave numbers of width variations. For suitable values of β a quasi resonant behavior is exhibited by the solution: in this case the planform is unstable provided the wavenumber λ_b fall within a convenient range.

Chapter 4

Suppression of free bars in channels with variable width

4.1 Introduction

In the present chapter we investigate the effect of periodic width variations on the development process of free bars in straight cohesionless channels.

Kinoshita & Miwa (1974) showed experimentally that channel curvature induces a damping effect on alternate bar formation and migration; in particular they observed that, provided channel sinuosity exceed a certain threshold value, depending on hydraulic conditions, migrating alternate bars do not develop in the channel. The process has also been interpreted theoretically by Tubino & Seminara (1990) with reference to a regular sequence of small-amplitude meanders.

The aim of the present chapter is to ascertain whether a similar suppressive mechanism on migrating alternate bars is exerted by periodic variations of channel width. The approach adopted herein presents several analogies with respect to the case of meandering channels. In both cases it is required an investigation of the non linear interactions between free responses which would naturally develop (alternate bars) and forced responses (due to channel curvature or width variations). In the present case, in order to determine the forced response we take advantage of the assumption of small amplitude of width variations. It is worth pointing out that unlike in the case of meandering channels, here the forced bed response displays a spatial structure which differs from that of alternate free bars, due to the symmetric character of the forcing effect exerted by channel banks.

Some preliminary results of this work are reported in Repetto & Tubino (1999)b.

4.2 Formulation of the problem

We tackle the problem within a context of a two dimensional model, hence we refer to the mathematical formulation presented in section 3.2.1.

The adoption of a depth averaged model may turn out to be a rather crude approximation in the light of results presented in section 3.3.4, which suggest that three dimensional effects influence significantly the flow and bed structure in channels with variable width. However, a two dimensional model is amenable to an analytical solution which requires a comparatively small effort with respect to the three dimensional solution. Also notice that the effect of secondary flows due to local curvature of streamlines on transverse bed shear stress can be taken into account as described in section 3.5.

4.3 Solution

4.3.1 Outline of the solution procedure

We develop a linear stability theory for free bars formation in a channel with sinusoidal width variations of small amplitude. It will appear that our solution will lead to determine a linear correction to the growth rate of free bars as predicted in the case of constant width channel (Colombini et al. (1987)).

The first step of the analysis is to study the forced problem driven by width variations. The assumption of small-amplitude of width variations, which is mathematically expressed by (3.1b), suggests to expand the solution in terms of parameter δ as follows

$$\begin{aligned} (U, V, H, D) = & (1, 0, \overline{H}, 1) + \delta [e_1 (U_1, V_1, H_1, D_1) + c.c.] + \\ & + \delta^2 \{ [e_2 (U_2, V_2, H_2, D_2) + c.c.] + (U_0, V_0, H_0, D_0) \} + \mathcal{O}(\delta^3), \end{aligned} \quad (4.1)$$

where

$$e_1 = \exp(i\lambda_b x), \quad e_2 = \exp(2i\lambda_b x). \quad (4.2a,b)$$

Substituting from (4.1) into the governing differential equations (3.9a-d) and in the boundary conditions (3.11a-d), leads to a sequence of ordinary differential problems in terms of the transverse coordinate y . In particular, at order $\mathcal{O}(\delta)$ we find the linear forced solution described in section 3.2 which leads to the following structure of variables

$$V_1 = \gamma_1 \sinh(\lambda_1 y) + \gamma_2 \sinh(\lambda_2 y), \quad (4.3a)$$

$$U_1 = \phi_1 \cosh(\lambda_1 y) + \phi_2 \cosh(\lambda_2 y), \quad (4.3b)$$

$$H_1 = \theta_1 \cosh(\lambda_1 y) + \theta_2 \cosh(\lambda_2 y), \quad (4.3c)$$

$$D_1 = \delta_1 \cosh(\lambda_1 y) + \delta_2 \cosh(\lambda_2 y). \quad (4.3d)$$

The $\mathcal{O}(\delta^2)$ terms arise from nonlinear interactions of the linear forced solution and consist of a second harmonic in the longitudinal direction (U_2, V_2, H_2, D_2) and a distortion of the basic uniform flow (U_0, V_0, H_0, D_0).

We now investigate the conditions required for the basic flow (4.1) to loose stability with respect to infinitesimal perturbations periodic in the longitudinal direction. The structure of the solution (say for the longitudinal velocity) can be written in terms of a two parameters expansion in the form

$$\begin{aligned} U = & 1 + \delta [e_1 U_1(y) + c.c.] + \delta^2 [(e_2 U_2(y) + c.c.) + U_0(y)] + \mathcal{O}(\delta^3) + \\ & + A(t) [E_1 u_1(y) + c.c.] + A(t) \delta [E_1 e_1 U'_{11}(y) + \bar{E}_1 e_1 U''_{11}(y) + c.c.] + \\ & + A(t) \delta^2 [E_1 U_{01}(y) + c.c.] + \mathcal{O}(A^2, A\delta^2), \end{aligned} \quad (4.4)$$

with $A(t)$ infinitesimal amplitude of bars and

$$E_1 = \exp [i(\lambda x - \omega_0 t)], \quad (4.5)$$

where λ and ω_0 are the dimensionless wavenumber and angular frequency of free bars. Overlines denote the complex conjugates.

At $\mathcal{O}(A)$ we recover the linear homogeneous problem for free bars stability in channels with constant width. If we neglect higher order terms, according with the solution of Colombini et al. (1987) we obtain

$$A = \hat{A} \exp(\Omega_0 t). \quad (4.6)$$

Solvability of linear problem leads to a dispersion relationship for the growth rate Ω_0 and the angular frequency ω_0 of free bars in channels with constant width in the form

$$(\Omega_0, \omega_0) = f(\lambda, \beta, \vartheta_0, d_s), \quad (4.7)$$

where ϑ_0 is Shields parameter of the reference uniform flow.

The structure of the expansion (4.4) suggests that non linear interactions involving the fundamental $\mathcal{O}(A)$ alternate bar mode and the $\mathcal{O}(\delta)$ forced mode lead to mixed modes. At order $\mathcal{O}(A\delta^2)$ the fundamental free mode is reproduced by the interactions of the mixed $\mathcal{O}(A\delta)$ mode with the linear

forced mode and of the $\mathcal{O}(\delta^2)$ distortion of the basic flow with the linear free mode. This implies the appearance of $\mathcal{O}(\delta^2)$ terms in the linear problem for free bars. Hence, solvability is accomplished provided the growth rate Ω and angular frequency ω of free bars are given in the form

$$(\Omega - i\omega) = (\Omega_0 - i\omega_0) + \delta^2 (\Omega_1 - i\omega_1), \quad (4.8)$$

where Ω_1 and ω_1 depend also on the wavenumber λ_b of width variations.

4.3.2 First order free problem - $\mathcal{O}(A)$

We recall in this section the linear solution of Colombini et al. (1987) for free bars formation in straight channels with constant width. We study the stability of the uniform flow in the channel with respect to small perturbations of the bed. The problem is mathematically described by 2D de Saint Venant flow equations, continuity equation and sediment continuity equation. We assume the time scale of bottom deformation to be much smaller than the time scale of flow field variations; hence, we neglect time derivatives in flow field equations. In other words we assume the flow to be, at each time, in equilibrium with the instantaneous bed configuration. The governing differential equations read

$$UU_{,x} + VU_{,y} + H_{,x} + \frac{\beta\tau_x}{D} = 0, \quad (4.9a)$$

$$UV_{,x} + VV_{,y} + H_{,y} + \frac{\beta\tau_y}{D} = 0, \quad (4.9b)$$

$$(UD)_{,x} + (VD)_{,y} = 0, \quad (4.9c)$$

$$(F_0^2 H - D)_{,t} + Q_0(q_{x,x} + q_{y,y}) = 0, \quad (4.9d)$$

where

$$Q_0 = \frac{d_s^* \left(\frac{\rho_s - \rho}{\rho} g d_s^* \right)^{1/2}}{(1-p)D_0^* U_0^*}. \quad (4.10)$$

The boundary conditions impose vanishing of water and sediment flux at the side walls; they read

$$V = 0, \quad (y = \pm 1), \quad (4.11a)$$

$$q_y = 0, \quad (y = \pm 1). \quad (4.11b)$$

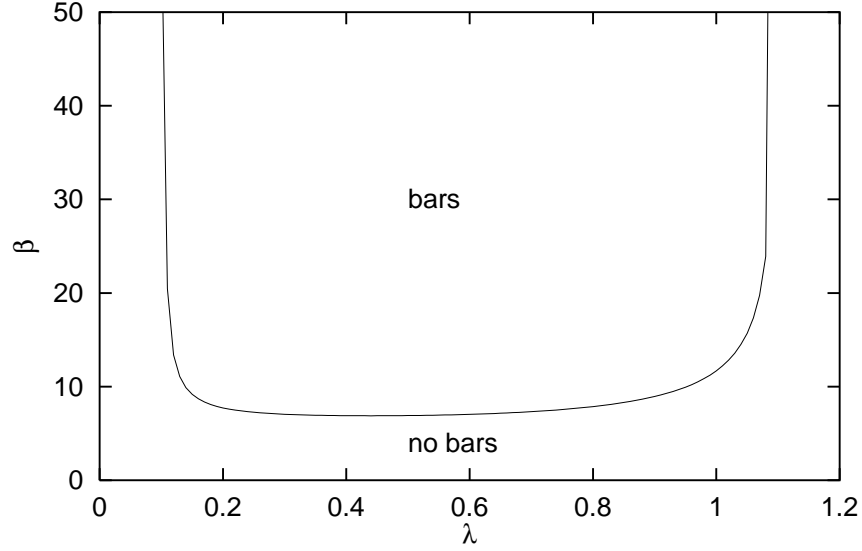


Figure 4.1: Neutral stability curve for bars formation.

We expand the solution in terms of the small amplitude of bed perturbations $A(t)$ in the form

$$(U, V, H, D) = (1, 0, \overline{H}, 1) + A(t)E_1[u_1(y), v_1(y), h_1(y), d_1(y)] + c.c.. \quad (4.12)$$

The infinitesimal amplitude A is found to grow in time according to the following relationship

$$A = \hat{A} \exp(\Omega_0 t), \quad (4.13)$$

where Ω_0 is the growth rate of bars.

Substituting (4.12) into equations (4.9a-d) and (4.11a,b) we find the following homogeneous differential system

$$\mathbf{\Gamma} \cdot \begin{pmatrix} u_1 \\ v_1 \\ h_1 \\ d_1 \end{pmatrix} = \begin{pmatrix} 0 \\ 0 \\ 0 \\ 0 \end{pmatrix}, \quad (4.14)$$

where

$$\Gamma_{11} = i\lambda + 2\beta C_{f0},$$

$$\Gamma_{12} = \Gamma_{21} = \Gamma_{24} = \Gamma_{33} = 0,$$

$$\begin{aligned}
\Gamma_{13} = \Gamma_{31} = \Gamma_{34} &= i\lambda, & \Gamma_{14} &= \beta C_{f0}(C_D - 1), \\
\Gamma_{22} &= i\lambda + \beta C_{f0}, & \Gamma_{23} = \Gamma_{32} &= \frac{d}{dy}, \\
\Gamma_{41} &= 2Q_0\Phi_0 i\lambda\Phi_T, & \Gamma_{42} &= Q_0\Phi_0 \frac{d}{dy}, \\
\Gamma_{43} &= F_0^2 \left(-Q_0\Phi_0 R \frac{d^2}{dy^2} + \Omega_0 - i\omega_0 \right), \\
\Gamma_{44} &= Q_0\Phi_0 \left(R \frac{d^2}{dy^2} + i\lambda C_D \Phi_T \right) - \Omega_0 + i\omega_0
\end{aligned} \tag{4.15}$$

and all the coefficients have been defined in section 3.2.

To find a non trivial solution of system (4.14) a solvability condition is required, which leads to determine the dispersion relation and allows one to calculate the growth rate Ω_0 and migration speed ω_0 of free bars in the form

$$(\Omega_0, \omega_0) = f(\lambda, \beta, \vartheta_0, d_s), \tag{4.16}$$

The analysis performed by Colombini et al. (1987) suggests that the crucial parameter to predict bar formation is the width to depth ratio β : when β exceeds a threshold value, which is dependent on Shields parameter and grain roughness parameter, free bars develop. Figure 4.1 shows a neutral stability curve in the plane (λ, β) for given values of ϑ_0 and d_s .

4.3.3 First order forced problem - $\mathcal{O}(\delta)$

The first order forced problem, which has been already considered in section 3.2, can be written in the form

$$\mathbf{L}_1 \cdot \begin{pmatrix} U_1 \\ V_1 \\ H_1 \\ D_1 \end{pmatrix} = \begin{pmatrix} b_1^{(1)} \\ b_2^{(1)} \\ b_3^{(1)} \\ b_4^{(1)} \end{pmatrix}, \tag{4.17}$$

with the boundary conditions

$$V_1 = \pm i\lambda_b, \quad (y = \pm 1), \tag{4.18a}$$

$$(F_0^2 H_1 - D_1)_{,y} = 0, \quad (y = \pm 1), \quad (4.18b)$$

where

$$\mathbf{L}_1 = \begin{pmatrix} i\lambda_b + 2\beta C_{f0} & 0 & i\lambda_b & \beta C_{f0}(C_D - 1) \\ 0 & i\lambda_b + \beta C_{f0} & \frac{d}{dy} & 0 \\ i\lambda_b & \frac{d}{dy} & 0 & i\lambda_b \\ 2i\lambda_b \Phi_T & \frac{d}{dy} & -F_0^2 R \frac{d^2}{dy^2} & R \frac{d^2}{dy^2} + i\lambda_b C_D \Phi_T \end{pmatrix}, \quad (4.19)$$

where all the coefficients have been defined in section 3.2 and

$$b_1^{(1)} = b_2^{(1)} = b_3^{(1)} = b_4^{(1)} = 0. \quad (4.20a-c)$$

4.3.4 Scheme of the solution at the higher orders

Proceeding to the higher orders of approximation the structure of the solution is given by the interaction between the first order solutions $\mathcal{O}(A)$ and $\mathcal{O}(\delta)$ which have the following form (for instance for the perturbation of the longitudinal velocity component)

$$A \exp(i\lambda x) \sin\left(\frac{\pi}{2}y\right) + \bar{A} \exp(-i\lambda x) \sin\left(\frac{\pi}{2}y\right), \quad (4.21a)$$

$$\delta \exp(i\lambda_b x) \cosh(\alpha y) + \bar{\delta} \exp(-i\lambda_b x) \cosh(\bar{\alpha} y), \quad (4.21b)$$

where we are considering the alternate bar mode and the overline indicates the complex conjugate problem.

The structure of the solution at order $\mathcal{O}(\delta^2)$ and order $\mathcal{O}(A\delta)$ read

Order δ^2

$$\delta\delta \exp(2i\lambda_b x) \cosh^2(\alpha y) + c.c., \quad (4.22a)$$

$$\delta\bar{\delta} \cosh(\alpha y) \cosh(\bar{\alpha} y) + c.c.. \quad (4.22b)$$

Order $A\delta$

$$A\delta \exp[i(\lambda + \lambda_b)x] \sin\left(\frac{\pi}{2}y\right) \cosh(\alpha y) + c.c., \quad (4.23a)$$

$$A\bar{\delta} \exp [i(\lambda - \lambda_b)x] \sin \left(\frac{\pi}{2}y \right) \cosh(\bar{\alpha}y) + c.c.. \quad (4.23b)$$

At order $\mathcal{O}(A\delta^2)$ non linear interactions lead to the following structure of the solution

$$A(\delta\delta) \exp [i(\lambda + 2\lambda_b)x] \sin \left(\frac{\pi}{2}y \right) \cosh^2(\alpha y) + c.c., \quad (4.24a)$$

$$A(\bar{\delta}\bar{\delta}) \exp [i(\lambda - 2\lambda_b)x] \sin \left(\frac{\pi}{2}y \right) \cosh^2(\bar{\alpha}y) + c.c., \quad (4.24b)$$

$$\rightarrow A(\bar{\delta}\delta) \exp (i\lambda x) \sin \left(\frac{\pi}{2}y \right) \cosh(\alpha y) \cosh(\bar{\alpha}y) + c.c., \quad (4.24c)$$

$$\delta(A\delta) \exp [i(\lambda + 2\lambda_b)x] \sin \left(\frac{\pi}{2}y \right) \cosh^2(\alpha y) + c.c., \quad (4.24d)$$

$$\rightarrow \delta(A\bar{\delta}) \exp (i\lambda x) \sin \left(\frac{\pi}{2}y \right) \cosh(\alpha y) \cosh(\bar{\alpha}y) + c.c., \quad (4.24e)$$

$$\delta(\bar{A}\delta) \exp [i(-\lambda + 2\lambda_b)x] \sin \left(\frac{\pi}{2}y \right) \cosh^2(\alpha y) + c.c., \quad (4.24f)$$

$$\rightarrow \delta(\bar{A}\bar{\delta}) \exp (-i\lambda x) \sin \left(\frac{\pi}{2}y \right) \cosh(\alpha y) \cosh(\bar{\alpha}y) + c.c.. \quad (4.24g)$$

Notice that some interactions, namely those indicated by an arrow, reproduce the structure of the fundamental $\mathcal{O}(A)$ solution: at this level a solvability condition for the system is required as discussed in the following. Since we are studying the effect of width variations on free bars formation, we only need to solve those problems which lead to the fundamental structure reproduction.

The reproduction of the fundamental solution is obtained, at the third order, also by self interactions involving free modes only, as discussed by Colombini et al. (1987) ($A(\bar{A}A) + c.c.$ and $\bar{A}(AA) + c.c.$). However, in the context of a linear stability analysis, this contribution is negligible since we are assuming A to be much smaller with respect to the amplitude δ of width variations: this implies $\mathcal{O}(A^3) \ll (A\delta^2)$.

4.3.5 $\mathcal{O}(\delta^2)$ problem

The differential system governing the distortion of the basic flow is obtained as the solution of the following system

$$\mathbf{L}_0 \cdot \begin{pmatrix} U_0 \\ V_0 \\ H_0 \\ D_0 \end{pmatrix} = \begin{pmatrix} b_1^{(0)} \\ b_2^{(0)} \\ b_3^{(0)} \\ b_4^{(0)} \end{pmatrix}, \quad (4.25)$$

with the boundary conditions

$$V_0 = \pm i\lambda_b \bar{U}_1 + c.c., \quad (y = \pm 1), \quad (4.26a)$$

$$R(F_0^2 H_0 - D_0)_{,y} = Q_{y0} \pm i\lambda_b (\bar{U}_1 - \bar{Q}_{x1}) + c.c., \quad (y = \pm 1), \quad (4.26b)$$

where \mathbf{L}_0 is a linear differential operator obtained from \mathbf{L}_1 by replacing λ_b with 0; the coefficients $b_j^{(0)}$ arise from non linear interactions and read

$$\begin{aligned} b_1^{(0)} = & - [i\lambda_b(U_1 + H_1) - \beta C_{f0} D_1 + \beta T_{x1} + U_{1,y} \bar{V}_1 + \\ & - \beta T_{x1} \bar{D}_1 + \beta C_{f0} D_1 \bar{D}_1 - iy\lambda_b(\bar{U}_{1,y} + \bar{H}_{1,y}) + \beta T_{x0}] + c.c., \end{aligned} \quad (4.27a)$$

$$\begin{aligned} b_2^{(0)} = & - [i\lambda_b(V_1 + V_1 \bar{U}_1) + V_1 \bar{V}_{1,y} - \beta T_{y1} \bar{D}_1 + \\ & + \beta T_{y1} - i\lambda_b y \bar{V}_{1,y} + \beta T_{y0}] + c.c., \end{aligned} \quad (4.27b)$$

$$\begin{aligned} b_3^{(0)} = & - [i\lambda_b(U_1 + D_1) + V_{1,y} \bar{D}_1 + D_{1,y} \bar{V}_1 + \\ & - i\lambda_b y (\bar{U}_{1,y} + \bar{D}_{1,y})] + c.c., \end{aligned} \quad (4.27c)$$

$$b_4^{(0)} = -Q_0 [i\lambda_b Q_{x0} + Q_{y0,y} - i\lambda_b y Q_{x1,y}] + c.c., \quad (4.27d)$$

where

$$T_{x1} = C_{f0}(2U_1 + C_D D_1), \quad (4.28a)$$

$$T_{y1} = C_{f0} V_1, \quad (4.28b)$$

$$Q_{x1} = 2\Phi_0\Phi_T U_1 + C_D\Phi_0\Phi_T D_1 \quad (4.28c)$$

and the coefficients T_{x0} , T_{y0} , Q_{x0} and Q_{y0} are not reported for the sake of brevity.

Furthermore the condition (3.11d) has to be satisfied, it reads

$$\int_0^{\frac{2\pi}{L_b}} \int_{-1}^1 (F_0^2 H_0 - D_0) dy dx = 0. \quad (4.29)$$

4.3.6 $\mathcal{O}(A\delta)$ problem

At the order $\mathcal{O}(A\delta)$ mixed interactions give rise to $_{11}$ components satisfying the following differential system

$$\mathbf{L}'_{11} \cdot \begin{pmatrix} U'_{11} \\ V'_{11} \\ H'_{11} \\ D'_{11} \end{pmatrix} = \begin{pmatrix} b_1^{(11)'} \\ b_2^{(11)'} \\ b_3^{(11)'} \\ b_4^{(11)'} \end{pmatrix}, \quad (4.30)$$

with the boundary conditions

$$V'_{11} = \pm i\lambda_b u_1, \quad (y = \pm 1), \quad (4.31a)$$

$$R(F_0^2 H'_{11} - D'_{11})_{,y} = Q'_{y11} \pm i\lambda_b (u_1 - q_{x1}), \quad (y = \pm 1), \quad (4.31b)$$

The coefficients $b_j^{(11)'}$ arise from non linear interactions and read

$$\begin{aligned} b_1^{(11)'} &= -[i(\lambda + \lambda_b)U_1 u_1 + i\lambda u + V_1 u_{1,y} + v_1 U_{1,y} + i\lambda h_1 + \beta t_{x1} + \\ &\quad -\beta C_{f0} d_1 - \beta t_{x1} D_1 - \beta T_{x1} d_1 + 2\beta C_{f0} d_1 D_1 + \\ &\quad + \beta T'_{x11} - i\lambda_b u_{1,y} - iy\lambda_b h_{1,y}], \end{aligned} \quad (4.32a)$$

$$\begin{aligned} b_2^{(11)'} &= -[i\lambda U_1 v_1 + i\lambda_b u_1 V_1 + i\lambda v_1 + v_1 V_{1,y} + V_1 v_{1,y} + \beta t_{y1} + \\ &\quad -\beta t_{y1} D_1 - \beta T_{y1} d_1 + \beta T'_{y11} - iy\lambda_b v_{1,y}], \end{aligned} \quad (4.32b)$$

$$b_3^{(11)'} = -[i(\lambda + \lambda_b)(d_1 U_1 + D_1 u_1) + i\lambda(d_1 + u_1) + v_1 D_{1,y} + V_1 d_{1,y} +$$

$$+V_{1,y}d_1 + v_{1,y}D_1 - iy\lambda_b(u_1 + d_1)_{,y}], \quad (4.32c)$$

$$b_4^{(11)'} = -Q_0 [i(\lambda + \lambda_b)Q'_{x11} + Q'_{y11,y} + -iy\lambda q_{x1,y}], \quad (4.32d)$$

where

$$t_{x1} = C_{f0}(2u_1 + C_D d_1), \quad (4.33a)$$

$$t_{y1} = C_{f0}v_1, \quad (4.33b)$$

$$q_{x1} = 2\Phi_0\Phi_T u_1 + C_D\Phi_0\Phi_T d_1 \quad (4.33c)$$

and the coefficients T'_{x11} , T'_{y11} , Q'_{x11} and Q'_{y11} are not reported for the sake of brevity.

The differential problem for " component appearing in expansion (4.4) is obtained from (4.30), (4.31a,b), (4.32a-d) and (4.33a-c) by replacing $i\lambda$ with $-i\lambda$ and the coefficients of the $\mathcal{O}(A)$ fundamental free mode (u_1, v_1, h_1, d_1) with their complex conjugate.

4.3.7 Solvability condition

At the order $\mathcal{O}(A\delta^2)$ the following differential system is found

$$\mathbf{L} \cdot \begin{pmatrix} U_{01} \\ V_{01} \\ H_{01} \\ D_{01} \end{pmatrix} = \begin{pmatrix} b_1^{(01)} \\ b_2^{(01)} \\ b_3^{(01)} \\ b_4^{(01)} - \Omega_1 + i\omega_1 \end{pmatrix}, \quad (4.34)$$

where \mathbf{L} is the linear operator governing the fundamental free mode and on the right side of the equation the corrections to bars growth rate and migration speed appear. The coefficients $b_1^{(01)}$, $b_2^{(01)}$, $b_3^{(01)}$ and $b_4^{(01)}$ are not reported. System (4.34) requires a solvability condition because its homogeneous part admits of a non trivial solution. The solvability condition allows one to determine the total growth rate and migration speed of bars corrected by the effect of width variations in the form

$$(\Omega - i\omega) = (\Omega_0 - i\omega_0) + \delta^2 (\Omega_1 - i\omega_1). \quad (4.35)$$

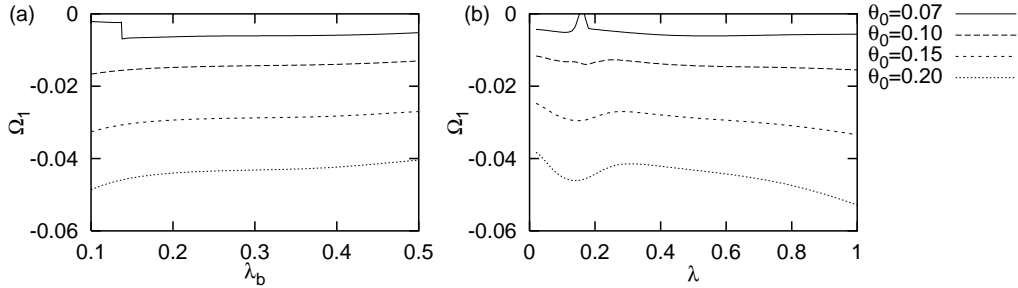


Figure 4.2: The correction Ω_1 to the growth rate of free bars is plotted versus λ_b (a) and λ (b) for different values of Shields parameter ϑ_0 ((a) $\lambda = 0.5$, (b) $\lambda_b = 0.3$, $\beta = 20$, $d_s = 0.01$).

4.4 Results

The main result of present analysis is the determination of the correction to the growth rate and migration speed of bars induced by periodic variations of channel width.

In figure 4.2a,b the correction Ω_1 to the growth rate is plotted versus the wavenumbers of width variations λ_b and of free bars λ , respectively, for different values of Shields parameter ϑ_0 . It appears that Ω_1 is always negative, which implies that the effect of width variations is invariably stabilizing. It also appears that the damping effect is slightly dependent on the wavenumber of width variations; furthermore it increases for increasing values of ϑ_0 . Notice that bar wavenumber of figure 4.2a roughly corresponds to that of the fastest growing bar in the constant width channel. Also notice that a resonant behavior analogous to that originally discovered by Blondeaux & Seminara (1985) in meandering channels is exhibited by our solution with $\vartheta_0 = 0.07$.

Equation (4.35) suggests that the damping effect on free bars is proportional to δ^2 , i.e. it increases as the amplitude of width variations increases. When the total growth rate vanishes free bars are suppressed: theoretical results suggest that this occurs for values of δ which are small enough to justify the small-amplitude assumption embodied in (4.1). Threshold values of δ for free bar suppression are given in figure 4.3 for different values of β and ϑ_0 . It appears that larger values of δ are required to suppress free bars when β is large. The latter finding is consistent with the fact that free bar instability is enhanced as we move away from the threshold value of width ratio β_c . This is also shown in figure 4.4a,b where the total growth rate of free bars is plotted versus λ for different values of λ_b and β , for given amplitude δ . When

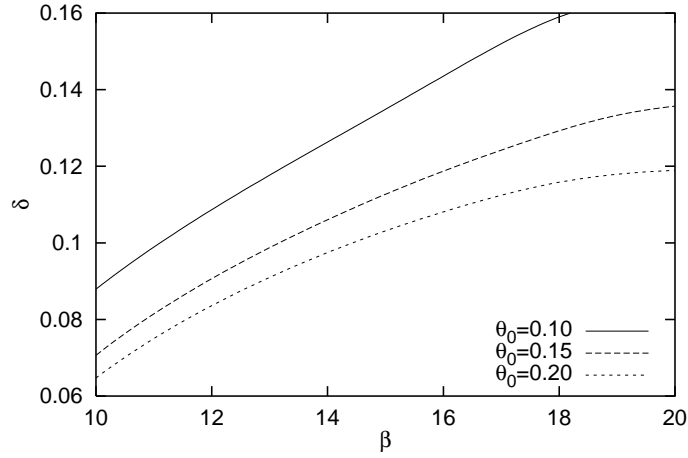


Figure 4.3: The threshold value of δ above which bars are suppressed is plotted versus β for different values of ϑ_0 ($d_s = 0.05$, $\lambda_b = 0.3$).

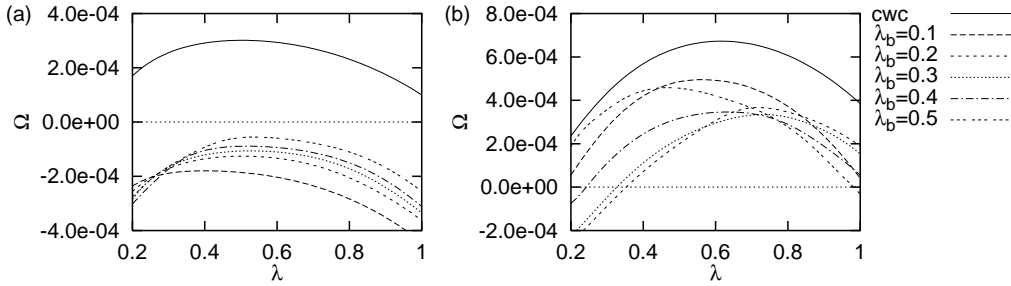


Figure 4.4: The growth rate Ω of free bars is plotted versus λ for different values of λ_b , (a) $\beta = 18$, (b) $\beta = 34$ (cwc: constant width channel. $\vartheta_0 = 0.2$, $d_s = 0.01$, $\delta = 0.125$).

β is small (figure 4.4a) free bars are suppressed; within the range of the most unstable bar perturbations the damping effect increases for increasing values of the wavelength of width variations. When β is large (figure 4.4b) width variations are unable to suppress free bars, however they significantly affect the selection process of the most unstable bar perturbation: for relatively slow variations (small λ_b) shorter bars are selected; as λ_b increases the most unstable range shifts towards smaller values of λ (longer bars).

Furthermore, figure 4.5a,b shows that the suppressive effect of width variations is more efficient at high values of Shields parameter (figure 4.5b).

Results for the migration speed of bars are reported in figures 4.6 and 4.7: it appears that width variations slow down the propagation of free bars; how-

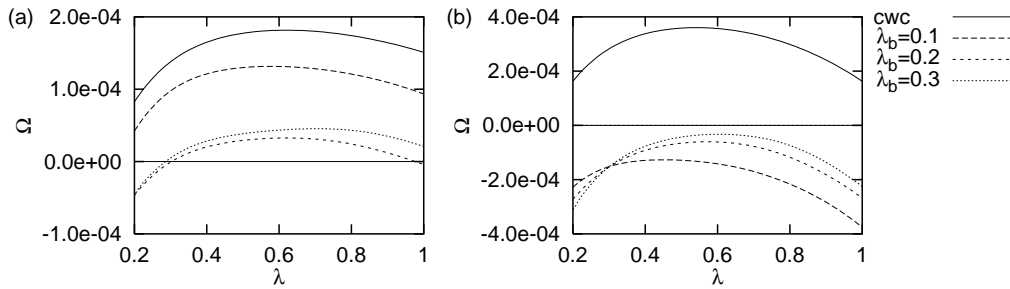


Figure 4.5: The growth rate Ω of free bars is plotted versus λ for different values of λ_b , (a) $\vartheta_0 = 0.1$, (b) $\vartheta_0 = 0.2$ (cwc: constant width channel. $\beta = 20$, $d_s = 0.01$, $\delta = 0.125$).

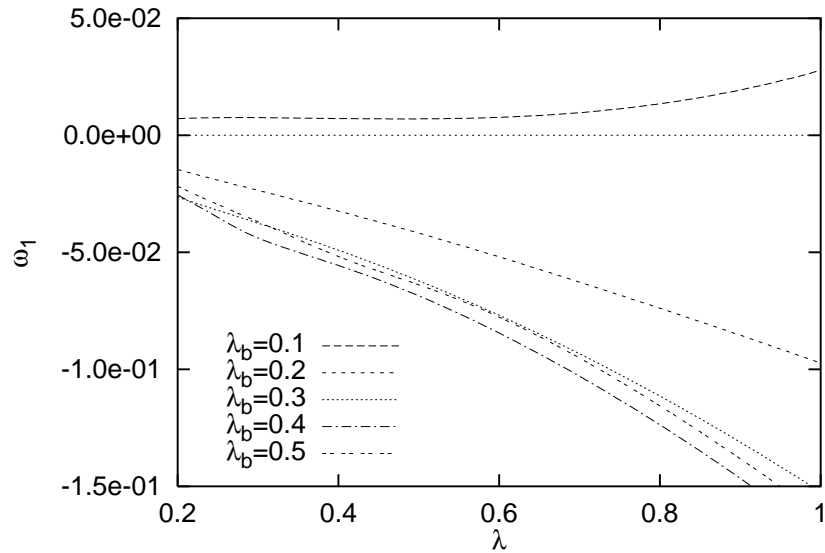


Figure 4.6: The correction ω_1 to total angular frequency ω of free bars is plotted versus λ for different values of λ_b ($\vartheta_0 = 0.2$, $d_s = 0.01$, $\beta = 18$, $\delta = 0.125$).

ever, at small values of λ_b the correction ω_1 becomes positive, which implies that slow spatial variations of channel width may speed up bar propagation.

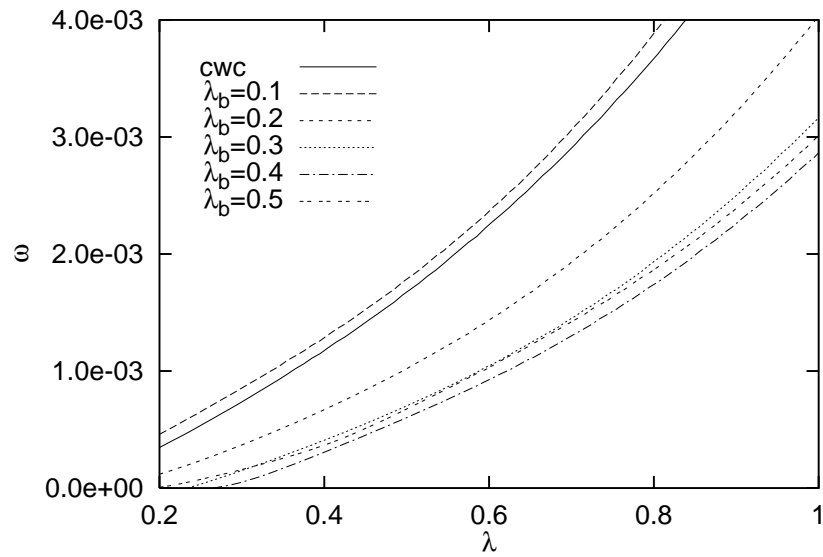


Figure 4.7: The total angular frequency ω of free bars is plotted versus λ for different values of λ_b ($\vartheta_0 = 0.2$, $d_s = 0.01$, $\beta = 18$, $\delta = 0.125$).

Chapter 5

Stability of bifurcations in channels with movable bed

5.1 Introduction

Channel bifurcations are fundamental features characterizing braided systems, being the formative braiding mechanism (figure 5.1). Their role is also crucial in fully developed braided networks: the evolution of a bifurcation governs water and sediment distribution into the downstream branches and slight changes at the channels division may strongly affect the topographic behavior of the downstream reaches. In the present chapter the stability of a bifurcation is investigated through a one dimensional numerical model. The bifurcation is defined stable when both branches remain open, while it is defined unstable when one branch tends to close and water and sediment discharge flows into the other. The abandonment of one branch may be due to an inherent instability of the system under suitable conditions or may be induced by external forcings, such as backwater effects, migration of bars through the bifurcation, changes of bed level in the downstream branches, etc.. The present work deals both with free instability of bifurcations and with the case of instability forced by the boundary conditions.

In one dimensional network models of rivers confluences and bifurcations form nodal points. The equations used to describe both processes are the same; nevertheless, there is a significant difference between modeling a confluence or a bifurcation: in the former case water and sediment discharges are known in both of the upstream branches; on the other hand, at a bifurcation it is necessary to decide how do water and sediment divide. Hence, a so called *nodal point relationship* is required, which determines the distribution of flow and bedload transport into the two downstream branches.



Figure 5.1: Bifurcation in a braided river, Sunwapta (Alberta, Canada).

In this chapter a quasi two dimensional nodal point relationship is presented. The results show that, in the absence of forcing effects, bifurcations are stable provided Shields stress exceed a threshold value, which depends on channel geometry and hydraulic conditions.

5.2 Previous contributions: Wang et al. (1995) model

In this section the main results of a previous theoretical work performed by Wang et al. (1995) on the stability of river bifurcations are presented. The authors consider the simple channel network sketched in figure 5.2 in which a river bifurcates into two branches ending in a lake. The attention is mainly devoted to the behavior of a river delta. The conditions under which the bifurcation loses stability are investigated through a one-dimensional model, in the absence of any forcing effect.

At the upstream section of the first channel water and sediment discharge are imposed while at the end of the two downstream branches water level is kept constant. A one dimensional model is unable to represent accurately water and sediment flow at the bifurcation; therefore, the establishment of suitable nodal point conditions turns out to be the crucial aspect of the approach. The authors propose the following relationships to be applied at the bifurcation:

- i) water discharge balance

$$Q_a = Q_b + Q_c; \quad (5.1)$$

- ii) sediment discharge balance

$$b_a q_a = b_b q_b + b_c q_c; \quad (5.2)$$

- iii) constance of water level

$$H_a = H_b = H_c; \quad (5.2a,b)$$

where Q is water discharge, q is sediment discharge per unit width, b is channel width and H water level (figure 5.3). Subscript a , b and c denote the different branches. Furthermore the authors introduce a so called *nodal point relation* which takes the form

- iv) nodal point relationship

$$\frac{b_b q_b}{b_c q_c} = \left(\frac{Q_b}{Q_c} \right)^k \left(\frac{b_b}{b_c} \right)^{1-k}, \quad (k > 1). \quad (5.3)$$

The latter condition is somehow arbitrary but it satisfies the following requirements

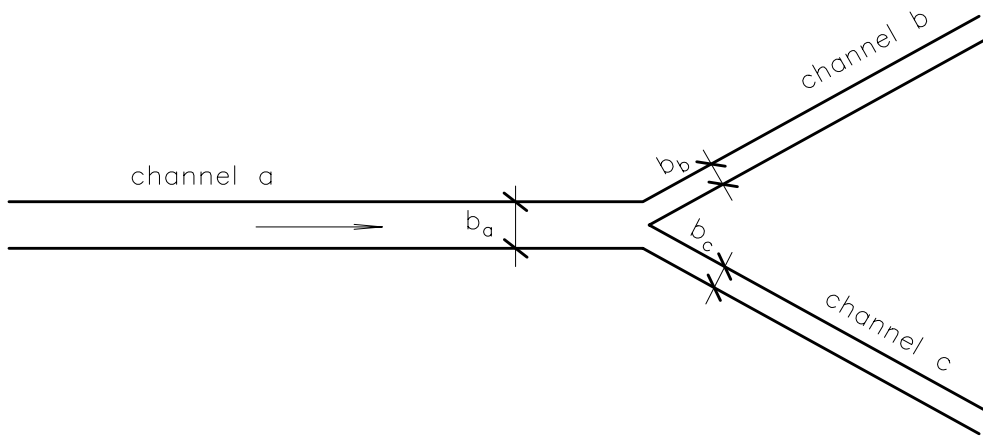


Figure 5.2: Geometry of the network.

- i) it is symmetric;
- ii) it allows the model to represent all possible physically realistic situations (stable and unstable bifurcations);
- iii) it allows only uniquely determined equilibrium conditions with both branches open.

The coefficient k is unknown; the only estimates provided by the authors give $k = 2$ and $k = 6$ for a real river and for a scale model of a bifurcation, respectively.

The authors suggest that the only possible equilibrium conditions for the network are the following

- i) both branches are open, each branch transports a part of the water and sediment;
- ii) branch b is closed ($Q_b = q_b = 0$) and all water and sediment is transported through branch c ;
- iii) branch c is closed ($Q_c = q_c = 0$) and all water and sediment is transported through branch b .

In order to analyze the stability of the equilibrium state the morphological development of the system far from the equilibrium is considered. To allow an analytical treatment of the problem the bathymetry of each branch is assumed to be represented by a single depth value. Furthermore the authors assume the flow to be uniform, even if the system is not in equilibrium. The

following relationships are used for water motion and sediment transport, respectively

$$Q_i = b_i C_i D_i^{3/2} S_i^{1/2}, \quad (5.4)$$

$$q_i = M \left(\frac{Q_i}{b_i D_i} \right)^n, \quad (5.5)$$

where i denotes the branch (a , b or c), C is dimensionless Chezy coefficient, D is water depth and S is channel slope.

Performing a linear stability analysis the authors determine the following set of differential equations, governing the development in time of the network

$$\frac{dD_b}{dt} = \phi_1(D_b, D_c), \quad (5.6a)$$

$$\frac{dD_c}{dt} = \phi_2(D_b, D_c), \quad (5.6b)$$

where ϕ_1 and ϕ_2 are functions of the flow depths of the downstream channels. Notice that at the equilibrium $\phi_1 = \phi_2 = 0$. The eigenvalues of the Jacobian of the system govern the stability of the bifurcation. If the real parts of the eigenvalues are negative, perturbations decay exponentially in time and the equilibrium is stable; if one of the eigenvalues has positive real part, the equilibrium is unstable. The results of the analysis suggest that the bifurcation is stable, provided the following requirement be satisfied

$$k > n/3, \quad (5.7)$$

where k is the exponent of the nodal point relationship (5.3) and n is the exponent of the sediment transport law (5.5). On the other hand, if $k < n/3$ the configuration with both branches open is unstable.

In the following the results of Wang et al. (1995) will be tested under non uniform flow conditions; then a physically based nodal point relation will be proposed.

5.3 Formulation of the problem

5.3.1 Problem for a single channel

The problem is formulated in the context of a one dimensional model, in terms of dimensional variables D , H and Q which are water depth, free surface elevation and water discharge, respectively (figure 5.3). Furthermore we assume the cross section to be rectangular and infinitely wide.

The continuity and flow equations in one dimensional form read

$$bD_{,t} + Q_{,x} = 0, \quad (5.8a)$$

$$Q_{,t} + \left(\frac{Q^2}{\Sigma} \right)_{,x} + g\Sigma H_{,x} + g\Sigma j = 0, \quad (5.8b)$$

where b is channel width, g is gravity, Σ is cross section area and j is defined as follows

$$j = \frac{\tau}{\rho g R_h}, \quad (5.9)$$

where τ is bed shear stress and R_h the hydraulic radius which coincides with the flow depth D for wide channels.

The flow field equations are coupled with sediment continuity equation; in the one-dimensional form it reads

$$(1 - p)\eta_{,t} + q_{,x} = 0, \quad (5.10)$$

where q is sediment transport per unit width, p is sediment porosity and η is bed elevation, defined as

$$\eta = H - D. \quad (5.11)$$

In order to complete the mathematical formulation of the problem we need to introduce suitable closures to model j and the solid discharge q . Using the relationship proposed by Gauckler and Strickler j is expressed in terms of local values of flow characteristics in the form

$$j = \frac{Q|Q|}{k_s^2 \Sigma^2 D^{4/3}}, \quad (5.12)$$

where k_s is Strickler coefficient.

Following a well established procedure originally introduced by Einstein (1950) bedload transport per unit width can be written as follows

$$q = \Phi(\vartheta, \vartheta_c) \sqrt{\frac{\rho_s - \rho}{\rho}} g d_s^3, \quad (5.13)$$

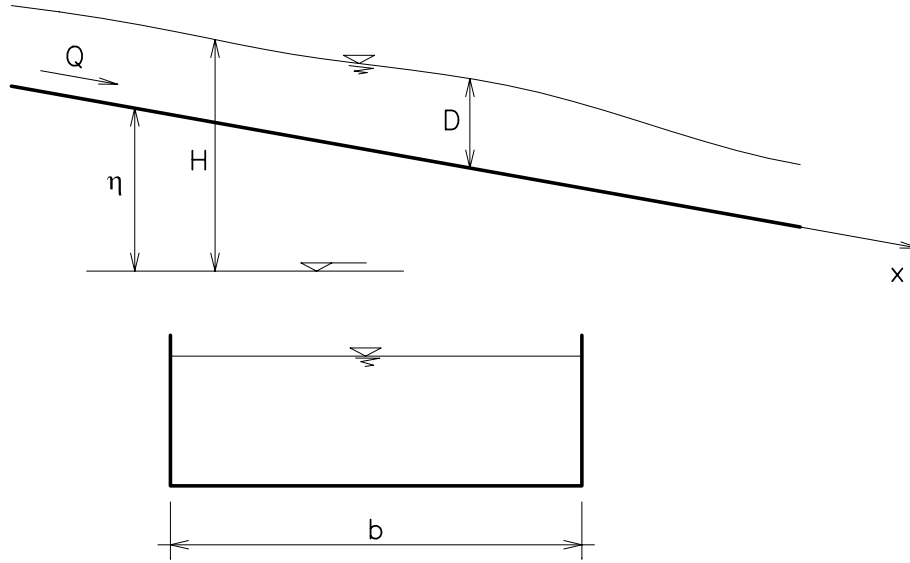


Figure 5.3: Notation.

where Φ is the bedload function given in terms of the local value of Shields parameter ϑ . Furthermore, ϑ_c is the critical value of Shields stress below which sediment does not move. In the following Φ is evaluated through Meyer-Peter & Müller (1948) formula. Hence bed load function is written in the form

$$\Phi = 8(\vartheta - \vartheta_c)^{3/2}, \quad (5.14)$$

and $\vartheta_c = 0.047$.

In terms of the variables of the problem Shields parameter reads

$$\vartheta = \frac{Q^2}{(s-1)d_s k_s^2 b^2 D^{7/3}}, \quad (5.15)$$

where

$$s - 1 = \frac{\rho_s - \rho}{\rho}. \quad (5.16)$$

Equation (5.15) implies that the bed load is a function of local values of water depth and discharge

$$q = q(D, Q). \quad (5.17)$$

The final form of the governing equations for constant width channels is obtained in the form

$$bD_{,t} + Q_{,x} = 0, \quad (5.18a)$$

$$Q_{,t} + \frac{2Q}{\Sigma} Q_{,x} + g\Sigma (H_{,x} + j) - b \frac{Q^2}{\Sigma^2} D_{,x} = 0, \quad (5.18b)$$

$$(1-p)bh_{,t} + (1-p)Q_{,x} + bq_{,\vartheta} (\vartheta_D D_{,x} + \vartheta_Q Q_{,x}) = 0, \quad (5.18c)$$

where the following coefficients have been defined

$$\vartheta_Q = \left. \frac{\partial \vartheta}{\partial Q} \right|_D = \frac{2Q}{(s-1)d_s k_s^2 D^{7/3} b^2}, \quad (5.19a)$$

$$\vartheta_D = \left. \frac{\partial \vartheta}{\partial D} \right|_Q = -\frac{7Q^2}{3(s-1)d_s k_s^2 b^2 D^{10/3}}. \quad (5.19b)$$

The system (5.18a-c) is hyperbolic and it is characterized by two characteristic curves propagating downward and by one propagating upward, both in the case of supercritical and subcritical flow.

As for the initial condition, we need to specify the value of the unknowns D , H and Q along the spatial domain at the initial time $t = 0$. In general the solution for the steady flow over the initial bed configuration is used for this purpose, which is obtained solving system (5.18a-c) under steady conditions

$$Q_{,x} = 0, \quad (5.20a)$$

$$\frac{2Q}{\Sigma} Q_{,x} + g\Sigma (H_{,x} + j) - b \frac{Q^2}{\Sigma^2} D_{,x} = 0, \quad (5.20b)$$

for given water discharge at the upstream section and given water level at the upstream or downstream section depending on the flow be super-critical or sub-critical. From (5.20a,b) $D(x, 0)$ and $H(x, 0)$ are computed once a fixed bed level is given; water discharge at the initial time ($t = 0$) is constant along the spatial domain, hence $Q(x, 0) = Q(0, 0)$.

As for the boundary conditions, under unsteady flow, water and sediment discharges are imposed at the upstream section as functions of time. Recalling equation (5.17), setting the above conditions is equivalent to assign two independent relationships of the type

$$\mathcal{F}[Q(0, t), D(0, t)] = 0. \quad (5.21)$$

In the present case the first condition sets the flow discharge $Q(0, t)$ as a given function of time, while the second condition implies a relationship between Q and D which must reproduce the given sediment discharge.

At the downstream section water level $H(L, t)$ is imposed or, a suitable stage-discharge relationship which involves $Q(L, t)$, $H(L, t)$ and $D(L, t)$, where L is the domain length.

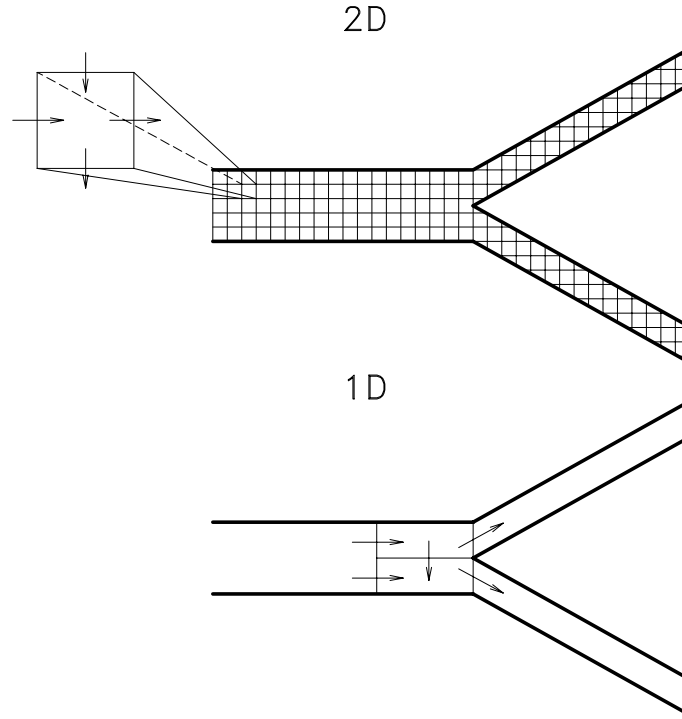


Figure 5.4: Sketch of the nodal point condition.

5.3.2 Problem for a channels network

In the following the stability of the simple channel network considered by Wang et al. (1995) is investigated (figure 5.2); in particular, the downstream branches have the same width, which is equal to the half width of the upstream branch ($b_a = 2b_b = 2b_c$), and the initial slope is constant in all the channels ($S_a = S_b = S_c$).

As showed in section 5.3.1, in order to solve the equations for each branch, two boundary conditions are needed at the upstream section and one at the downstream section. Water and sediment discharges are imposed at channel a inlet while water level is set at channels b and c outlets. As underlined by Wang et al. (1995) the most critical issue is to determine the five nodal point conditions.

In the first attempt the nodal point relationships proposed by Wang et al. (1995) have been used, which read

$$Q_a = Q_b + Q_c, \quad (5.22a)$$

$$b_a q_a = b_b q_b + b_c q_c, \quad (5.22b)$$

$$H_a = H_b = H_c, \quad (5.22c)$$

$$\frac{b_b q_b}{b_c q_c} = \left(\frac{Q_b}{Q_c} \right)^k \left(\frac{b_b}{b_c} \right)^{1-k}, \quad (k > 1). \quad (5.22d)$$

Condition (5.22d) plays a crucial role in the analysis of river bifurcations. The adoption of (5.22d) requires the introduction of a suitable value of k which is a-priori unknown. Furthermore k may be a function of local flow conditions and bed topography, which implies that k may change in time.

In order to overcome these difficulties a physically based nodal point condition is proposed in the following. The new approach is based on the recognition that, within the context of a two dimensional approach, a nodal point condition is no longer required: with reference to figure 5.4 the solution is obtained by solving flow field and sediment continuity equations for each computational cell. A similar approach has been followed in the present analysis where a quasi two-dimensional model is introduced in the neighborhood of the bifurcation. The last computational cell before the bifurcation, with a length of αb_a , is split longitudinally into two subcells. Exner equation is applied to both, assuming the incoming solid discharge to be uniformly distributed at the upstream section and taking into account a transverse component of bedload transport between the two cells. Sediment transport leaving both cells is then fed as supply to the downstream branches of the network. From physical point of view the coefficient α can be evaluated estimating the upward distance from the nodal point at which the effect of the bifurcation is felt.

Within a two dimensional approach, the transverse component of bedload transport consists of two terms, the first being proportional to transverse velocity and the second being dependent on transverse bed slope; following Ikeda (1982) we write

$$q_y = \Phi \sin \alpha, \quad (5.23)$$

where Φ is the bed load function and

$$\sin \alpha = V (U^2 + V^2)^{-1/2} - \frac{r}{\vartheta^{1/2}} (H - D)_{,y}, \quad (5.24)$$

where r is an empirical constant ranging between 0.3 and 0.6, (U, V) are longitudinal and transverse velocity components, respectively and y is transverse coordinate.

In the present case the transverse bedload component is treated in a similar way, thus we write

$$q_y = q_a \left[\frac{Q_t D_a}{Q_a \alpha D_{abc}} - \frac{r}{\sqrt{\vartheta}} \frac{\partial \eta}{\partial n} \right], \quad (5.25)$$

where

$$Q_t = \frac{Q_b - Q_c - Q_a \left(\frac{b_b - b_c}{b_a} \right)}{2}, \quad D_{abc} = \frac{1}{2} \left(\frac{D_b + D_c}{2} + D_a \right). \quad (5.26a,b)$$

In order to evaluate the transverse bed slope the difference between bottom elevation at the inlet of the two downstream channels is considered, divided by a fraction of the upstream branch width $t_b b_a$; typically $t_b = 0.5$ is assumed.

It should be noticed that applying Exner equation to the two sections of the last cell implies that the condition (5.22b) must not be accounted for: depositions and scours are possible at the bifurcation.

The nodal point conditions then read

i) water discharge balance

$$Q_a = Q_b + Q_c; \quad (5.27)$$

ii) constance of water level

$$H_a = H_b = H_c; \quad (5.28a,b)$$

iii) sediment continuity equation applied to the two sections of the last cell

$$\frac{1}{2}(1-p)\eta_{b,t} + \frac{q_b - q_a}{\alpha b_a} - \frac{q_y}{b_b} = 0, \quad (5.29a)$$

$$\frac{1}{2}(1-p)\eta_{c,t} + \frac{q_c - q_a}{\alpha b_a} + \frac{q_y}{b_c} = 0. \quad (5.29b)$$

The influence of α and t_b on the results will be discussed in section 5.5.2.

5.4 Numerical scheme

In order to solve system (5.18a-c) a so called *box scheme* originally proposed by Preissmann (1961) and Preissmann & Cunge (1961) is used, where a four points rectangular mesh is adopted (figure 5.5). Time and space derivatives are computed as weighted average of finite differences, evaluated in adjacent points along the perimeter of the cell. Introducing the temporal and spatial weight coefficients θ and ψ , ranging from 0 to 1, it follows that the derivatives of the generic variable f read

$$\frac{\partial f}{\partial t} = [(1 - \psi)(f_j^{k+1} - f_j^k) + \psi(f_{j+1}^{k+1} - f_{j+1}^k)] \frac{1}{\Delta t}, \quad (5.30a)$$

$$\frac{\partial f}{\partial x} = [(1 - \theta)(f_{j+1}^k - f_j^k) + \theta(f_{j+1}^{k+1} - f_j^{k+1})] \frac{1}{\Delta x}. \quad (5.30b)$$

Usually ψ is equal to 0.5 while θ ranges from 0.5 to 1 to avoid numerical instabilities; in the present case the value $\theta = 0.6$ has been used. Hence, the computational point is centered in space and shifted in time toward time $k + 1$.

Substituting expressions (5.30a,b) into equations (5.18a-c) and assuming a constant spatial step Δx , we obtain

$$\begin{aligned} & \frac{b}{2\Delta t} (D_j^{k+1} - D_j^k + D_{j+1}^{k+1} - D_{j+1}^k) + \\ & + \frac{1}{\Delta x} [\theta (Q_{j+1}^{k+1} - Q_j^{k+1}) + (1 - \theta) (Q_{j+1}^k - Q_j^k)] = 0, \end{aligned} \quad (5.31a)$$

$$\begin{aligned} & \frac{1}{2\Delta t} (Q_j^{k+1} - Q_j^k + Q_{j+1}^{k+1} - Q_{j+1}^k) + \\ & + \frac{(S_1)_{j+1/2}^{k+\theta}}{\Delta x} [\theta (Q_{j+1}^{k+1} - Q_j^{k+1}) + (1 - \theta) (Q_{j+1}^k - Q_j^k)] + \\ & + \frac{(S_2)_{j+1/2}^{k+\theta}}{\Delta x} [\theta (H_{j+1}^{k+1} - H_j^{k+1}) + (1 - \theta) (H_{j+1}^k - H_j^k)] + \\ & + \frac{(S_3)_{j+1/2}^{k+\theta}}{\Delta x} [\theta (D_{j+1}^{k+1} - D_j^{k+1}) + (1 - \theta) (D_{j+1}^k - D_j^k)] + \\ & + (S_4)_{j+1/2}^{k+\theta} = 0, \end{aligned} \quad (5.31b)$$

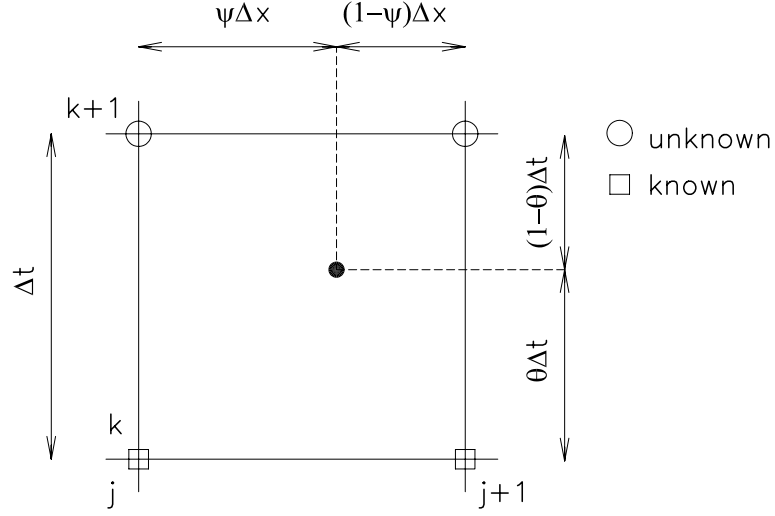


Figure 5.5: Numerical cell.

$$\begin{aligned}
& \frac{(1-p)b}{2\Delta t} [H_j^{k+1} - H_j^k + H_{j+1}^{k+1} - H_{j+1}^k] + \\
& + \frac{(S_5)_{j+1/2}^{k+\theta}}{\Delta x} [\theta (Q_{j+1}^{k+1} - Q_j^{k+1}) + (1-\theta) (Q_{j+1}^k - Q_j^k)] + \\
& + \frac{(S_6)_{j+1/2}^{k+\theta}}{\Delta x} [\theta (D_{j+1}^{k+1} - D_j^{k+1}) + (1-\theta) (D_{j+1}^k - D_j^k)] = 0. \quad (5.31c)
\end{aligned}$$

The coefficients S_i , ($i = 1, 6$) are defined as follows

$$S_1 = 2\frac{Q}{\Sigma}, \quad (5.32a)$$

$$S_2 = g\Sigma, \quad (5.32b)$$

$$S_3 = -b\frac{Q^2}{\Sigma^2}, \quad (5.32c)$$

$$S_4 = g\Sigma j, \quad (5.32d)$$

$$S_5 = 1 - p + bq_{,\vartheta} \vartheta_Q, \quad (5.32e)$$

$$S_6 = bq_{,\vartheta} \vartheta_D \quad (5.32f)$$

and they are evaluated at the computational point using an weighted average as follows

$$(S_i)_{j+1/2}^{k+\theta} = \frac{1}{2} \left\{ \theta \left[(S_i)_j^{k+1} + (S_i)_{j+1}^{k+1} \right] + (1 - \theta) \left[(S_i)_j^k + (S_i)_{j+1}^{k+1} \right] \right\}. \quad (5.33)$$

5.4.1 Solution for a single channel

A useful technique for the solution of non linear algebraic systems is the *double sweep method* introduced by Richtmyer & Morton (1967), which is an adaptation of Gauss method. At each time step the solution requires the preliminary linearization of system (5.31a-c), obtained imposing $\theta = 0$ in the coefficients (5.33).

If $j = 0, 1, 2, \dots, N$, a system of equations of the type (5.31a-c) can be written for each of the N sections. Hence, we have $3(N + 1)$ unknowns at time $k + 1$, and $3N$ equations. Three additional equations are obtained from the boundary conditions. System (5.31a-c) can be written as follows

$$A_j^1 Q_{j+1}^{k+1} + B_j^1 Q_j^{k+1} + C_j^1 H_{j+1}^{k+1} + D_j^1 H_j^{k+1} + E_j^1 D_{j+1}^{k+1} + F_j^1 D_j^{k+1} = L_j^1, \quad (5.34a)$$

$$A_j^2 Q_{j+1}^{k+1} + B_j^2 Q_j^{k+1} + C_j^2 H_{j+1}^{k+1} + D_j^2 H_j^{k+1} + E_j^2 D_{j+1}^{k+1} + F_j^2 D_j^{k+1} = L_j^2, \quad (5.34b)$$

$$A_j^3 Q_{j+1}^{k+1} + B_j^3 Q_j^{k+1} + C_j^3 H_{j+1}^{k+1} + D_j^3 H_j^{k+1} + E_j^3 D_{j+1}^{k+1} + F_j^3 D_j^{k+1} = L_j^3, \quad (5.34c)$$

where all the coefficients are defined in appendix B.

Imposing

$$Q_j = G_j H_j + L_j, \quad (j = 0, 1, 2, \dots, N) \quad (5.35)$$

and

$$D_j = M_j H_j + N_j, \quad (j = 0, 1, 2, \dots, N), \quad (5.36)$$

from (5.34a-c) we obtain the following relationships

$$\begin{aligned} G_{j+1} &= \frac{B_j' C_j'' - B_j'' C_j'}{A_j'' C_j' - A_j' C_j''}, & L_{j+1} &= \frac{C_j' D_j'' - C_j'' D_j'}{A_j'' C_j' - A_j' C_j''}, \\ M_{j+1} &= \frac{B_j' A_j'' - B_j'' A_j'}{C_j'' A_j' - C_j' A_j''}, & N_{j+1} &= \frac{A_j' D_j'' - A_j'' D_j'}{C_j'' A_j' - C_j' A_j''} \end{aligned} \quad (5.37a-d)$$

and an expression for H_j which reads

$$H_j = \frac{\bar{C}_j - A_j^2 Q_{j+1} - C_j^2 h_{j+1} - E_j^2 D_{j+1}}{\bar{A}_j}, \quad (5.38)$$

where all the coefficients are reported in appendix B.

Equations (5.35), (5.36) and (5.38) allow one to obtain three relationships that can be solved recursively upward, once the coefficients G_j, L_j, M_j, N_j ($j = 1, 2, \dots, N$) and $\bar{C}_j, A_j^2, C_j^2, E_j^2, \bar{A}_j$ ($j = 0, 1, \dots, N - 1$) are determined. Provided the upstream boundary conditions be given in the form $Q_0 = Q(t)$ and $D_0 = D(t)$, the solution proceeds through the following steps.

- i) Setting of the upstream boundary conditions: from (5.37a-d) it follows

$$G_0 = 0, \quad L_0 = Q(t), \quad (5.39a,b)$$

$$M_0 = 0, \quad N_0 = D(t), \quad (5.40a,b)$$

with $t = t_0 + (k + 1)\Delta t$.

- ii) First sweep (downward): computation of the coefficients $G_j, L_j, M_j, N_j, \bar{C}_j, A_j^2, C_j^2, E_j^2, \bar{A}_j$.
- iii) Setting of the downstream boundary condition: evaluation of the unknown values Q_N, D_N, H_N .
- iv) Second sweep (upward, j runs from $N - 1$ to 0): Q_j, D_j, H_j are determined through the solution in section ($j + 1$), using equation (5.38) to determine H_j and equations (5.35), (5.36) to determine Q_j and D_j , respectively.

Once obtained a first approximation of the solution for Q_j^{k+1}, D_j^{k+1} and H_j^{k+1} the above procedure is iterated, the coefficients S_j are now evaluated through equation (5.33) with $\theta \neq 0$.

5.4.2 Solution for a channel network

The solution for a free surface channel network can be obtained splitting the system into an appropriate number of subsystems and solving equations (5.18a-c) for each of them. The technique used herein, originally proposed by Shaffranek et al. (1981), allows one to solve a network under unsteady conditions in a very efficient way. At first, the boundary values of each unknown are computed for all the branches of the network; then the equations are solved along each branch using the scheme presented in section 5.4.1.

System (5.18a-c) can be written in matrix form for a network as follows

$$\alpha_j W_{j+1} + \beta_j W_j = \gamma_j, \quad (5.41)$$

with

$$\begin{aligned} W_j &= \begin{pmatrix} Q_j \\ D_j \\ H_j \end{pmatrix}, & \alpha_j &= \begin{pmatrix} A_j^1 & E_j^1 & C_j^1 \\ A_j^2 & E_j^2 & C_j^2 \\ A_j^3 & E_j^3 & C_j^3 \end{pmatrix}, \\ \beta_j &= \begin{pmatrix} B_j^1 & F_j^1 & D_j^1 \\ B_j^2 & F_j^2 & D_j^2 \\ B_j^3 & F_j^3 & D_j^3 \end{pmatrix}, & \gamma_j &= \begin{pmatrix} L_j^1 \\ L_j^2 \\ L_j^3 \end{pmatrix}. \end{aligned} \quad (5.42\text{a-d})$$

It follows

$$W_{j+1} = \zeta_j W_j + \eta_j, \quad (5.43)$$

where

$$\zeta_j = \alpha_j^{-1} \beta_j, \quad \eta_j = \alpha_j^{-1} \gamma_j. \quad (5.44\text{a,b})$$

Applying recursively equation (5.43) Q_0 , D_0 and H_0 at the upstream end of each branch can be related with Q_N , D_N and H_N at the downstream end of the same branch. In fact

$$W_1 = \zeta_0 W_0 + \eta_0, \quad (5.45)$$

$$W_2 = \zeta_1 W_1 + \eta_1 = \zeta_1 \zeta_0 W_0 + \zeta_1 \eta_0 + \eta_1, \quad (5.46)$$

from which

$$W_N = \xi W_0 + \bar{\eta}, \quad (5.47)$$

where

$$\xi = \prod_{i=0}^{N-1} \zeta_i, \quad (5.48\text{a})$$

$$\bar{\eta} = \eta_{N-1} + \sum_{k=0}^{N-2} \left(\prod_{i=k+1}^{N-1} \zeta_i \right) \eta_k. \quad (5.48\text{b})$$

A relationship like (5.47) which relates the values of the unknowns at the upstream and the downstream end of each channel, can be written for each branch of the network. Three algebraic equations are found, for the six values Q_0 , D_0 , H_0 , Q_N , D_N , H_N . For a network of m branches $3m$ relations are written, which, combined with the $3m$ boundary conditions (external and internal), determine a system of $6m$ equations. The solution of this system allows one to determine the $6m$ unknowns, i. e. the values of Q , D , and H at the boundaries of each channel.

In the present case we consider the network sketched in figure 5.2. Hence, it is necessary to set nine conditions, three for each channel. The four external boundary conditions have been described in section 5.3.1, the remaining five conditions are imposed at the nodal point as discussed in section 5.3.2.

The resulting algebraic system involves 18 equations in the unknowns $(Q_{i0}, D_{i0}, h_{i0}, Q_{iN}, D_{iN}, h_{iN})$ with $(i = a, b, c)$. Nine equations are obtained from system (5.47), four are given by the external conditions and five arise from the internal conditions at the nodal point. The system is solved using the Newton method. Equations (5.31a-c) are then solved in each branch of the network using the procedure described in section 5.4.1.

5.5 Results

5.5.1 Single channel

In this section the numerical model has been tested in order to ascertain its suitability to describe the development of natural channels. A single branch has been considered: starting from initial uniform conditions the system is perturbed by changing the boundary conditions. It is possible to demonstrate that, within the context of a one dimensional model, the only possible equilibrium configuration for the flow on movable bed with constant width is the uniform flow. In fact, under such conditions, the governing equations (5.18a-c) reduce to the simple form

$$Q_{,x} = 0, \quad (5.49a)$$

$$H_{,x} = -S, \quad (5.49b)$$

$$q_{,x} = 0. \quad (5.49c)$$

Hence, in the following examples, the final configuration achieved by the system for given (steady) boundary conditions is readily analytically predictable.

The numerical tests have been carried out using the geometric and hydraulic characteristics of a laboratory scale model.

Increase of sediment discharge at the upstream section

The numerical experiment starts from an initial uniform configuration with the following characteristics

- channel width: $b=0.6\text{m}$;
- channel length: $L=18\text{m}$;
- channel slope: $S=0.008$;
- Strickler coefficient: $k_s=70\text{m}^{1/3}\text{s}^{-1}$;
- sediment diameter: $d_s=1.2\text{mm}$.

The initial boundary conditions impose

- $Q=20\text{l/s}$ at the upstream section;

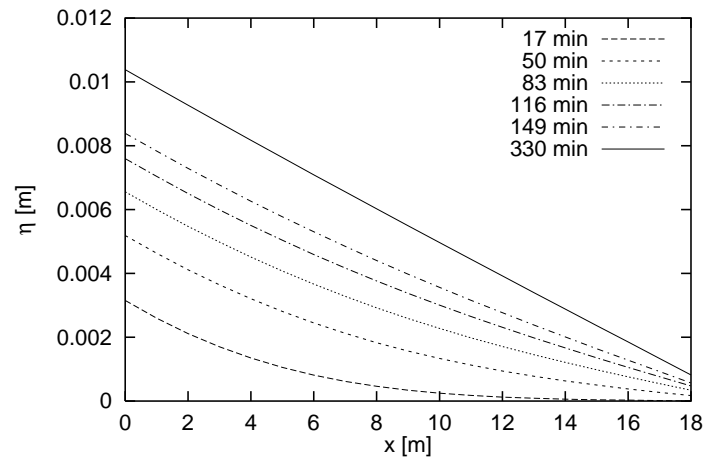


Figure 5.6: Bed profiles at different times; the sediment discharge has been increased by 10%. The initial channel slope has been filtered out from bed profile.

- $D = D_u$ at the upstream section;
- $D = D_u$ at the downstream,

where D_u is the uniform flow depth.

The sediment discharge at the upstream section is increased by 10% instantaneously and kept constant in time until a new equilibrium condition is reached. For the numerical solution a spatial step $\Delta x = 1\text{m}$ and a time step $\Delta t = 10\text{s}$ have been adopted.

In figure 5.6 bed configurations at different times are showed: it appears that the transient is characterized by an upstream deposition which gradually propagates downward. The final configuration reached by the channel displays a constant slope which is in equilibrium with prescribed sediment discharge, in agreement with theoretical predictions.

Increase of water level at the downstream section

Starting from the same uniform flow of the previous test, the water level at the downstream section is raised instantaneously to a depth of two times the initial one and it is kept constant in time since a new steady condition is reached by the system. For the numerical solution a spatial step $\Delta x = 0.4\text{m}$ and a time step $\Delta t = 10\text{s}$ have been adopted.

Notice that the flow is supercritical, the initial uniform configuration being characterized by a Froude number $F = 1.13$. In figure 5.7 bed and free

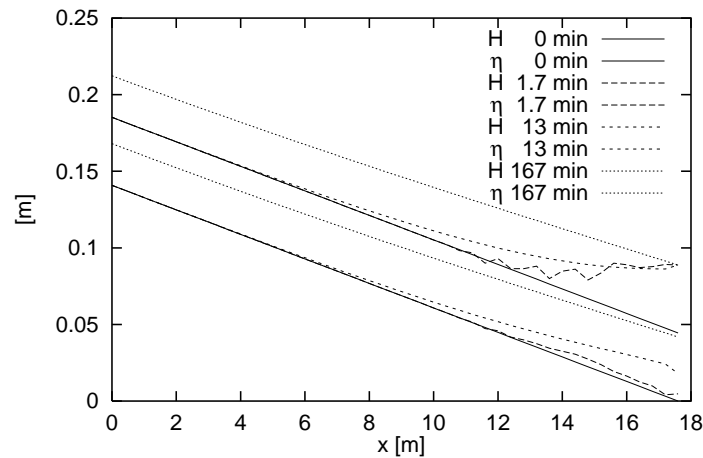


Figure 5.7: Bed and water level profiles at different times; the water level has been increased by 100%.

surface elevations are plotted at different times. The transient is characterized by the generation of a deposition at the channel outlet which propagates upward until the initial given slope is re-established. The model seems able to cope with relatively weak discontinuities; however, during the first part of the transient, some numerical instabilities are generated as shown in figure 5.7.

5.5.2 Channel network

In the present section the stability of a bifurcation is investigated through the numerical model which makes use of the nodal conditions (5.27), (5.28a,b) and (5.29a,b) proposed in section 5.3.2.

Free instability

We now consider the problem of the free stability of a bifurcation. As for the external boundary conditions we impose water and sediment discharge at the upstream section of branch *a* and the uniform flow condition at the outlets of channels *b* and *c* (see figure 5.2 for the geometry of the network). The initial configuration is characterized by a unique slope in all the branches; furthermore, water and sediment discharges are equally distributed in the two downstream branches. The system is perturbed by the introduction of a small bump of sediments in channel *b*. Depending upon the geometry of the network and flow and sediment characteristics the model predicts both situations of stable and unstable bifurcation.

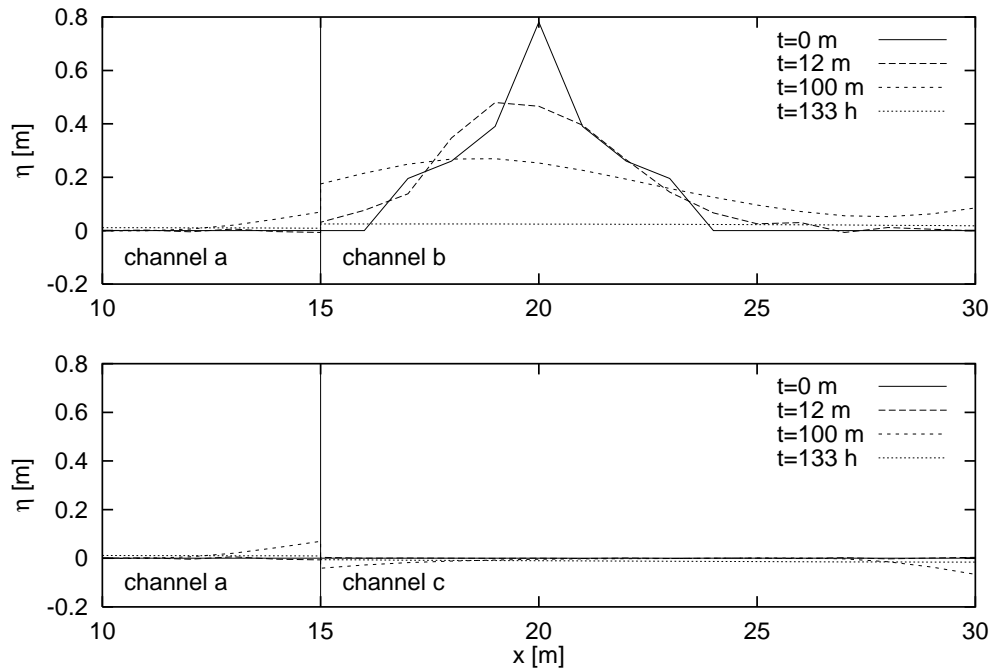


Figure 5.8: Bottom profile development under stable conditions. The initial channel slope has been filtered out from bed profile.

In figure 5.8 the typical behavior under stable conditions is showed: the sediment bump migrates upstream along channel *b* (the flow is supercritical) and it is progressively damped and diffused. After some time deposition occurs along the whole channel *b*, whose height slowly decays in time since the unperturbed initial configuration is re-established by the system. Channel *c* is almost unaffected by the presence of the sediment bump except for a small erosion at the inlet which does not propagate along the channel. A relatively small deposition is generated at the downstream end of branch *a* during the initial stage of the process. In figure 5.9 the behavior of the network under unstable conditions is reported. The initial phase does not differ significantly from that of the stable case; however the deposition in branch *b* grows in time and consequently in branch *c* undergoes an erosion process. The numerical simulation ends when Shields stress in channel *b* falls below the critical value for sediment motion.

Numerical results suggest that, given the geometry of the channel, it is possible to find a threshold value of Shields parameter ϑ above which the bifurcation is stable and below which it is unstable. Notice that braided rivers, in which the bed configuration is strongly unstable, are characterized

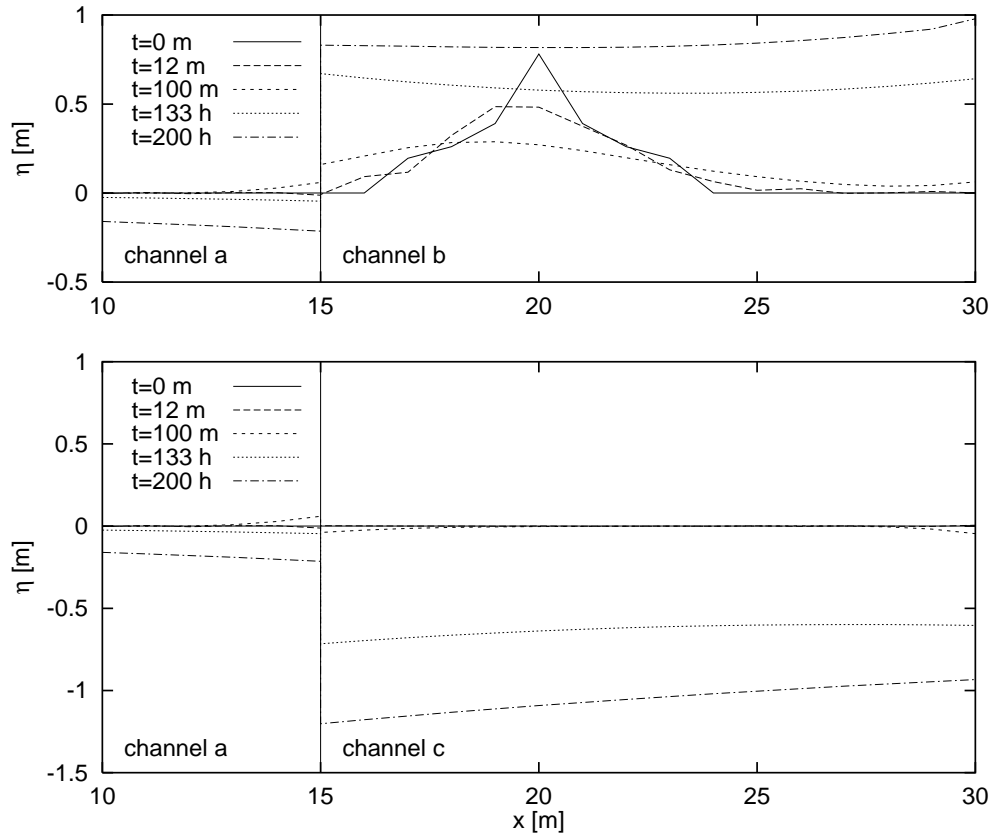


Figure 5.9: Bottom profile development under unstable conditions. The initial channel slope has been filtered out from bed profile.

by values of Shields stress close to the critical conditions. In figure 5.10 the threshold value of ϑ is plotted versus the width ratio of channel a for two different values of Froude number, corresponding to subcritical and supercritical flow. The plot shows that as the width ratio of the channel increases, larger values of Shields stress are needed to ensure the stability of the bifurcation. It is worth pointing out that the threshold value of Shields parameter seems to be weakly dependent on Froude number as appears from figure 5.11 in which the neutral stability curve is plotted versus Froude number.

Furthermore, we note that in the nodal conditions (5.29a,b) the coefficients α and t_b appear, which are involved into the evaluation of the length of the nodal cell and of the transverse bed slope, respectively. These parameters need a suitable tuning in order to describe the development of real bifurcations. In figures 5.12 and 5.13 the dependence of the threshold value of Shields stress on these parameters is shown, for given channels width and

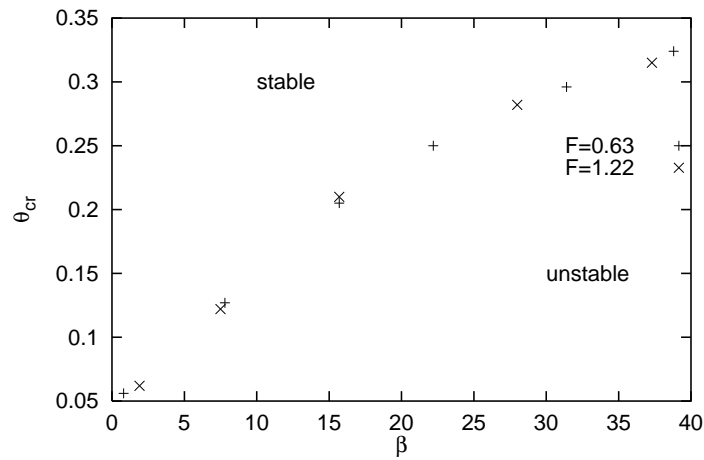


Figure 5.10: The critical Shields number θ is plotted versus the width ratio β for different Froude numbers (channels width $b=50\text{m}$, channels slope $S=0.008$).

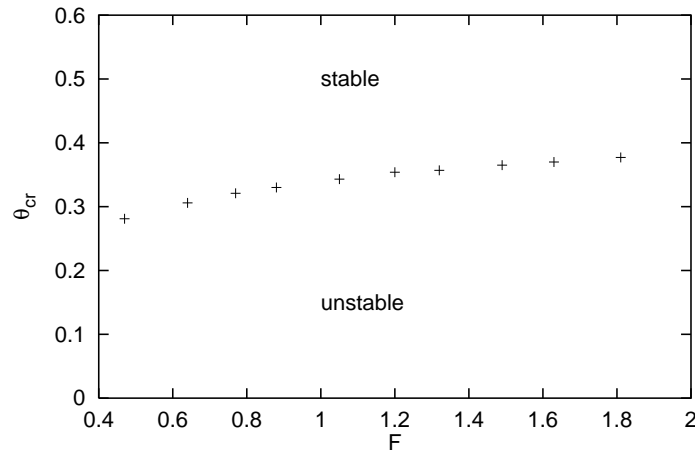


Figure 5.11: The critical Shields number θ is plotted versus the Froude number F (channels width $b=50\text{m}$, channels slope $S=0.008$).

slope. It appears that the solution is affected by the values of both the parameters, however the dependence of the results on α and t_b decreases increasing their values. In all the numerical simulations the following choice has been pursued: $\alpha=1.3$, $t_b=0.5$. The stabilizing role of the transverse slope is found to be crucial to predict stable conditions: assuming $t_b \rightarrow \infty$ the model always predicts instability, even for very large values of Shields stress.

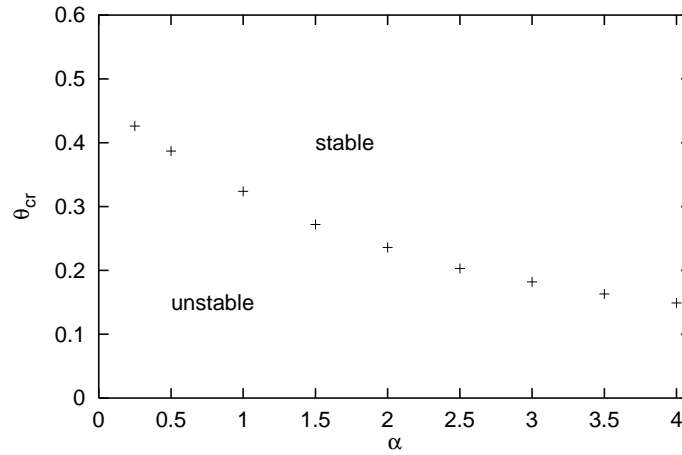


Figure 5.12: The critical Shields number θ is plotted versus the coefficient α (channels width $b=50\text{m}$, channels slope $S=0.008$).

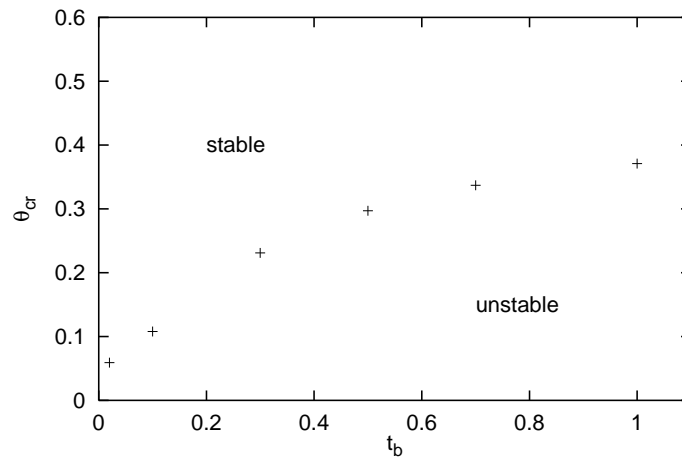


Figure 5.13: The critical Shields number θ is plotted versus the coefficient t_b (channels width $b=50\text{m}$, channels slope $S=0.008$).

Forced instability

Let now consider the problem of the stability of a bifurcation subject to a forcing effect induced by non uniform boundary conditions. This is typically the situation characterizing braided rivers in which the branches are relatively short due to the continuous interplay of channels. In the numerical simulation the initial configuration is characterized by a unique slope in all the branches; water and sediment discharges are equally distributed into branches b and c .

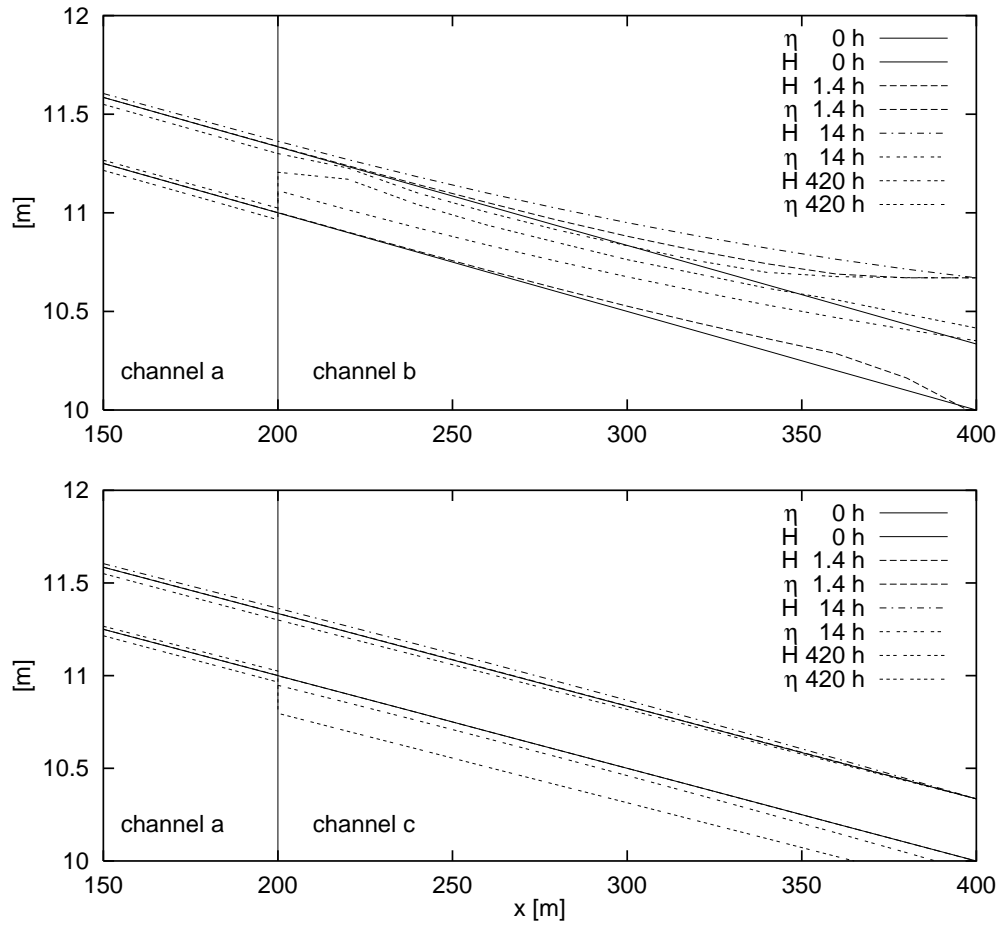


Figure 5.14: Bottom and free surface profile development forced by raising water level at the downstream end of channel *b*.

Water level at the downstream end of channel *b* is raised instantaneously to a depth of two times the initial one and kept constant in time. Figure 5.14 shows the behavior in time of free surface and bed elevation. It appears that a deposition occurs at channel *b* outlet, that propagates upward; at the same time channel *c* is subject to an erosion process almost uniform along all the branch. A step on bed elevation forms at the inlets of the two divided channels, which rapidly grows in time. Starting from the downstream section, the flow in channel *b* is no longer able to transport sediment; the numerical run is stopped when Shields stress falls below the critical value for sediment motion, along all the branch. Channel *a* is almost unaffected by this behavior.

5.5.3 Comparison with the results of Wang et al. (1995)

In this section a comparison with the theoretical findings of Wang et al. (1995) is presented: the nodal point conditions (5.22a-d) proposed by the authors have been adopted for this purpose.

Wang et al. (1995) analysis predicts stability provided $k > n/3$, where k and n are the exponents of the nodal point condition (5.22d) and of the bedload transport law (5.5), respectively. In the present case sediment discharge is described through Meyer-Peter and Müller formula which does not imply a constant value of n ; it is easy to demonstrate that for $\vartheta \rightarrow 0$ we have $n \rightarrow \infty$ while for $\vartheta \rightarrow \infty$ we have $n \rightarrow 0.9$.

In figure 5.15 the threshold value of k above which the bifurcation is stable is plotted versus Shields parameter for different values of Froude number: the marginal stability curve agrees satisfactorily with the theoretical predictions of Wang et al. (1995). It is worth pointing out that the threshold value of k is completely independent on Froude number.

The imposition of the nodal conditions (5.27), (5.28a,b) and (5.29a,b) described in section 5.3.2 allows one to determine water and sediment distribution into the two downstream branches; hence it is possible to evaluate numerically the exponent k of the nodal point condition (5.22d). In figure 5.16 the value of k is plotted versus time for different values of Shields parameter; both stable and unstable conditions are considered. It appears that k is strongly dependent on time when the system is far from equilibrium conditions. This result implies that the nodal point relationship proposed by Wang et al. (1995) is not applicable to describe the development of a natural bifurcation: the value of k is a function of the geometry of the bifurcation and it can change in time depending on the topographic development of the system.

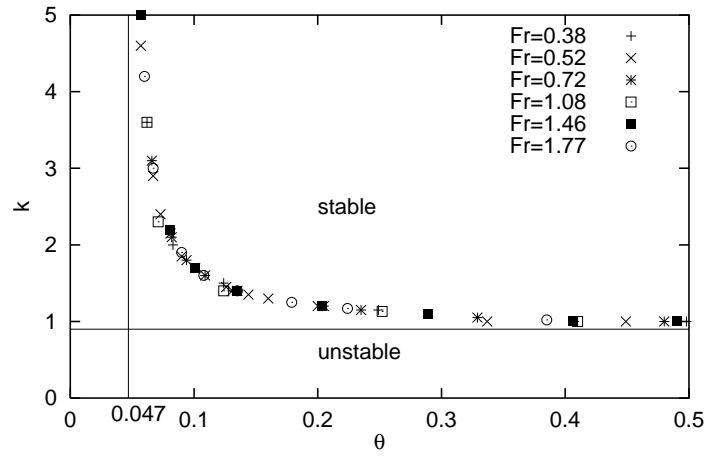


Figure 5.15: The critical value of the exponent of the nodal point relation k is plotted versus Shields parameter ϑ for different values of Froude number.

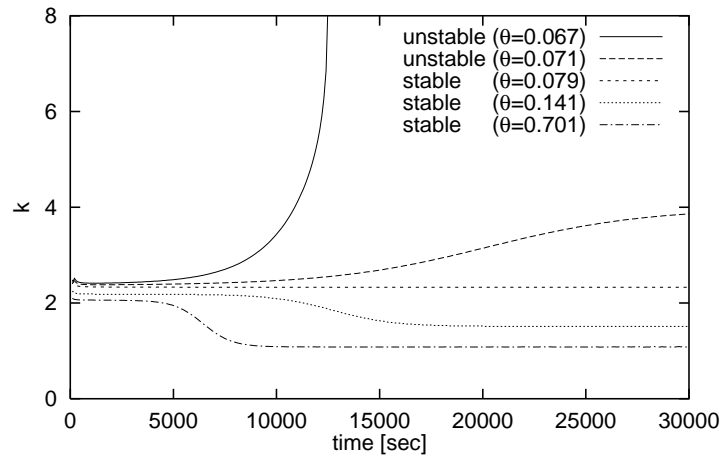


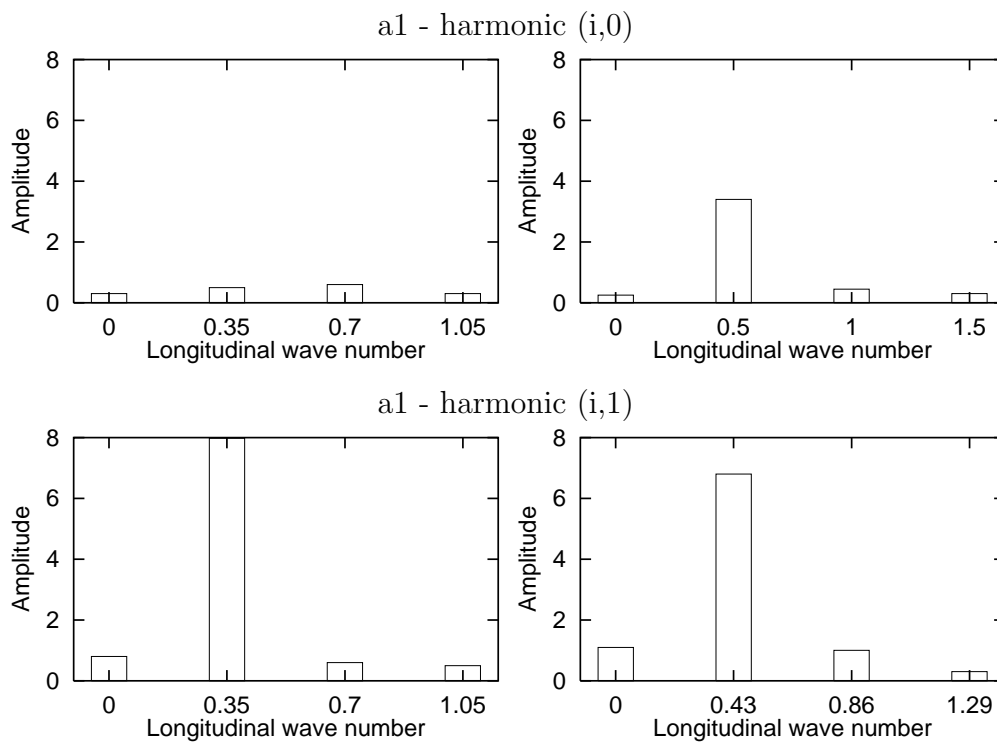
Figure 5.16: The value of the exponent of the nodal point relation k as a function of time for different Shields parameters ϑ .

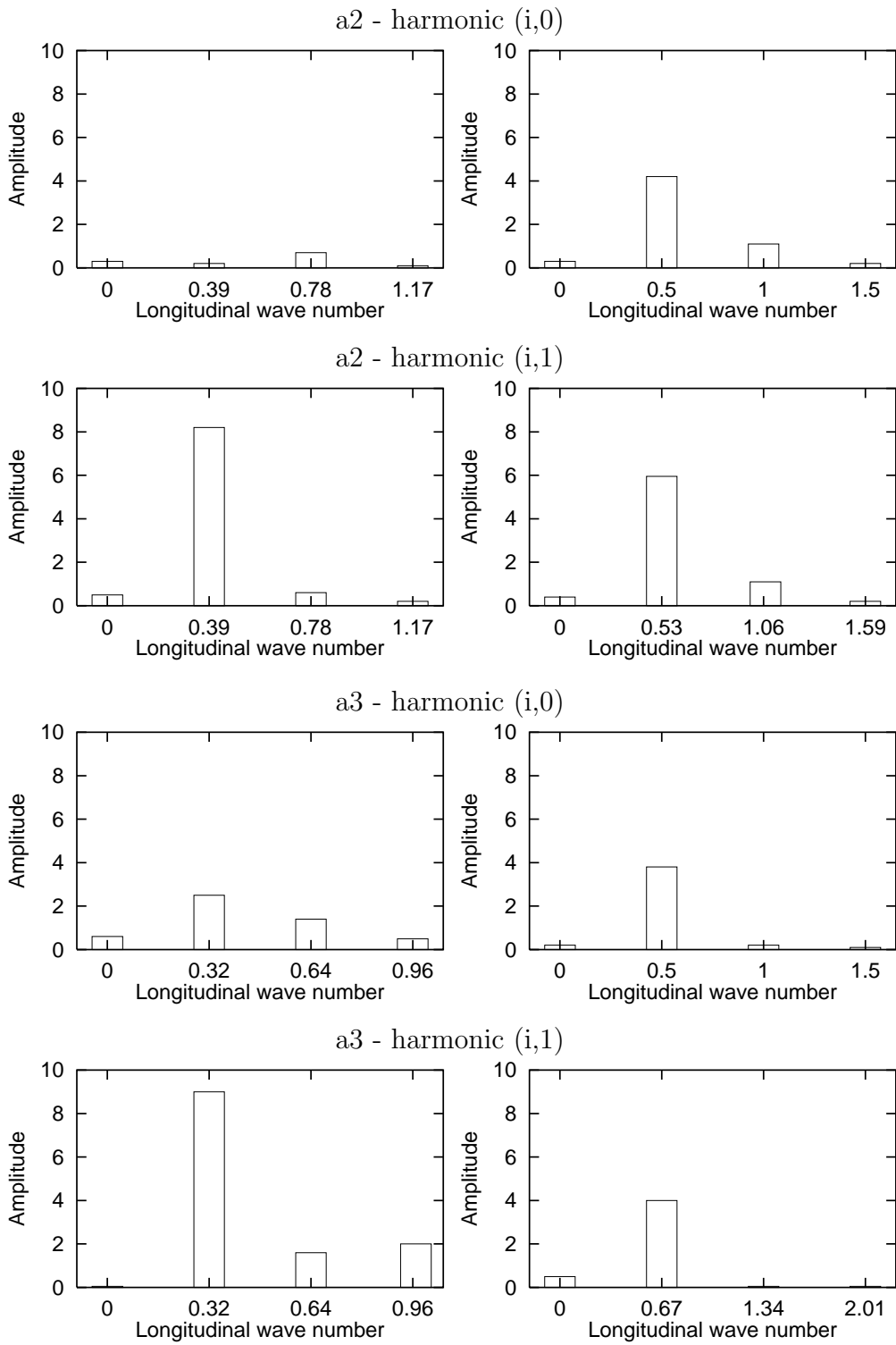
Appendix A

Experimental results

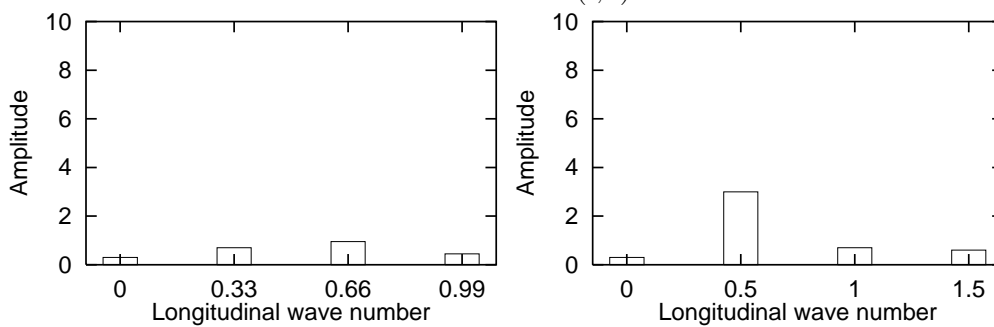
A.1 Series “a”

In the following plots the results of the Fourier analysis of the bed topography are reported for each experiment of series “a”. The harmonics $(i, 0)$ correspond to purely longitudinal deformations of the bed while alternate bars are represented by the harmonics $(i, 1)$.

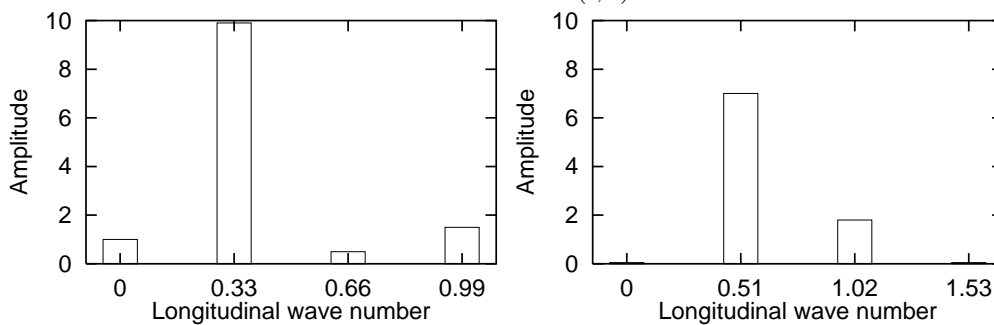




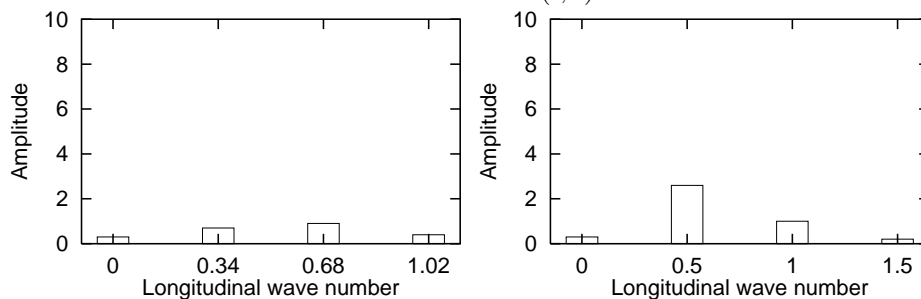
a4 - harmonic (i,0)



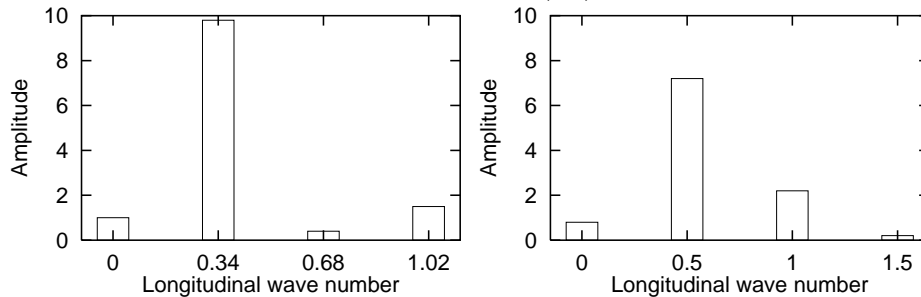
a4 - harmonic (i,1)

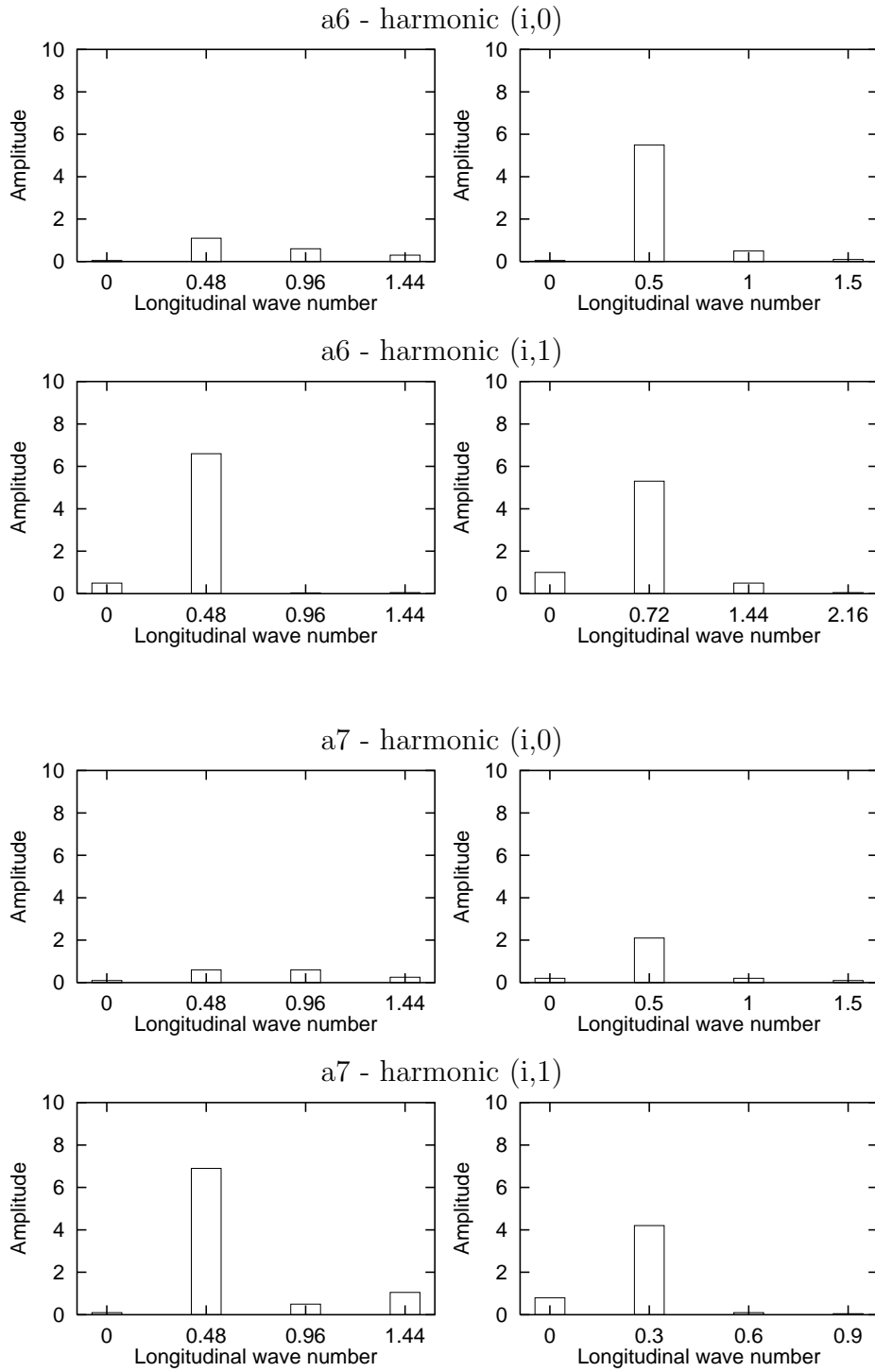


a5 - harmonic (i,0)

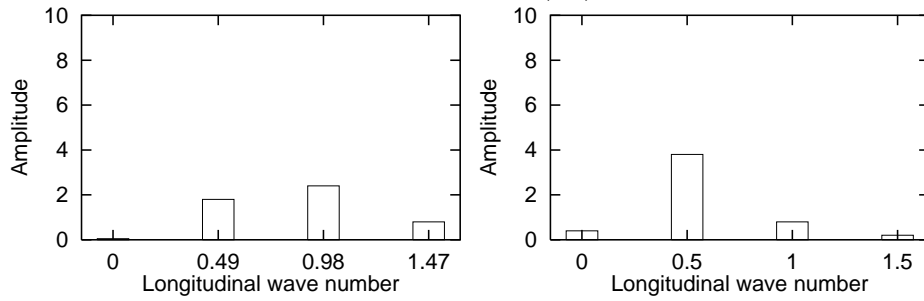


a5 - harmonic (i,1)

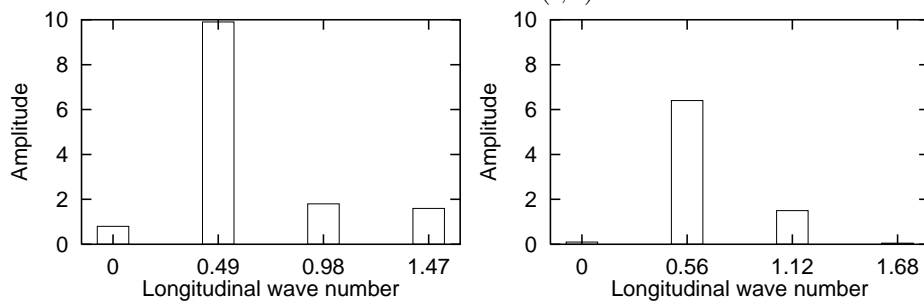




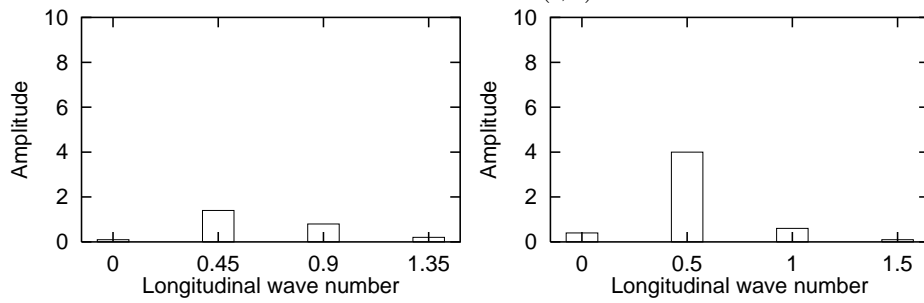
a8 - harmonic (i,0)



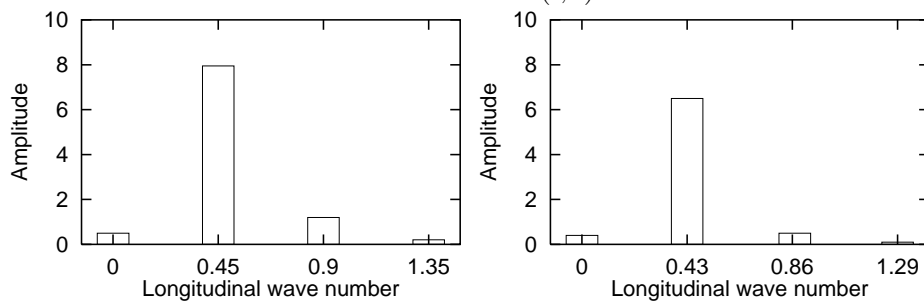
a8 - harmonic (i,1)

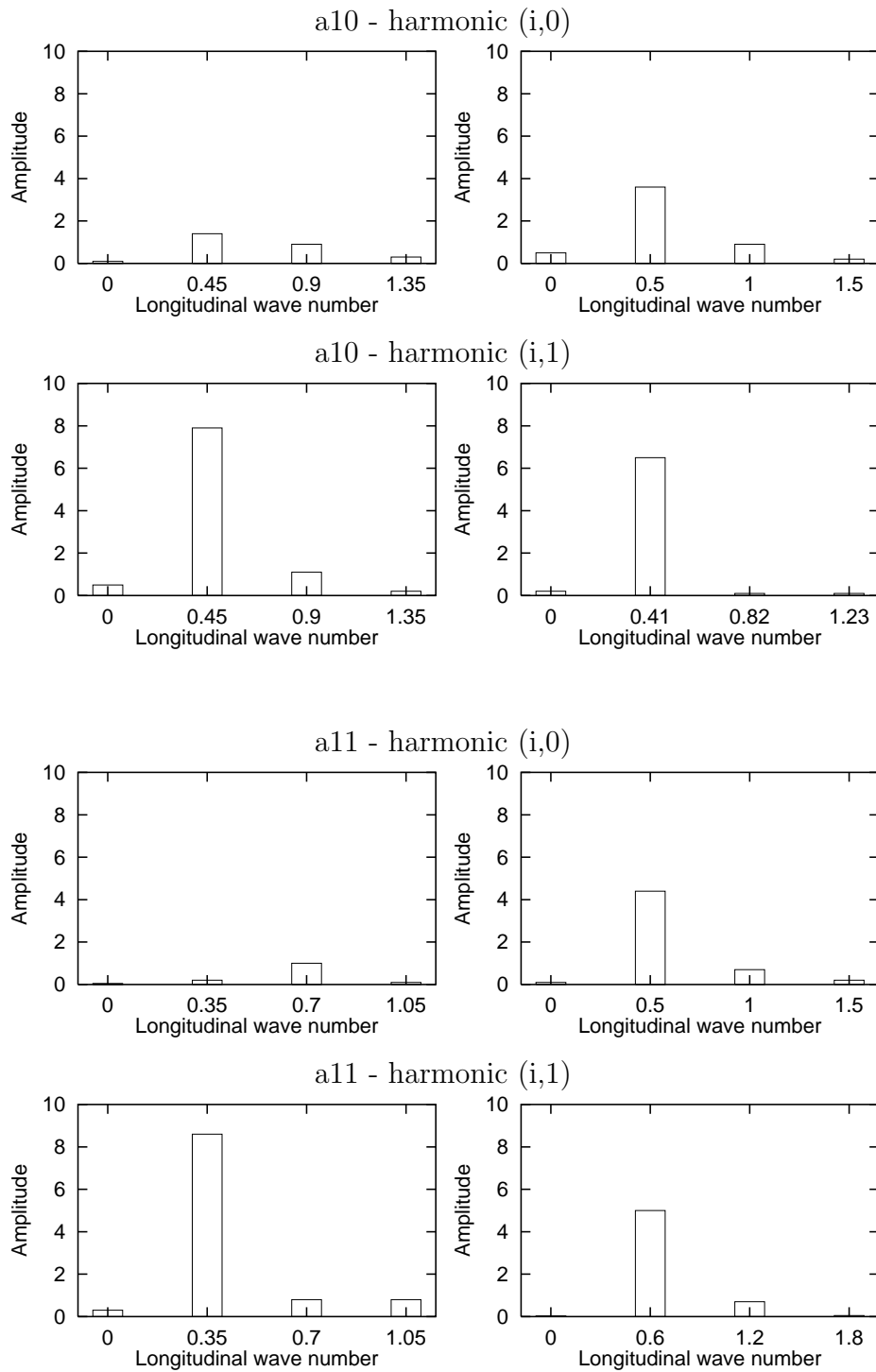


a9 - harmonic (i,0)



a9 - harmonic (i,1)





A.2 Series “b”

In the following tables and plots the results of Fourier analyses of experimental bed configuration are reported along with a comparison with theoretical findings. We denote with A_{exp} and A_{th} the experimental and theoretical amplitudes of each harmonic of bed profile, respectively. Harmonic 0 represents the purely longitudinal component and harmonic 1 the central bar mode. In the plots theoretical results are denoted with continuous lines.

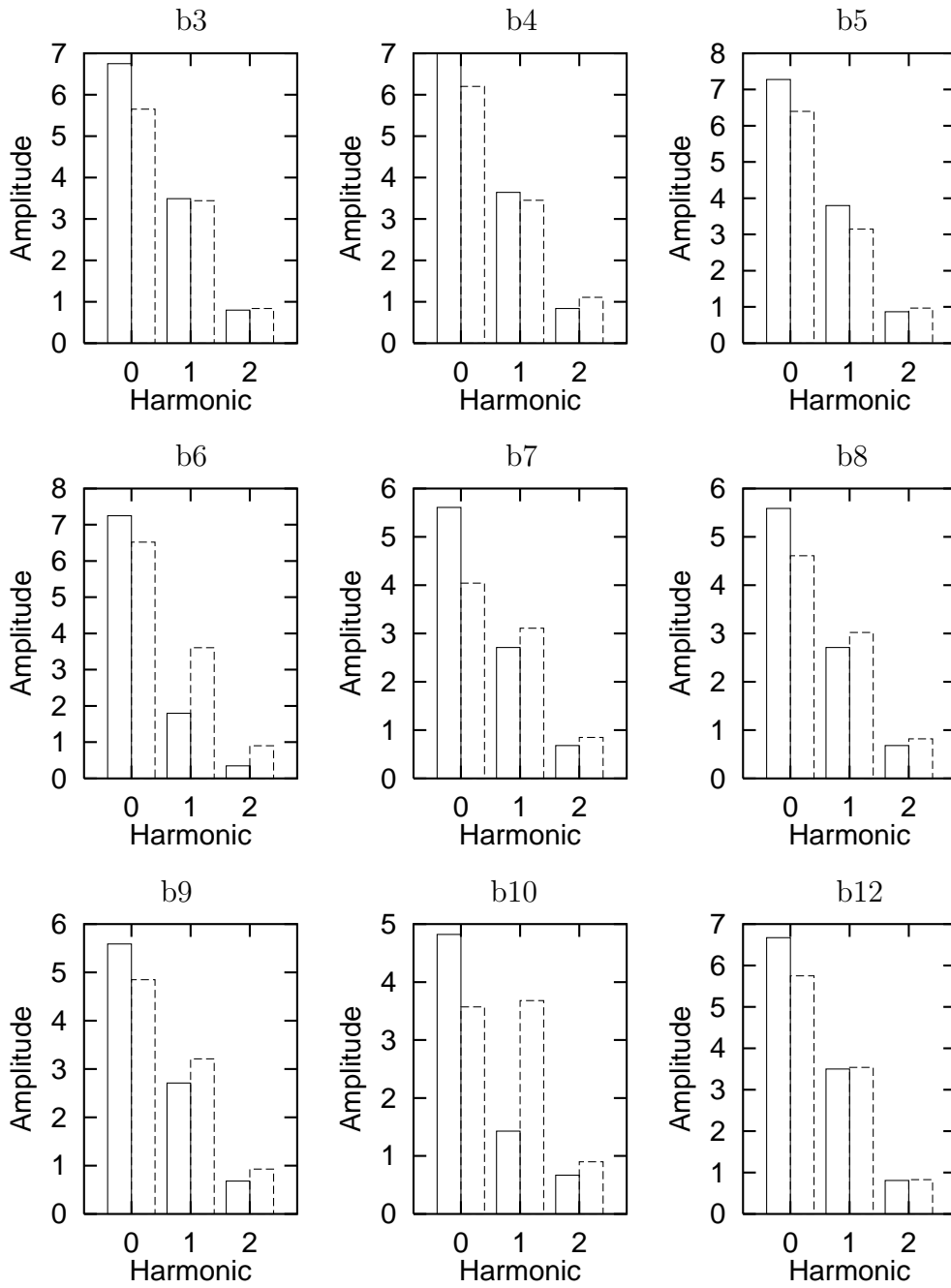
run	harmonic	A_{th} [mm]	A_{exp} [mm]
b3	0	6.75	5.65
	1	3.49	3.44
	2	0.81	0.84
b4	0	7.00	6.20
	1	3.64	3.45
	2	0.84	1.11
b5	0	7.28	6.40
	1	3.80	3.15
	2	0.87	0.97
b6	0	7.25	6.52
	1	1.88	3.61
	2	0.35	0.90
b7	0	5.61	4.04
	1	2.71	3.11
	2	0.68	0.85
b8	0	5.59	4.61
	1	2.71	3.02
	2	0.68	0.82
b9	0	5.59	4.84
	1	2.71	3.21
	2	0.68	0.93
b10	0	4.82	3.57
	1	1.43	3.68
	2	0.67	0.90

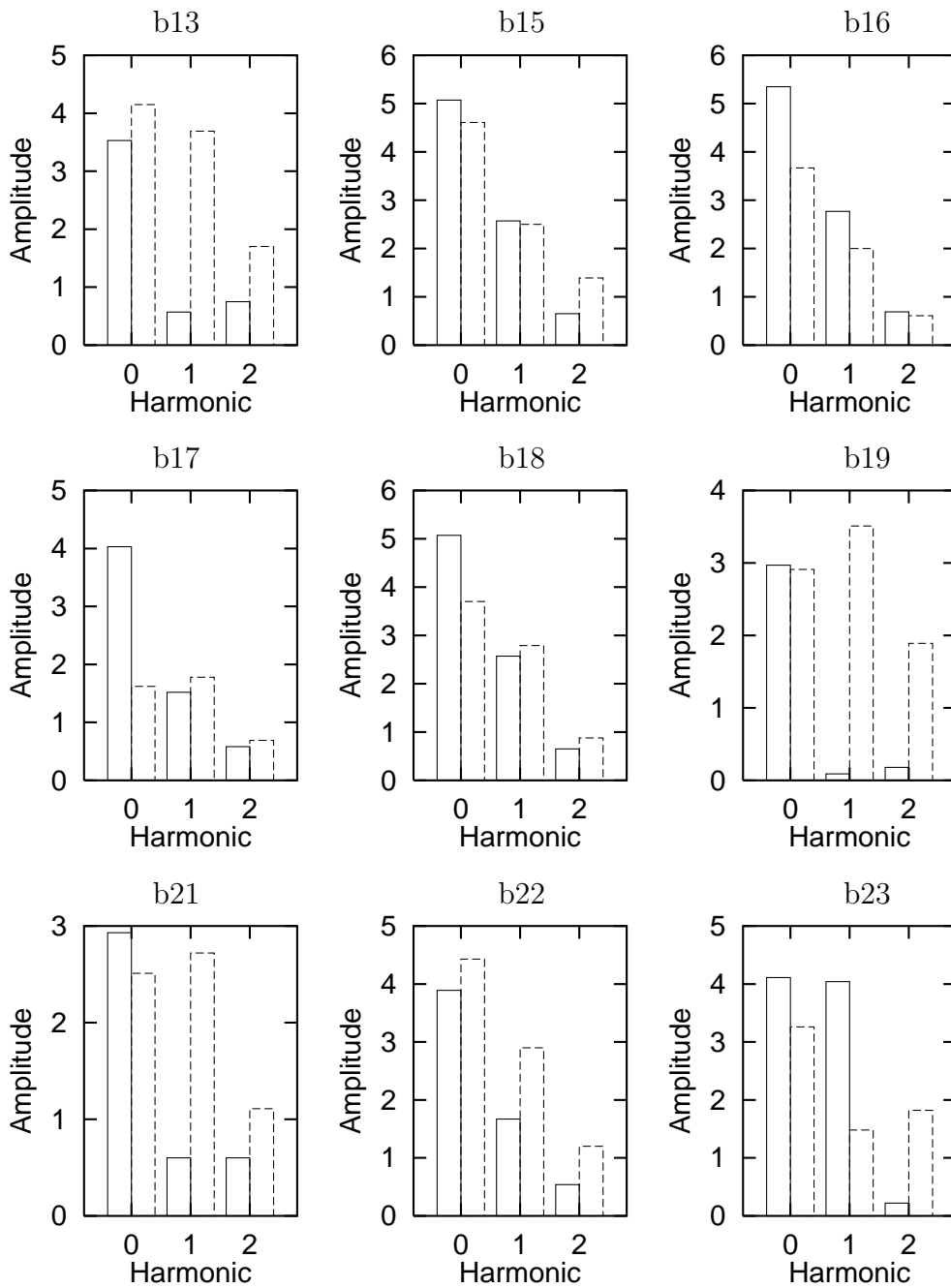
run	harmonic	A_{th} [mm]	A_{exp} [mm]
b12	0	6.67	5.75
	1	3.50	3.54
	2	0.81	0.83
b13	0	3.53	4.15
	1	0.57	3.69
	2	0.75	1.70
b15	0	5.07	4.61
	1	2.57	2.50
	2	0.65	1.39
b16	0	5.35	3.67
	1	2.77	2.00
	2	0.69	0.61
b17	0	4.03	1.62
	1	1.52	1.78
	2	0.58	0.69
b18	0	5.07	3.70
	1	2.57	2.79
	2	0.65	0.88
b19	0	2.97	2.91
	1	0.09	3.51
	2	0.18	1.89
b21	0	2.93	2.51
	1	0.60	2.72
	2	0.60	1.11
b22	0	3.89	4.43
	1	1.67	2.90
	2	0.54	1.20
b23	0	4.11	3.26
	1	4.04	1.48
	2	0.22	1.82
b24	0	5.00	5.32
	1	2.24	1.69
	2	0.25	0.43
b25	0	4.71	4.71
	1	2.12	0.94
	2	0.24	0.81

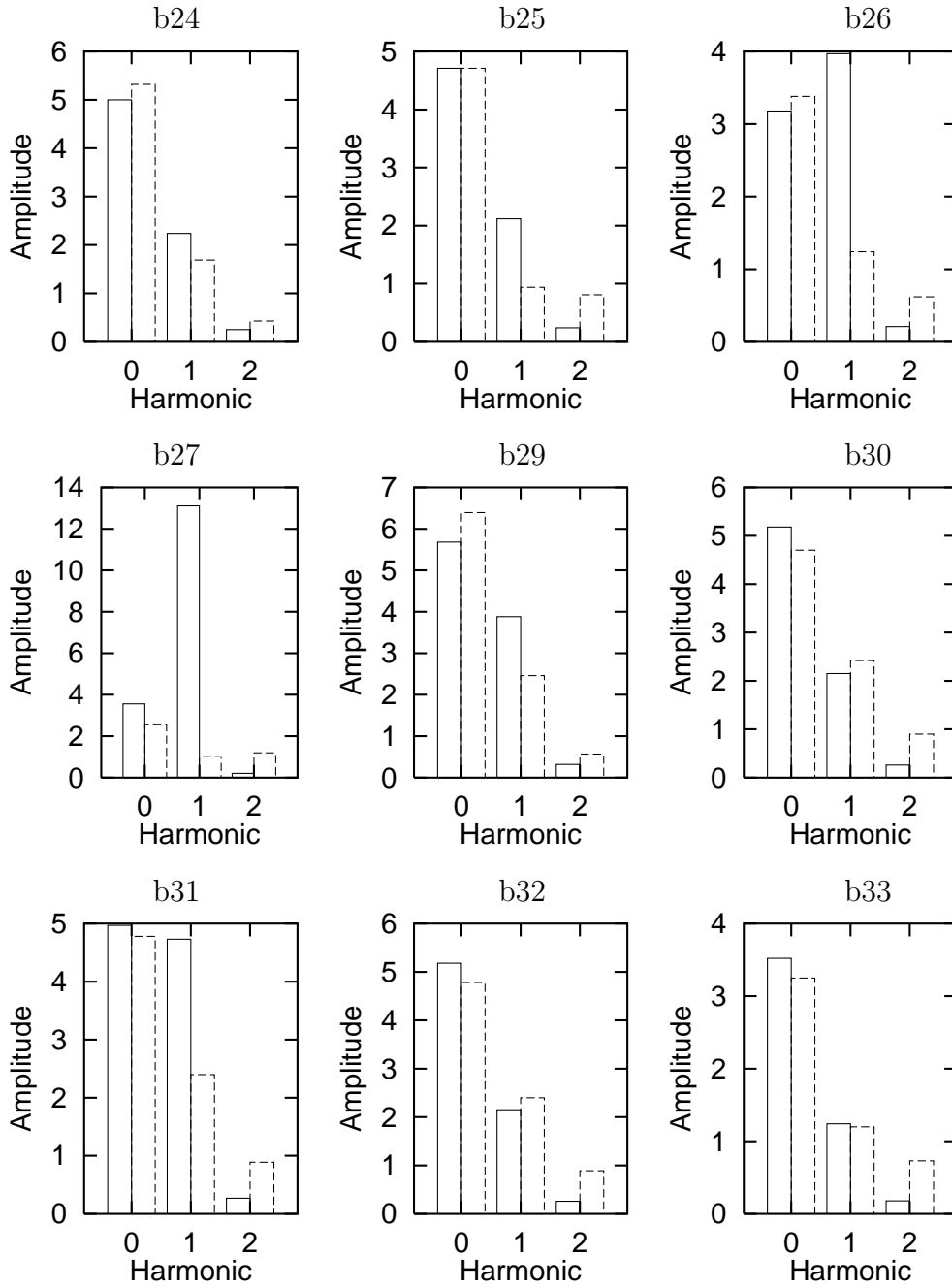
run	harmonic	A_{th} [mm]	A_{exp} [mm]
b26	0	3.18	3.38
	1	3.97	1.24
	2	0.21	0.63
b27	0	3.56	2.55
	1	13.11	1.01
	2	0.21	1.20
b29	0	5.68	6.39
	1	3.88	2.46
	2	0.32	0.57
b30	0	5.18	4.70
	1	2.15	2.42
	2	0.26	0.90
b31	0	4.97	4.78
	1	4.73	2.40
	2	0.27	0.89
b32	0	5.18	4.78
	1	2.15	2.40
	2	0.26	0.89
b33	0	3.52	3.25
	1	1.24	1.20
	2	0.18	0.73
b34	0	3.18	3.25
	1	3.97	1.20
	2	0.21	0.73
b35	0	3.33	2.95
	1	1.93	3.10
	2	0.38	1.18
b36	0	4.67	5.07
	1	3.27	2.04
	2	0.25	0.62
b37	0	4.19	3.23
	1	9.68	2.44
	2	0.24	1.47
b38	0	5.01	4.85
	1	2.54	2.41
	2	0.26	1.03

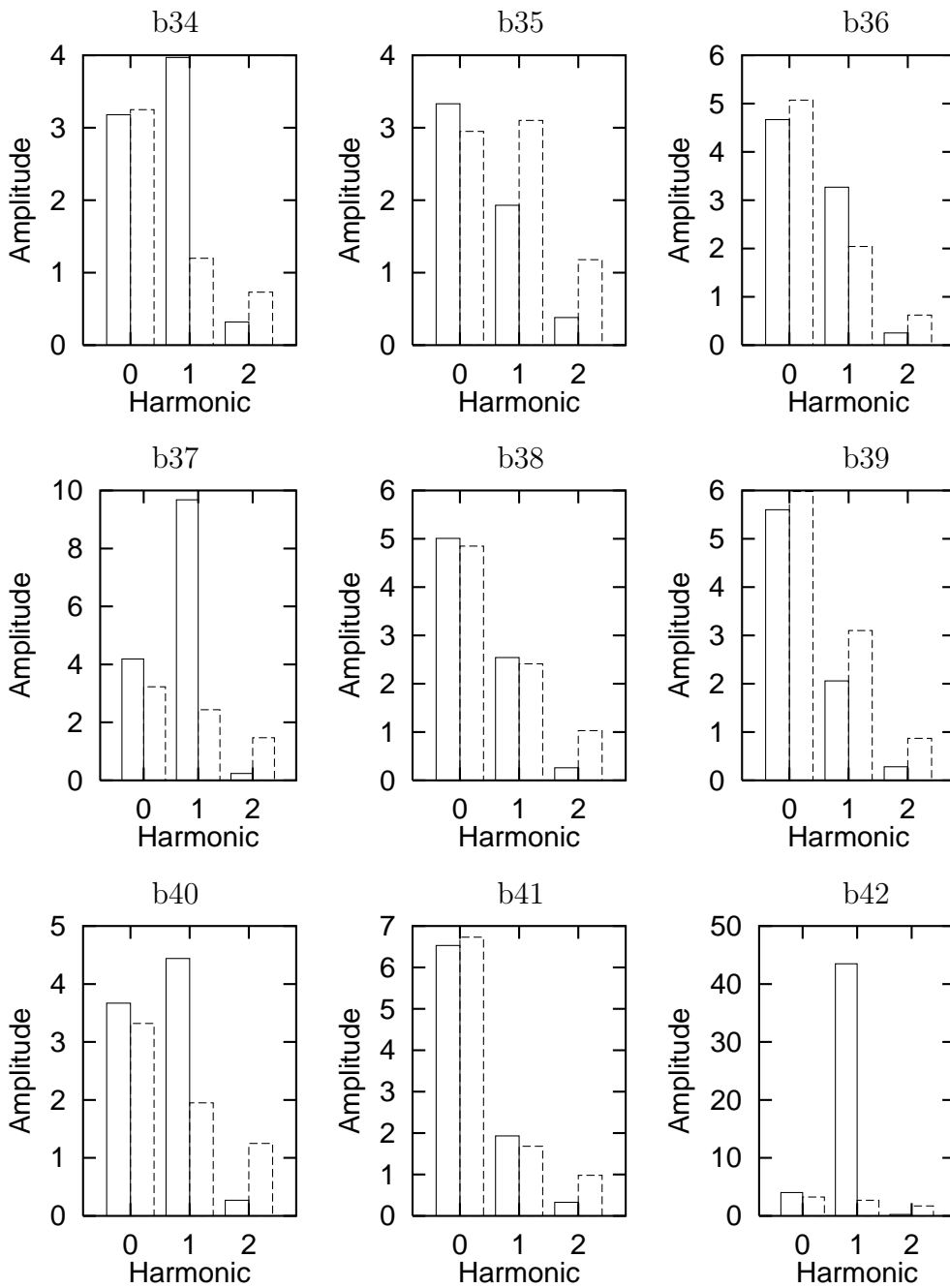
run	harmonic	A_{th} [mm]	A_{exp} [mm]
b39	0	5.60	5.98
	1	2.06	3.10
	2	0.28	0.87
b40	0	3.67	3.32
	1	4.44	1.95
	2	0.27	1.25
b41	0	6.53	6.73
	1	1.93	1.68
	2	0.33	0.98
b42	0	4.03	3.25
	1	43.49	2.68
	2	0.25	1.70
b43	0	5.34	5.35
	1	2.22	3.17
	2	0.27	1.23
b44	0	3.00	2.76
	1	1.13	2.06
	2	0.43	1.34
b45	0	4.44	3.55
	1	4.26	3.39
	2	0.39	1.70
b46	0	5.21	4.58
	1	4.28	2.07
	2	0.27	1.03
b47	0	6.69	6.20
	1	1.97	2.94
	2	0.32	0.70
b48	0	7.49	7.83
	1	1.94	2.84
	2	0.36	0.84
b49	0	4.93	4.18
	1	11.18	3.85
	2	0.28	1.97
b50	0	6.36	6.62
	1	2.04	2.72
	2	0.31	0.91

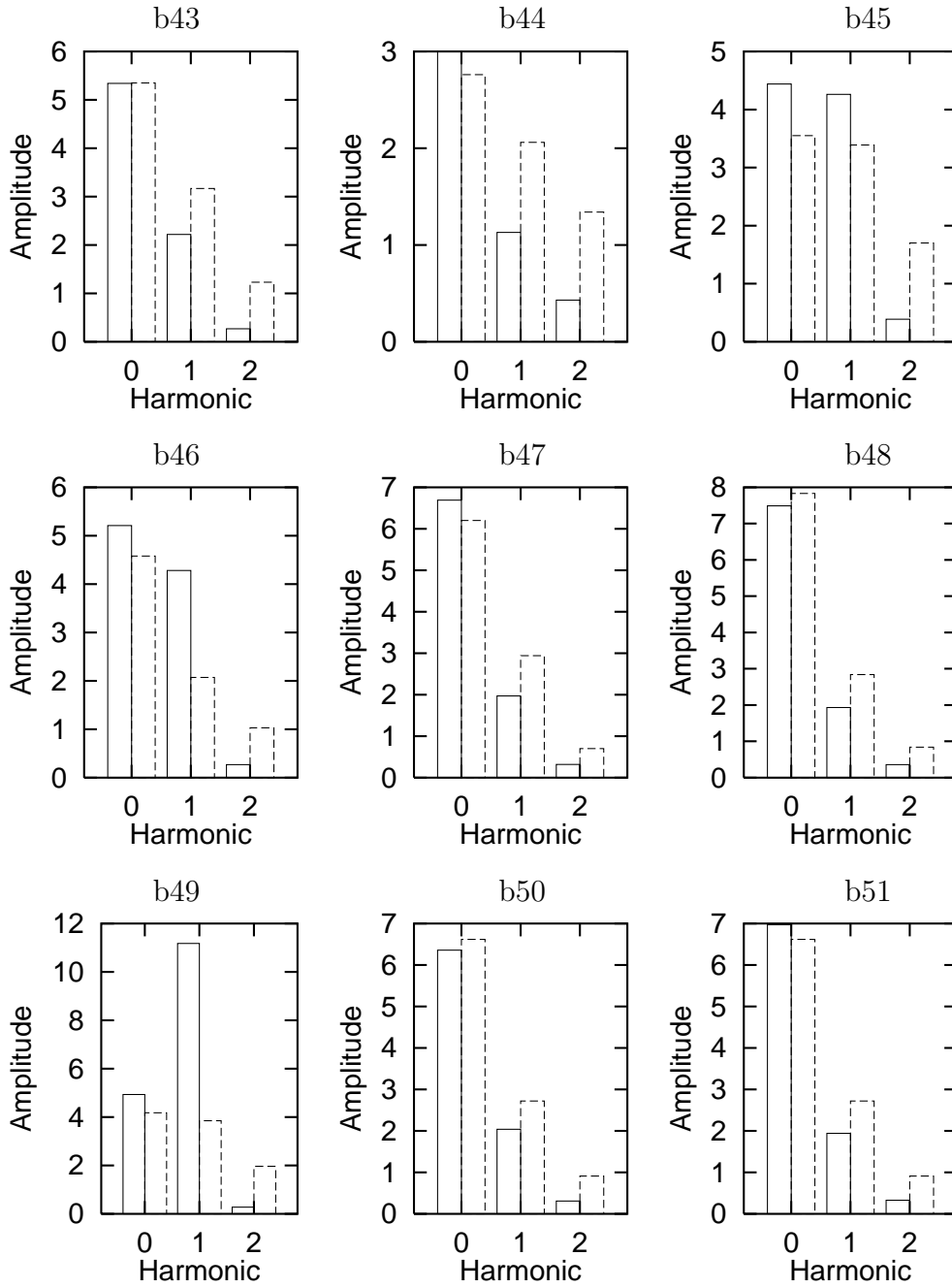
run	harmonic	A_{th} [mm]	A_{exp} [mm]
b51	0	6.97	6.62
	1	1.94	2.72
	2	0.33	0.91
b52	0	6.82	6.72
	1	1.95	1.67
	2	0.33	0.50
b53	0	6.55	6.57
	1	2.00	2.01
	2	0.31	0.42
b54	0	6.62	6.72
	1	1.99	1.67
	2	0.32	0.70
b60	0	13.64	14.48
	1	10.69	3.68
	2	1.22	0.98
b61	0	15.05	17.27
	1	9.01	3.76
	2	0.69	1.58
b62	0	11.88	12.74
	1	22.99	5.11
	2	0.75	1.83
b63	0	10.47	13.19
	1	8.55	2.67
	2	0.55	0.93
b64	0	8.92	11.92
	1	7.28	3.44
	2	0.47	1.04
b65	0	7.43	10.56
	1	4.25	4.76
	2	1.17	2.33
b66	0	11.63	14.82
	1	5.05	3.87
	2	0.57	1.30
b67	0	14.98	18.34
	1	3.87	3.88
	2	0.72	2.00

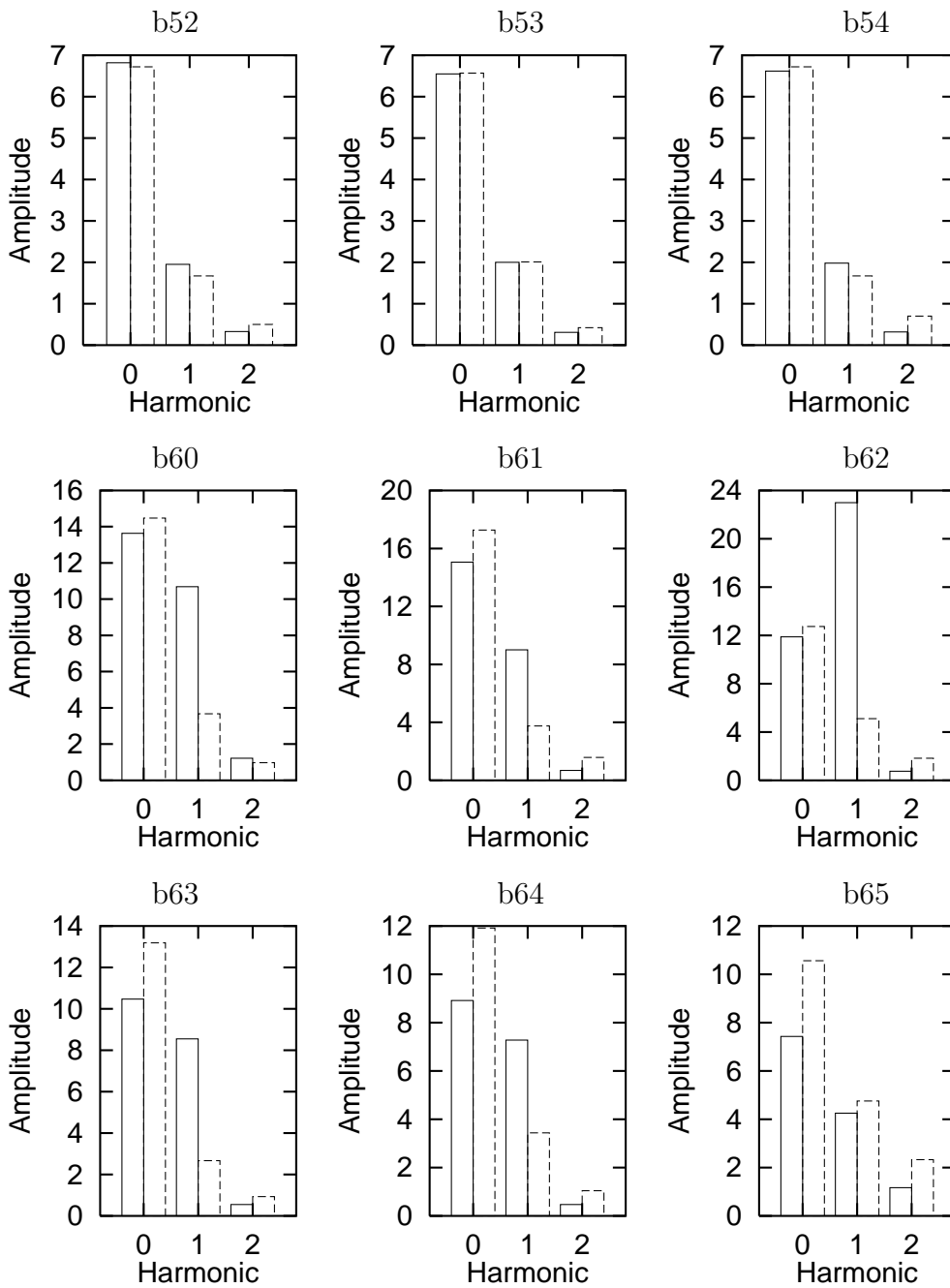


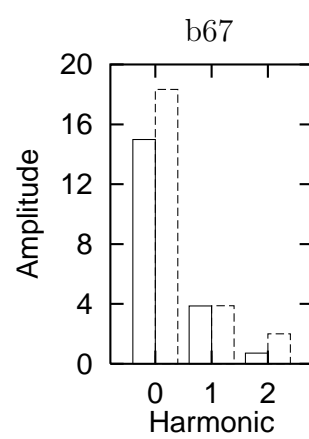
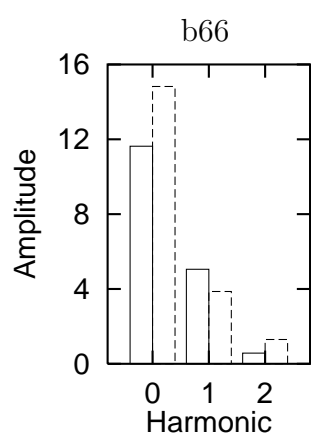












Appendix B

Stability of bifurcations

$$A_j^1 = -B_j^1 = \frac{\theta}{\Delta x}, \quad (\text{B.1})$$

$$C_j^1 = D_j^1 = 0, \quad (\text{B.2})$$

$$E_j^1 = F_j^1 = \frac{b}{2\Delta t}, \quad (\text{B.3})$$

$$L_j^1 = \frac{b}{2\Delta t} (D_j^k + D_{j+1}^k) + \frac{(1-\theta)}{\Delta x} (Q_j^k - Q_{j+1}^k), \quad (\text{B.4})$$

$$A_j^2 = \frac{1}{2\Delta t} + \frac{\theta}{\Delta x} (S_1)_{j+1/2}^{k+\theta}, \quad (\text{B.5})$$

$$B_j^2 = \frac{1}{2\Delta t} - \frac{\theta}{\Delta x} (S_1)_{j+1/2}^{k+\theta}, \quad (\text{B.6})$$

$$C_j^2 = -D_j^2 = \frac{\theta}{\Delta x} (S_2)_{j+1/2}^{k+\theta}, \quad (\text{B.7})$$

$$E_j^2 = -F_j^2 = \frac{\theta}{\Delta x} (S_3)_{j+1/2}^{k+\theta}, \quad (\text{B.8})$$

$$\begin{aligned} L_j^2 = & \frac{1}{2\Delta t} (Q_j^k + Q_{j+1}^k) + \frac{(1-\theta)}{\Delta x} (S_1)_{j+1/2}^{k+\theta} (Q_j^k - Q_{j+1}^k) + \\ & + \frac{(1-\theta)}{\Delta x} (S_2)_{j+1/2}^{k+\theta} (H_j^k - H_{j+1}^k) - (S_4)_{j+1/2}^{k+\theta} + \end{aligned}$$

$$+\frac{(1-\theta)}{\Delta x}(S_3)_{j+1/2}^{k+\theta}(D_j^k - D_{j+1}^k), \quad (\text{B.9})$$

$$A_j^3 = -B_j^3 = \frac{\theta}{\Delta x}(S_5)_{j+1/2}^{k+\theta}, \quad (\text{B.10})$$

$$C_j^3 = D_j^3 = (1-p)\frac{b}{2\Delta t}, \quad (\text{B.11})$$

$$E_j^3 = -F_j^3 = \frac{\theta}{\Delta x}(S_6)_{j+1/2}^{k+\theta}, \quad (\text{B.12})$$

$$\begin{aligned} L_j^3 &= \frac{(1-\theta)}{\Delta x}(S_5)_{j+1/2}^{k+\theta}(Q_j^k - Q_{j+1}^k) + (1-p)\frac{b}{2\Delta t}(H_j^k + H_{j+1}^k) + \\ &+ \frac{(1-\theta)}{\Delta x}(S_6)_{j+1/2}^{k+\theta}(D_j^k - D_{j+1}^k), \end{aligned} \quad (\text{B.13})$$

$$A'_j = A_j^3 \bar{A}_j - A_j^2 \bar{B}_j, \quad (\text{B.14})$$

$$B'_j = C_j^3 \bar{A}_j - C_j^2 \bar{B}_j, \quad (\text{B.15})$$

$$C'_j = E_j^3 \bar{A}_j - E_j^2 \bar{B}_j, \quad (\text{B.16})$$

$$D'_j = \bar{A}_j \bar{D}_j - \bar{B}_j \bar{C}_j, \quad (\text{B.17})$$

$$A''_j = A_j^3 \bar{E}_j - A_j^1 \bar{B}_j, \quad (\text{B.18})$$

$$B''_j = C_j^3 \bar{E}_j, \quad (\text{B.19})$$

$$C''_j = E_j^3 \bar{E}_j - E_j^1 \bar{B}_j, \quad (\text{B.20})$$

$$D''_j = \bar{D}_j \bar{E}_j - \bar{B}_j \bar{F}_j, \quad (\text{B.21})$$

$$\bar{A}_j = B_j^2 G_j + D_j^2 + F_j^2 M_j, \quad (\text{B.22})$$

$$\bar{B}_j = B_j^3 G_j + D_j^3 + F_j^3 M_j, \quad (\text{B.23})$$

$$\bar{C}_j = L_j^2 - B_j^2 L_j - F_j^2 N_j, \quad (\text{B.24})$$

$$\bar{D}_j = L_j^3 - B_j^3 L_j - F_j^3 N_j, \quad (\text{B.25})$$

$$\bar{E}_j = B_j^1 G_j + F_j^1 M_j, \quad (\text{B.26})$$

$$\bar{F}_j = H_j^1 - B_j^1 L_j - F_j^1 N_j. \quad (\text{B.27})$$

Bibliography

- Ashmore, P. E. (1982). Laboratory modeling of gravel bed stream morphology. *Earth Surf. Proc. and Landforms*, vol. 7, 201-225.
- Ashmore, P. E. (1991). How do gravel-bed rivers braid? *Can. J. Sci.*, 28, 326-341.
- Ashmore, P. E. & Parker, G. (1983). Confluence scour in coarse braided streams *Water Resources Research*, 19, 392-402.
- Bittner, L. (1994). River bed response to channel width variation, *Master Thesis, Univ. of Illinois*.
- Blondeaux, P. & Seminara, G. (1985). A unified bar-bend theory of river meanders. *J. Fluid Mech.*, 157, 449-470, 1985.
- Colombini, M., Seminara, G. & Tubino, M. (1987). Finite-amplitude alternate bars, *J. Fluid Mech.*, 181, 213-232.
- Colombini, M., Tubino, M. & Whiting, P. J. (1992). Topographic expression of bars in meandering channels. *In Dynamics of gravel-bed rivers*, (ed. by P. Billi, R.D. Hey, C.R. Thorne and P. Tacconi). John Wiley & Sons Ltd. 457-474.
- Dean, R. B. (1974). *Aero Rept. 74-11, Imperial College, London*.
- Enstein, H. A. (1950). The bedload function for sediment transport in open channel flow, *US Dept. Agric. Tech. Bull.*, 1026.
- Engelund, F. (1974). Flow and bed topography in channel bends. *J. Hydraul. Div., ASCE*, 100 (HY11), 1631-1648.
- Fredsøe, J. (1978). Meandering and braiding of rivers. *J. Fluid Mech.*, 84, 609-624.
- Fujita, Y. & Muramoto, Y. (1988). Multiple bar and stream braiding. *International conference on river regime. Edited by W. R. White. Hydraulic Research Limited, Wallingford, U. K.*, pp. 289-300.
- Ikeda, S. (1982). Lateral bedload transport on side slopes, *J. Hydraul. Engng.*

- ASCE*, 108, 1369-1373.
- Ikeda, S., Parker G. & Sawai, K. (1981). Bend theory of river meanders. Part 1 - Linear development, *J. Fluid Mech.*, 112, 363-377.
- Johannesson, H. & Parker, G. (1989a). Linear theory of river meanders, *River Meandering, edited by S. Ikeda and G. Parker, Water Res. Monogr.*, 12 AGU, Washington, D. C., 181-213.
- Johannesson, H. & Parker, G. (1989b). Secondary flow in a mildly sinuous channel, *J. Hydraul. Engng., ASCE*, 115 (3), 289-308.
- Johannesson, H. & Parker, G. (1989c). Velocity redistribution in meandering rivers, *J. Hydraul. Engng., ASCE*, 115 (8), 1019-1039.
- Kinoshita, R. & Miwa, H. (1974). River channel formation which prevents downstream translation of transverse bars, *Shinsabo*, 94, 12-17. (In Japanese).
- Leopold, L. B. & Wolman, G. (1957). River channel patterns: Braiding, meandering and straight, *Phys. and Hydr. Studies of Rivers*, 14, 283-300.
- Meyer-Peter, E. & Müller, R. (1948). Formulas fo bedload transport, *III Conf. of Internat. Ass. of Hydraul. Res., Stockholm, Sweden*.
- Mosley, M. P. (1976). An experimental study of channel confluences. *Journal of Geology*, 84(5), 535-562.
- Murray, A. B. & Paola, C. (1994). A cellular model of braided rivers, *Nature*, 371, 54-57, 1994.
- Olesen, K. W. (1987). Bed topography in shallow river bends, *Communications on Hydraulic and Geotechnical engineering*, Rep. 87-1.
- Parker, G. (1978). Self-formed straight rivers with equilibrium banks and mobile bed. Part 2. The gravel river, *J. Fluid Mech.*, 89, 127-146.
- Preissmann, A. (1961). *1st Congres de l'Association Francaise de Calcul*, Grenoble.
- Preissman, A. & Cunge, J. A. (1961). *Proc. 9th IAHR Congress*, Dubrovnik.
- Repetto, R. & Tubino, M. (1999)a. Topographic expressions of bars in channels with variable width. *EGS XXIV General Assembly, The Hague*.
- Repetto, R. & Tubino, M. (1999)b. Transition from migrating alternate bars to steady central bars in channels with variable width. *I.A.H.R. Meeting. River, coastal and estuarine morphodynamics, Genova 6-10 September 1999*, vol. I, pp. 605-614.

- Richtmyer R. D., Morton K. W. (1967). Difference method for initial value problems, *Wiley*, New York.
- Shaffranek, R. W., Golberg, D. E. & Baltzer, R. A. (1981). *USGS Tech. of Water Resources Inv.*, book 7 (chapter 3).
- Seminara, G. & Tubino, M. (1992). Weakly non linear theory of regular meanders. *J. Fluid Mech.*, 224, 257-288.
- Talmon, A., van Mierlo, M.C.L.M. & Struiksma, N. (1995). Laboratory measurements of direction of sediment transport on transverse alluvial-bed slopes, *J. Hydr. Res.* 33 (4), 519-534.
- Tubino, M. & Seminara, G. (1990). Free-forced interactions in developing meanders and suppression of free bars. *J. Fluid Mech.*, 214, 131-159.
- Wang, Z. B., Fokkink, R. J., De Vries, M. & Langerak A. (1995). Stability of river bifurcations in 1D morphodynamics models. *J. Hydraul. Res.*, vol. 33 n. 6, pp. 739-750.
- Whiting, P. J. & Dietrich, W. E. (1993). Experimental studies of bed topography and flow patterns in large-amplitude meanders. 1. Observations. *Water Resour. Res.*, 29(11), 3605-3622.

Acknowledgements

This work has been developed within the framework of the National Project supported by the Italian Ministry of University and Scientific Research Cofin '97 "*Fluvial and Coastal Morphodynamics*".

Ringraziamenti

Sono profondamente grato al prof. Marco Tubino che mi ha attentamente seguito durante il corso di tutto il dottorato: lavorare insieme è stato sempre piacevole e stimolante.

Ringrazio il *Maestro* prof. Giovanni Seminara per la passione e l'entusiasmo che ha saputo infondermi nei confronti della ricerca.

Sono riconoscente al prof. Gianpaolo Di Silvio per aver attentamente letto questo elaborato, fornendomi utili commenti e spunti di riflessione.

Dalla collaborazione con il prof. Chris Paola sono scaturite molte preziose idee che hanno contribuito allo sviluppo del lavoro di tesi.

Sono inoltre grato ai prof. Chris Paola e Peter Ashmore per l'organizzazione della campagna di misure di campo sul fiume Sunwapta, in Canada, che mi ha permesso di vivere un'esperienza estremamente formativa.

Un sentito ringraziamento a Veronica Galletta, Luca Solari e Guido Zolezzi con i quali ho condiviso questi anni di dottorato e che hanno contribuito a rendere il lavoro piacevole e divertente.

Ringrazio Giovanni Besio, Michele Bolla Pittaluga, Daniele Cristoforetti, Erik Gadotti e Claudio Volcan con i quali ho collaborato nello sviluppo della ricerca.

Sono infine grato al Dipartimento di Ingegneria delle Strutture, delle Acque e del Terreno dell'Università dell'Aquila che mi ha permesso di svolgere l'ultimo anno di dottorato presso le proprie strutture.